„Multi-scale, correlative structural and material characterization
of the tiled skeletons of sharks and rays"

D I S S E R T A T I O N
zur Erlangung des akademischen Grades
Doctor rerum naturalium
(Dr. rer. nat.)

Eingereicht an der
Lebenswissenschaftlichen Fakultät der Humboldt-Universität zu Berlin
von
Ronald Seidel
31.10.1979 – Berlin

Präsidentin
der Humboldt-Universität zu Berlin
Prof. Dr. –Ing. Dr. Sabine Kunst

Dekan der Lebenswissenschaftlichen Fakultät
der Humboldt-Universität zu Berlin
Prof. Dr. Bernhard Grimm

Gutachter:

1. . . . .

2. . . . .

3. . . . .

Tag der mündlichen Prüfung: . . . .

Die Endlosigkeit des wissenschaftlichen Ringens sorgt unablässig dafür, daß dem
forschenden Menschengeist seine beiden edelsten Antriebe erhalten bleiben und immer wieder
von neuem angefacht werden: die Begeisterung und die Ehrfurcht.

– Max Planck –

ABSTRACT

Elasmobranch fish (sharks, rays, skates and sawfish) are unique among vertebrates in lacking a bony endoskeleton, having instead a skeleton comprised largely of unmineralized cartilage. Each skeletal element mineralizes only on the outside, forming a thin outer layer, in contrast to the fully mineralized skeletons of the vast majority (~98%) of vertebrate species. Moreover, the mineralized crust is not continuous, as with the surface of bones, but rather broken into an array of polygonal tiles, called tesserae. This 'tessellation' has defined the elasmobranch group for more than 400 million years, yet the limited data on development and ultrastructure of elasmobranch skeletons have restricted our abilities to understand tessellated cartilage growth and mechanics, and develop hypotheses for its implications for vertebrate skeletal evolution. Research efforts have been particularly hampered by the small size of tesserae (~500 x 300 µm, width x height), the composite nature of the skeleton (comprising unmineralized cartilage, tesserae and their flexible joints), and their complicated 3d arrangements. In this dissertation, I address these issues in a multi-scale structural analysis of tesserae and associated unmineralized tissues providing a holistic view on elasmobranch tessellated cartilage.

The first study examines the mineral phase of tesserae, using high-resolution, two-dimensional and three-dimensional materials science techniques and biological methods, including micro-computed tomography (µCT), transmission and scanning electron microscopy (TEM and SEM), immunohistochemistry (IHC), histology and light microscopy (LM) to characterize the ontogeny of tesserae and their ultrastructure in round stingray *Urobatis halleri*. We outline the development of unique intratesseral features, define growth phases for tesserae and illustrate in backscatter SEM images that tesserae are strongly heterogeneous with distinct mineral density variations representing records of growth processes, but without evidence of repair or remodeling. We show that tesserae are anchored to surrounding tissues by fiber bundles, which extend uninterrupted between unmineralized and mineralized tissues. High-resolution µCT data indicate that the joints between tesserae are structurally complex architectures, involving complicated arrangements of mineralized and fibrous materials, but no structural interdigitations. We observe commonalities in tesseral structural features, such as local mineral density and cell distribution, among species of all major elasmobranch groups despite large variation in tesseral shape and size, suggesting universal principles of tesseral growth and form across elasmobranchs.

The second study examines the soft tissue associated with and underlying the tesseral layer, showing that the varying mineral density observed in tesserae, is mirrored in density variation of the underlying collagen matrix. Our data allow us to answer a long-standing question of whether tesserae are more like bone or calcified cartilage. We use IHC, TEM and histology to characterize the collagenous composition of tessellated cartilage and surrounding tissues in *U. halleri*, showing that tesserae are

bipartite composites, comprised of an upper "cap zone" that merges into a lower "body zone", patterned on type-I or type-II collagen (Coll I & II), respectively. Our TEM imaging shows thick Coll I-based Sharpey's fibers, typically observed in vertebrate dentition and bone tissue, coming from the perichondrium and inserting into the cap zone of tesserae. The fibrous material linking adjacent tesserae is also spatially diverse, comprised of an upper (perichondral) portion containing both Coll I and Coll II fibers, whereas the lower (chondral) portion contains finer, unidentified fibers that stained neither for Coll I, II, X nor Elastin. Coll X expression, a common marker for mineralization in mammals, was only observed on the perichondral side of tesserae, in a thin, supratesseral layer of unmineralized cartilage matrix (Coll II). These findings illustrate that tesserae are a structurally complex hybrid tissue, an amalgam of chondroid bone and mineralized cartilage, and indicate that vertebrate cartilage mineralization can also occur in the absence of Coll X and without cell hypertrophy or cell death.

The third study draws on the first two works examining a previously undescribed type of calcified cartilage associated with tesserae appearing to be a response to mineralization control failure. Unlike the bony skeletons of other vertebrates, elasmobranch skeletons have limited healing capability and their mechanisms for avoiding damage or responding to it when it does occur are largely unknown. We describe an aberrant, tesserae-associated type of elasmobranch mineralized cartilage, which we term endophytic masses (EPMs). When compared to tesserae and other elasmobranch calcified tissues EPMs exhibit strikingly different morphologies, demonstrating them to be distinct tissues. We use histology, µCT, backscatter SEM, TEM, selected area electron diffraction (SAED) and energy dispersive X-ray spectroscopy (EDX) and Raman spectroscopy to characterize the morphology, ultrastructure and chemical composition of EPMs in different shark and ray species. EPMs appear to develop between and in intimate association with tesserae, grow into the unmineralized cartilaginous core, but lack the lines of periodic growth and varying mineral density characteristic of tesserae. Both tesserae and EPMs appear to develop in a Coll II-based matrix, but in contrast to tesserae, all chondrocytes embedded or in contact with EPMs are dead and mineralized. EPMs are mineral-dominated (high mineral and low organic content), comprised of birefringent bundles of large calcium phosphate crystals (likely brushite) aligned end to end in long strings. We discuss several possible etiologies for EPM development, including tissue reinforcement, repair, and disruptions of mineralization processes, within the context of elasmobranch skeletal biology, as well as the damage responses of other vertebrate mineralized tissues.

The studies of this dissertation build on each other's findings to provide complementary perspectives on the growth, structuring and homeostasis of elasmobranch tessellated cartilage. The results underline the potential of this skeletal tissue, as a natural alternative to bone and a valuable model, not only for skeletal evolution research, but also functional anatomy, biomedicine and composite mechanics.

ZUSAMMENFASSUNG

Das Skelett der Rochen und Haie (Elasmobranchii, oder Plattenkiemer) ist in vielerlei (biologischer, medizinischer und bautechnischer) Hinsicht interessant, da es einzigartig in seiner Anatomie und Zusammensetzung innerhalb der Wirbeltierskelette ist. Im Gegensatz zu den verknöcherten Skeletten der meisten Wirbeltiere –etwa 98% der Wirbeltierarten besitzen ein Endoskelett aus Knochen– besteht das Skelett von Rochen und Haien zum größten Teil aus Knorpel. Deshalb bezeichnet man Rochen und Haie auch als Knorpelfische. Das Knorpelskelett ist oberflächlich von einer dünnen Schicht aus kleinen, mineralisierten Kacheln, den sogenannten „Tesserae" überzogen, die miteinander durch faseriges Gewebe verbunden sind. Dieses Mosaik aus mineralisierten Tesserae ist ein Alleinstellungsmerkmal des Knorpelfischskelettes, welches anhand von Fossilienfunden auf über 400 Millionen Jahre zurückdatiert werden kann. Über die Entwicklung und Ultrastruktur (oder Mikromorphologie) der Knorpelfischskelette ist jedoch wenig bekannt, wodurch Hypothesen zum Wachstum der Tesserae und auch der Evolution der Knorpelfisch- und Wirbeltierskelette im Allgemeinen nur sehr eingeschränkt belegbar sind.

Die Entwicklung und Ultrastruktur der Tesserae des kalifornischen Rundstechrochens *Urobatis halleri* wurde mit Hilfe von hochauflösenden, 2- und 3-dimensionalen Techniken der Materialwissenschaften und der Biologie, einschließlich Mikro-Computertomographie (µCT), Transmissions- und Rasterelektronenmikroskopie (TEM und SEM), Immunhistochemie (IHC), Histologie und Lichtmikroskopie (LM) charakterisiert (siehe die erste Studie dieser Arbeit). Anhand elektronenmikroskopischer Bilder wird der heterogene Aufbau sowie die Entstehung von außergewöhnlichen Merkmalen der Tesserae beschrieben und Stadien ihrer Entwicklung definiert. Die Untersuchungen zeigen, dass Unterschiede in ihrer Mineraliendichte von Wachstumsprozessen zeugen, die keinen Hinweis auf Reparaturmechanismen oder Heilungsprozesse geben. Hochauflösende mikro-computertomographische Daten offenbaren die Komplexität der „Gelenke" zwischen den Tesserae. Diese bestehen aus komplizierten Verflechtungen aus mineralisiertem und nicht-mineralisiertem, faserigen Material. Größere Überlappungen und Verzahnungen anliegender, benachbarter Tesserae existieren nicht. Trotz der großen Variabilität in Form und Größe der Tesserae verschiedener Rochen- und Haiarten können wir Gemeinsamkeiten zwischen ihnen beobachten, zum Beispiel in der Mineraliendichte- und Zellverteilung, die auf universelle Prinzipien des Tesseraewachstums innerhalb der gesamten Knorpelfische schließen lassen.

Ultrastrukturelle Beobachtungen anhand von Querschnitten der Tesserae deuten darauf hin, dass sie durch Faserbündel mit dem umliegenden Gewebe fest verankert sind. Die Fasern enden nicht an der Oberfläche der Tesserae sondern dringen aus umliegendem, nicht-mineralisiertem Gewebe tief in das mineralisierte Gewebe der Tesserae ein. In der zweiten Studie dieser Dissertation wird gezeigt,

dass sich die Muster der lokal unterschiedlichen Mineraliendichten in dem darunter liegenden, organischen Gewebe wiederspiegeln. Mit Hilfe von IHC, TEM und Histologie wurde die kollagene Zusammensetzung des mineralisierten Knorpels und der angrenzenden Gewebe im Stachelrochen *U. halleri* bestimmt. Dabei wird deutlich, dass adulte Tesserae einen zweiteiligen Aufbau besitzen. Sie bestehen aus einem äußeren Bereich basierend auf Kollagen Typ-1 („cap zone"), der mit einem darunterliegenden, dem Skelettkern zugewandten, Körper basierend auf Kollagen Typ-2 („body zone") verschmolzen ist. Benachbarte Tesserae sind durch faseriges Gewebe in den intertesseralen Gelenken miteinander verbunden, und auch hier ist eine Zweiteilung der kollagenen Zusammensetzung der Gelenke erkennbar, bei der der äußere Bereich, nahe dem Perichondrium, Faserbündel vom Kollagen Typ-1 und -2 aufweist. Im Gegensatz dazu zeigt der untere, dem Knorpelinneren zugewandte, Teil transparente und sehr feine Fasern, die weder als Kollagen Typ-1, 2 oder 10, noch als Elastin (ein Strukturprotein mit hoher Dehnungsfähigkeit) identifiziert werden konnten. Anhand von elektronenmikroskopischen Bildern wird der Verlauf von dicken Kollagen Typ-1 Faserbündeln, ähnlich den Sharpey's Fasern (die ursprünglich im Zahn- und Knochengewebe anderer Wirbeltiere beschrieben worden sind) vom Perichondrium in die „cap zone" gezeigt. Eine elektronendichte Hülle, welche die Faserbündel in der mineralisierten Matrix bedeckt, scheint die Ursache für das fehlende Anfärben der Faserbündel im Tesserae mit histologischen Methoden zu sein. Eine starke extrazelluläre Kollagen Typ-10 Expression ist nur in einer dünnen, nicht-mineralisierten Knorpelschicht (Kollagen Typ-2) zwischen Tesserae und Perichondrium nachzuweisen, und deutet damit auf Parallelen zur Kalzifikation von Knorpel bei anderen Wirbeltieren hin, fehlt jedoch an den anderen Mineralisationsfronten (laterale und chondrale, dem Knorpelinneren zugewandte Ränder) der Tesserae. Die Ergebnisse sprechen dafür, dass Tesserae ein intermediäres Gewebe sind und aus kalzifiziertem Knorpel und chondroidalem Knochen („chondroid bone", Knochenmatrix mit Chondrocyten) bestehen. Des Weiteren zeigen sie, dass der Prozess der Mineralisierung von Knorpel innerhalb der Wirbeltiere nicht zwangsläufig an das Vorhandensein von Kollagen Typ-10, Zellhypertrophie (signifikante Zellvolumenvergrößerung) und das Absterben der Chondrocyten gebunden ist.

Im Vergleich zum knöchernen Skelett der Wirbeltiere besitzt das Knorpelskelett der Elasmobranchii nur in sehr begrenztem Maße die Fähigkeit zur Regeneration und Heilung. Die zellulären und physiologischen Prozesse zur Vermeidung oder Regeneration von Gewebeschäden sind wenig untersucht und kaum bekannt. In der dritten Studie dieser Arbeit wird in verschiedenen Rochen- und Haiarten ein abnormaler Typ von kalzifiziertem Knorpel als „endophytic masses" (EPMs) beschrieben, der in seiner Morphologie sehr stark von der von Tesserae und anderen bekannten, kalzifizierten Geweben (z.B. den Wirbelkörpern) abweicht. Anhand von computertomographischen,

elektronenmimroskopischen und spektroskopischen (z.B. Raman-Spektroskopie) Daten wird die Anatomie, Ultrastruktur und chemische Zusammensetzung von EPMs in unterschiedlichen Rochen- und Haiarten charakterisiert. EPMs zeigen eine starke Assoziation zu Tesserae, insbesondere zu deren Gelenken, bei denen die ursprünglich unmineralisierte Matrix vollständig durch EPMs mineralisiert ist. EPMs zeigen jedoch nicht die für Tesserae typischen Linien unterschiedlicher Mineraliendichte, die von einem periodischen Wachstum zeugen. Sowohl Tesserae als auch EPMs basieren auf der Mineralisation einer Kollagen Typ-2 Matrix. Jedoch sind die Zellen, die im Kontakt mit EPMs oder vollständig darin eingebettet sind tot, und ihr Zellvolumen ist dicht mit Kristallen gepackt. EPMs sind mineraliendominiert –sie besitzen eine hohe Mineralien- und niedrige, organische Materialdichte– und bestehen aus aufgereihten, großen und licht-doppelbrechenden (unter polarisiertem Licht) Calcium-PhosphatKristallen (wahrscheinlich Brushit). Die angeführten ultrastrukturellen Unterschiede von EPMs und Tesserae belegen, dass es sich um zwei grundlegend verschiedene, aber eng miteinander in Beziehung stehende Gewebsmineralisationen handelt. Die möglichen Gründe der Entwicklung von EPMs, zum Beispiel zur Gewebeunterstützung, insbesondere der Gelenke zwischen Tesserae, als Reparaturmechanismus, oder Anzeichen von gestörten Kontrollmechanismen der Tesseraemineralisation werden diskutiert. Sowohl im Zusammenhang mit der Skelettbiologie der Elasmobranchii im Allgemeinen, als auch unter Berücksichtigung der Beschreibungen mineralisierter Gewebe und deren Reaktion auf Verletzungen in anderen Wirbeltieren.

Table of Contents

1. INTRODUCTION

Vertebrate skeletons exhibit great differences in anatomy, but are largely made of the same building blocks –water, collagens and biominerals. However, our knowledge of the ultrastructure and mechanics of vertebrate skeletal tissues is biased, because the majority of data comes from a small fraction of vertebrates, which are mostly mammalian or avian species exhibiting a bony endoskeleton. This limits our view on the diversity of calcified tissues in vertebrates and our understanding of these tissues in health and disease. Although the number of ultrastructural studies on other vertebrate skeletal tissues –from fish, amphibians, and reptiles– has increased in the last two decades, we are still missing a lot of information on the mechanisms that steer tissue mineralization and skeletal formation in vertebrates. This lack of information is particularly poignant when considering the elasmobranch fishes (sharks, rays and relatives), which represent not only an ancient vertebrate lineage, but also the only vertebrate group with a skeleton made of something other than bone.

The skeleton of vertebrates provides mechanical support to the body and serves as attachment site for muscles and tendons used for active movement. The vast majority of vertebrates (~98%) have stiff, bony endoskeletons. Bone is a dynamic material that is capable of remodeling and repetitive mechanical loads are thought to result in strain and strain rates within bone stimulating the structural adaptation (Turner, 1998; Atkins et al., 2014), but also repairing after damage following loads that exceeded critical forces (e.g. Hoerth et al., 2014). These fish are special, as they do not exhibit a bony endoskeleton, instead their primary skeletal material is unmineralized hyaline-like cartilage, which is a rather flexible material when compared to bone. Cartilage forms the embryonic skeleton of all vertebrates, but whereas it is typically replaced by bone during ontogeny in the rest of the vertebrates, in elasmobranchs it persists a lifetime, forming the adult skeleton (Hall, 2005; Dean & Summers, 2006; Dean et al., 2009). Building an endoskeleton out of cartilage is a counterintuitive strategy, especially in animals with active (i.e. skeleton-damaging) ecologies, because it has several disadvantages in comparison to bone. Elasmobranch cartilage is similar to mammalian cartilage, in being aneural, avascular, and most importantly showing very limited ability to heal (Clement, 1992; Ashhurst, 2004; Hall, 2005). Further, when comparing the material properties, bone is about 10.000 times stiffer than cartilage, providing rigidity to the body and protecting its organs (Fig. A; Ashby et al., 1995).

Sharks and rays stiffen their endoskeleton in a different way; almost the entire endoskeleton (i.e. except for some regions on the vertebrae) is covered in a thin layer of mineralized cartilage. This surface crust is tiled into minute, mineralized platelets, called tesserae, which are several hundred microns wide and deep (~500 x ~300 μm, respectively) (Fig. B; Müller, 1836; Clement, 1992; Dean & Summers, 2006; Dean et al., 2009). The flexible cartilage core and the outer mineralized tesseral layer are wrapped in a fibrous perichondrium (Fig. B; Kemp & Westrin, 1979; Clement, 1992; Dean
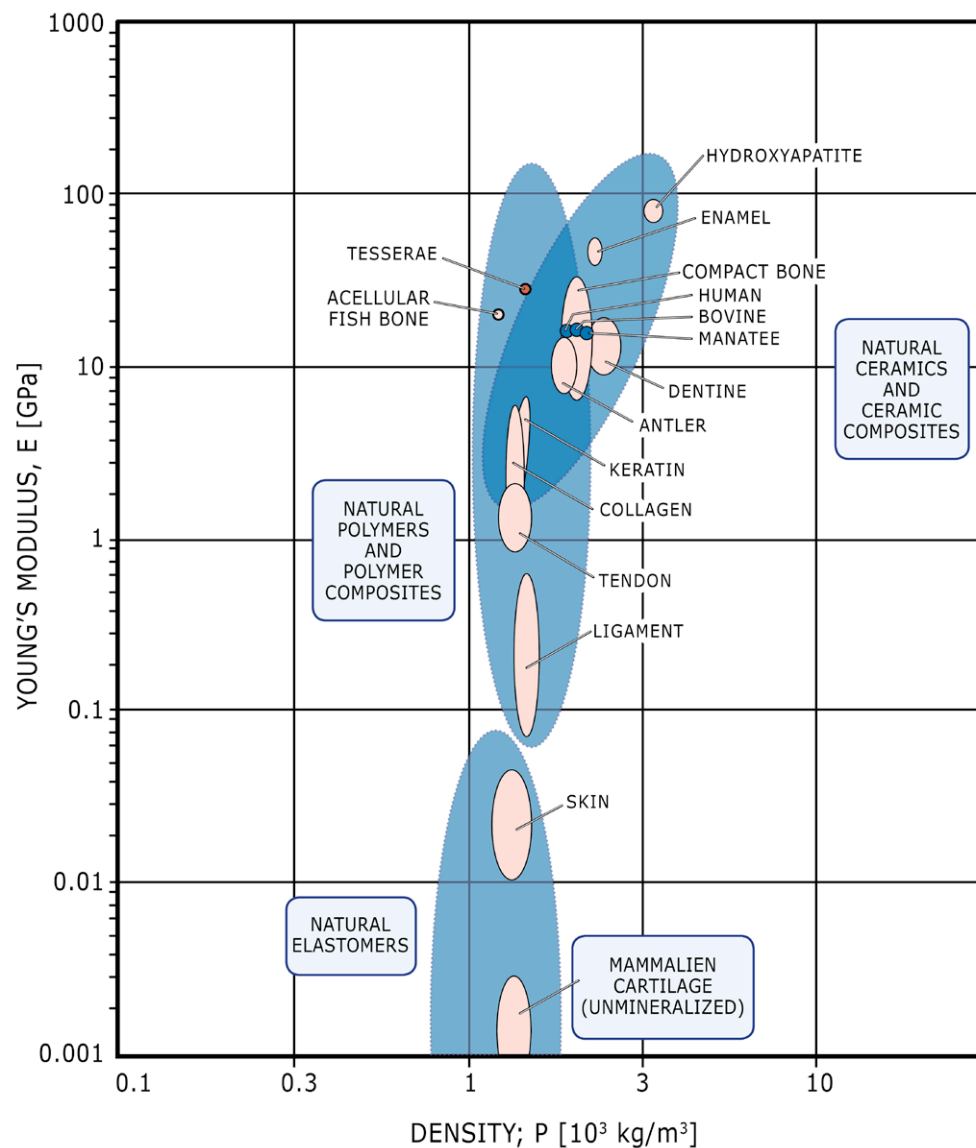
Figure A. Material property chart for natural materials.
Young's modulus is plotted against density, modified from Ashby et al., 1995. Mineralized tissues such as bone and tesserae are several orders of magnitude stiffer than unmineralized cartilage. Tesserae in comparison to mammalian compact bone are lighter with a similar density to unmineralized tissues such as cartilage or skin.

et al., 2009). Tesserae appear not to fuse during age, and remain separated by unmineralized, fibrous cartilage at all times, resulting in a complex tissue architecture of hard tiles linked via soft joints, sandwiched between two different connective tissues, cartilage and perichondrium. Elasmobranch composite endoskeletons are therefore interesting from a biological and engineering perspective (e.g. see Duro-Royo et al., 2015), as they represent a unique tissue architecture of soft and hard tissue among vertebrate skeletons that is in an evolutionary sense –with a fossil record dating back more than 400 mya, (Maisey, 2013; Long, 2015)– a successful alternative to an otherwise fully mineralized bony skeleton.

The combination of a hard tessellated surface sheathing a softer core suggests interesting mechanical properties for whole skeletal elements, as both cartilage and tesserae exhibit very different material properties (Fig. A), but the interaction of these tissues remainded to be elucidated. The elastic modulus (Young's modulus, describing the stiffness) of cartilage is about 3 orders of magnitude smaller when compared with tesserae and other bio-mineralized tissues. Therefore, it can be assumed that without the tesseral layer the cartilaginous skeletal elements would not be sufficiently stiff for swimming or biting, especially in larger sharks and rays. There is some evidence that covering the skeletal surface with a dense array of tesserae shifts the effective stiffness of skeletal elements significantly, in particular when loading is parallel to the tesseral layer (by a max. factor of 45, Liu et al., 2014). In a scenario where skeletal elements would bend under load, the skeletal surface (i.e. the tesseral layer) on one side would be under tension whereas the opposing site would be under compression. Tesserae on the compressive side would be pressed against one another (transferring the load by contact) and prevent further bending (Liu et al., 2014; Fratzl et al., 2016). The tiling of the mineralized crust, the presence of unmineralized joints between tesserae, thereby appears to be crucial as they enable skeletal flexibility and allow for bending of skeletal pieces, in which tesserae on the tensile side would be pulled apart from one another and load is transferred to the fibrous joints. Interestingly, only small portions of the skeleton are mineralized (i.e. the volumetric ratio between cartilage and tesserae), but cross-sections of elasmobranch skeletal pieces suggest that the materials are typically arranged (i.e. oriented in the animal) to maximize the portion of the tessellated layer along the loading axis (i.e. cross-sectional shapes are compressed perpendicular to the loading axis) (Fratzl et al., 2016; Wilga et al., 2016). Although elasmobranchs' skeletons bear a fascinating architecture in which only the surface regions, experiencing the largest compressive/tensile stresses under load, are reinforced with mineralized tissue (tesserae), our understanding of the mechanics is yet limited and is hampered particularly by the lack of ultrastructural data.

Among the musculoskeletal tissues of elasmobranchs, tessellated cartilage may have received the majority of research attention (in comparison to muscles and tendons), however, detailed knowledge about both tesserae development and ultrastructure is scarce (Dean et al., 2009). Tessellated cartilage is known as a feature of elasmobranchs for more than 180 years (e.g. Müller, 1836) and the general organisation of the tissues forming elasmobranch skeletons is known, but very few data of the interactions of tesserae with one another and with associated tissues exist. The combined results of the studies in this thesis help to fill fundmental gaps in our understanding of tessellated cartilage; for example, we were lacking clear descriptions of diagnostic features of tesserae –what tesserae actually are– and even most fundamental questions remained to be answered: "Do tesserae grow in size or in number as the animals age?", "What are intertesseral joints made of and how do tesserae interact with one another?" or "On which collagens are tesserae patterned?".
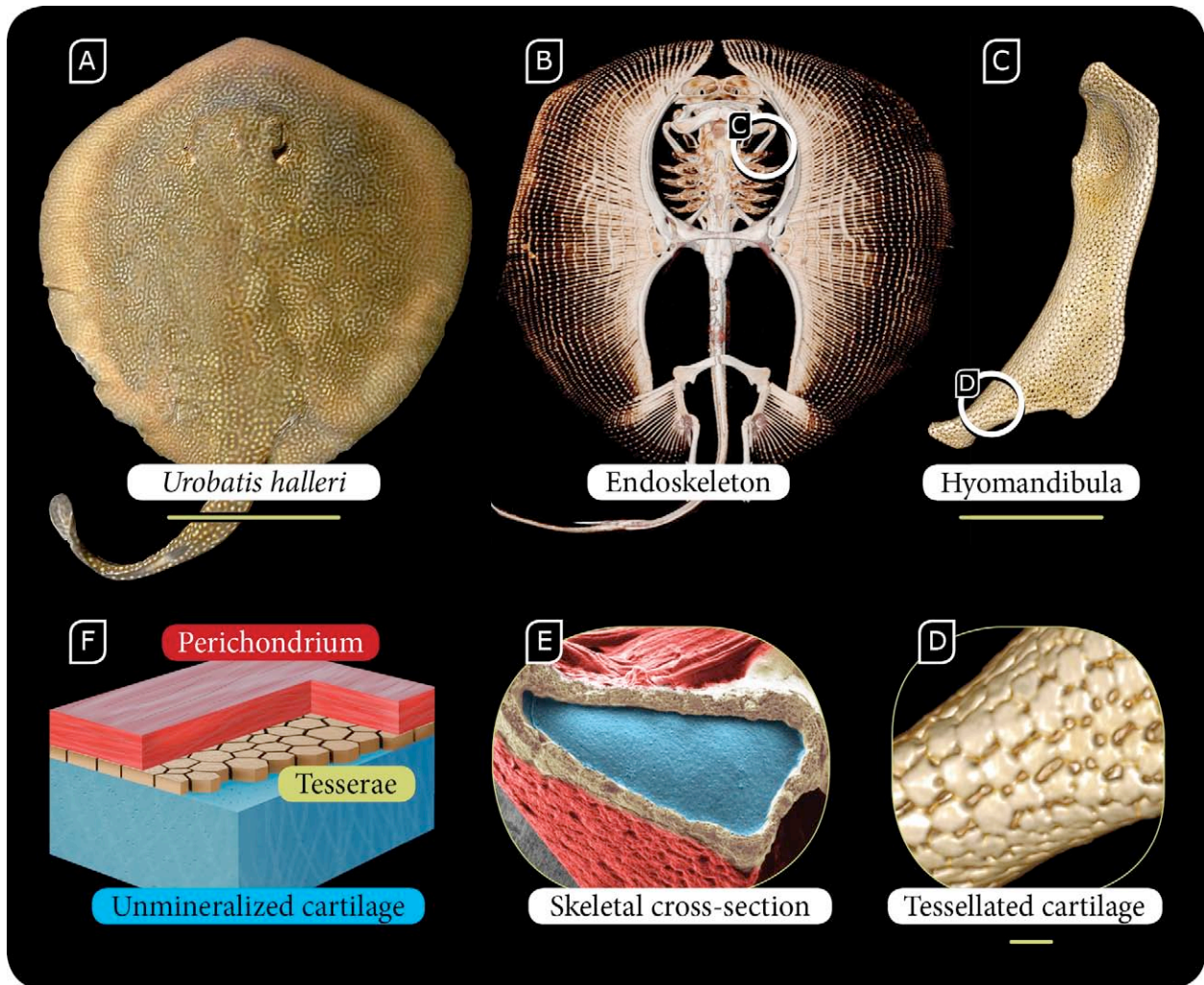
Figure B. Mineralized tessellated cartilage in Elasmobranchs (sharks and rays).

A) Photograph of round stingray *Urobatis halleri*. B) Micro-computed tomography scan of *U. halleri* showing the calcified cartilage in the endoskeleton. C) Micro-CT scan of a hyomandibula, a skeletal element connecting the jaws with the chondocranium (skull) in elasmobranchs. D) Close up of the tessellated pattern of calcified cartilage covering skeletal elements. E) Scanning electron microscopic image of a freeze-dried skeletal cross-section showing the unmineralized hyaline-like cartilage core (blue) sheathed in a tessellated crust of calcified cartilage and wrapped in fibrous perichondrium (red). F) Schematic illustration of the skeletal tissue organization in elasmobranchs with tessellated cartilage sandwiched between unmineralized cartilage and fibrous perichondrium. Scale bars: A) = 10 cm; C) = 10 mm; D) = 500 μm.

2. AIMS

This thesis aims to address these questions (end of previous chapter: Introduction) and provide a holistic view on the tissue composition and development of elasmobranch tessellated cartilage. In the first study of this thesis, an age series of *Urobatis halleri* (for which the majority of developmental data on tesserae from previous studies exists) is used to characterize the development of the mineralized endoskeleton at high resolution, defining inherent and variable ultrastructural features through comparison with numerous shark and ray species' tesserae (Seidel et al., 2016, J Anat). The second study is a comprehensive investigation of the collagenous composition of adult tessellated cartilage from *U. halleri*, addressing the long-standing question of whether the tessellated skeleton is a more bone- or cartilage-like tissue (Seidel et al., 2017, J Struct Biol). The third study comprises an ultrastructural, material and crystallographic description of aberrant, mineralized tissues previously undescribed in elasmobranch that point to a possible damage response in tessellated cartilage and provide insights into vertebrate cartilage mineralization physiology (Seidel et al. 2017, J Struct Biol).

The **first** study aims to characterize the development, ultrastructure and mineral density variation of the mineralized tissue of tessellated cartilage (tesserae) in an age series of round stingray *U. halleri*, including supporting data from other shark and ray species, using backscatter electron microscopy, transmission electron microscopy, micro-computer tomography, histological staining and polarized light microscopy. The objectives are in detail:

- To recognize the mechanisms of elasmobranch cartilage calcification and characterize *U. halleri* tesserae growth and development
- To illustrate the variation in tesserae anatomy (across species) and define diagnostic characters (i.e. intratesseral features) describing what tesserae are
- To identify the nature of intertesseral joints, showing how adjacent tesserae interact with one another and outline/discuss also functional anatomical characteristics
- To capture adult tesserae age changes, shedding light on elasmobranch cartilage physiology, tesserae damage and potential remodeling capabilities
- To show how chondrocytes (or cells in general) are involved in elasmobranch cartilage and tesserae calcification
- To discuss commonalities and differences to other vertebrate mineralized tissues.

The **second** study aims to reveal the type(s) of skeletal tissue(s) forming elasmobranch tessellated cartilage and in particular pattern(s) tesserae mineralization, using immunohistochemistry, electron microscopy, and histological staining methods. The objectives are in detail:

- To characterize the collagenous composition of adult tesserae in round stingray *U. halleri*, in particular in those intratesseral regions exhibiting diagnostic characters of tesserae described in the previous study

- To identify the unmineralized fibrous material in the intertesseral joints linking adjacent tesserae, and the tissue composition and organization of those tesseral regions involved in tesserae interaction (i.e. where tesserae are in direct contact)

- To characterize the tissue(s) associated with tessellated cartilage that is/are involved in elasmobranch skeletal formation and in particular in tesserae's multiple mineralization fronts (outer, perichondral vs. inner, chondral vs. lateral, joint side).

- To depict ultrastructural commonalities and differences (e.g. presence/absence of collagens, cell physiology) to other well-studied vertebrate mineralized tissues (e.g. mammalian calcified cartilage and bone) and discuss their implications on "our" current view on vertebrate cartilage calcification pathways.

The **third** study aims for a better understanding of the physiological and cellular mechanisms steering elasmobranch cartilage calcification in health and disease. Lessons may be learnt from the molecular mechanisms underpinning the transition from cartilage to mineralized tesserae by characterization of anatomical differences between tesserae and an aberrant type of cartilage calcification (EPMs) associated with tesserae in a variety of sharks and rays. We use analytical/ material characterization techniques such as energy dispersive X-ray spectroscopy, selected area electron diffraction, backscatter electron microscopy, transmission electron microscopy, micro-computer tomography μCT, histological staining and polarized light microscopy for ultrastructural characterization of both mineralized and the underlying organic tissue in EPMs and tesserae. The objectives are in detail:

- To characterize the anatomy, mineral composition, crystal orientation and underlying soft tissue composition of EPMs

- To compare EPM ultrastructural data with that of tesserae to discuss possible reasons for EPM development and alternative elasmobranch cartilage calcification pathways

- To outline similarities and differences with existing (pathologic) vertebrate (incl. elasmobranch and mammalian) calcified cartilages in the context of skeletal tissue damage response, repair, and reinforcement.

3.   STATE OF THE ART

3.1   Mineralized cartilage in elasmobranchs (sharks and rays)

The formation of biominerals by living organisms is an extremely widespread phenomenon occurring in animals across all five kingdoms, and some 60 different biominerals are identified (Lowenstam & Weiner, 1989). Mineralized tissues are significantly harder and stiffer when compared to non-mineralized tissues, forming teeth, spines, scales and the endoskeleton in vertebrates. In this thesis, the tissues of the cartilaginous endoskeleton of elasmobranchs are studied (sharks, rays, skates and sawfish) with particular focus on those forming the mineralized, tessellated parts in the periphery of the skeletal elements. In the following, I'll give a brief overview of the types of endoskeletal calcifications occurring in elasmobranch fish, outline the history of scientific study of tesserae, and detail the state of the art knowledge of tessellated cartilage within the contexts of each of the three studies in this thesis.

3.2   Types of mineralized cartilage in elasmobranch fish skeleton

Unlike bony vertebrates possessing a fully mineralized endoskeleton, only small portions of the skeleton of elasmobranchs are mineralized. Many terms have been coined to describe elasmobranch skeletal, mineralized tissues on both the macro- and microscopic scale:

• On the macro-scale, two regular (non-pathologic) types of mineralized cartilages are distinguished: 1) vertebral mineralized cartilage found in the vertebral center and neural arches and 2) tessellated cartilage, a thin mineralized layer found on the surface of/in the remainder of the axial and appendicular skeleton (Benzer, 1944; Ørvig, 1951; Clement, 1992; Dean & Summers, 2006, Dean et al. 2009, 2011).

• On the micro-scale, both vertebral and tessellated cartilages are comprised of three types of calcification that are classified based on their anatomy and location: 1) areolar calcification (vascularized, densely calcified tissue consisting of layers nested like ice cones) forming the 'double cone' of the vertebral body (Ridewood, 1921; Wurmbach, 1932; Hoenig et al. 1982; Peignoux-Deville et al. 1982; Clement, 1992). However, areolar calcification is not particularly concerned in this thesis. The two other types of calcification are 2) prismatic and 3) globular cartilage, both co-occurring in tessellated cartilage, forming a thin calcified skeletal crust broken up in numerous, minute polygonal tiles (tesserae). Prismatic cartilage is characterized by needle-like crystallite arrays at tesserae mineralization fronts, whereas globular cartilage exhibits spherules of mineralized cartilage at tesserae mineralization fronts (Kemp & Westrin, 1979; Clement, 1992; Dean & Summers, 2006, Dean et al. 2009, 2011).

However, our ability to "make sense" of the terminology, for example, when comparing different species, is hampered by these tissue 'types' being defined often by external appearance in 2d slices and not composition or 3d arrangements.

3.3 Elasmobranchs' skeletal tessellated cartilage

The mosaic-like mineralization of tessellated cartilage was recognized early as a unique feature of the endoskeleton of both recent and fossil elasmobranch species ("pflasterförmige Kruste bestehend aus Scheibchen oder Prismen" in Müller, 1836), and because it has never been found in other
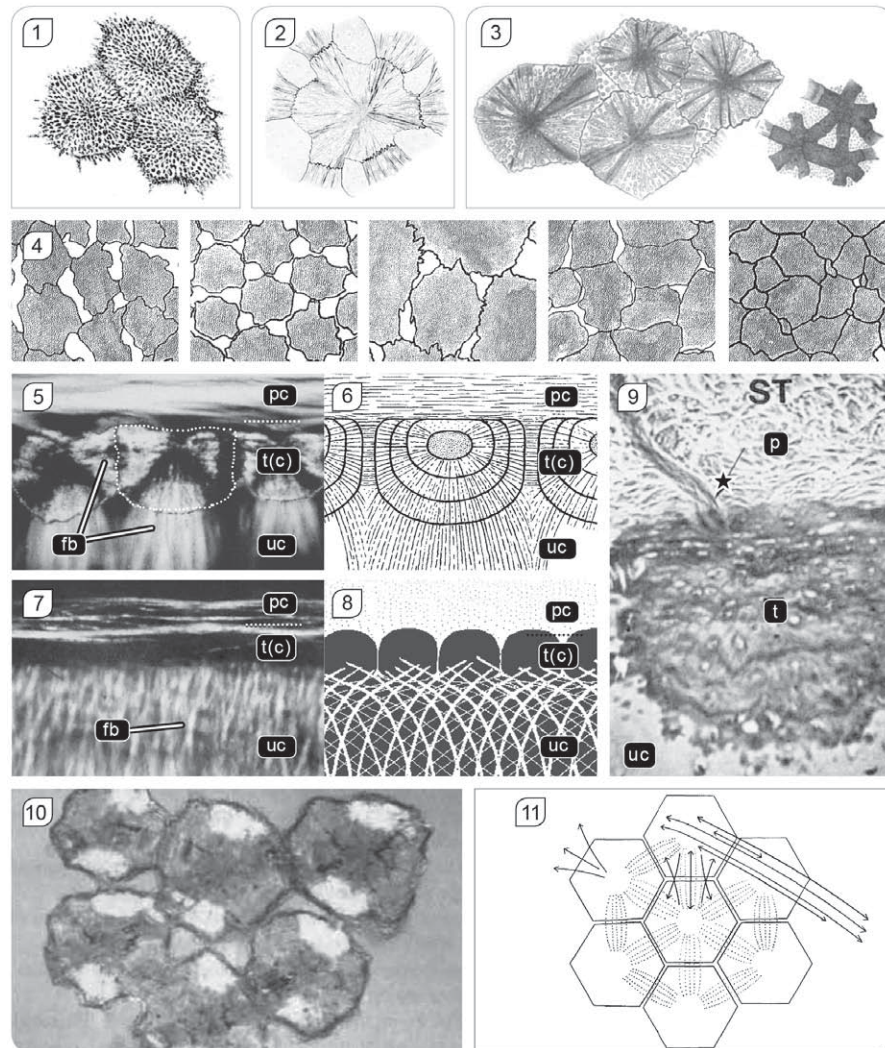
Figure C. Elasmobranchs' skeletal tessellated cartilage.
1-4) Early hand drawn illustrations of the variation in the tiling pattern and tesserae morphology in different shark and ray species. 1) *Myliobatis aquila* in Müller, 1836; 2) *Raja batis* in Leydig, 1852; 3) Unknown spec. in Leydig, 1857; 4) from left to right: *Zygaena malleus*, *Rhinobatis* spec., *Torpedo marmorata*, *Scylium catulus*, *Lamna cornubica* in Roth, 1911. 5-8) Polarized light microscopic images and schematic illustrations of cross-sections of skeletal elements (i.e. tesserae in vertical section). Fibrous material, highly birefringent, links tesserae at their lateral edges to one another and at their chondral edges to the unmineralized cartilage core. 5-6) *Galeus canis* in Schmidt, 1952; 7-8) *Acanthias vulgaris* in Bormuth, 1933. 10-11) Polarized light microscopic image and schematic illustration of tesserae in planar view, showing highly birefringent fibrous material associated with the lateral edges of tesserae and its preferred orientation. 10) *Scyliorhinus canicula* in Clement, 1992; 11) Bargmann, 1939.

vertebrates it is considered to be an apomorphic feature of chondrichthyans (Maisey, 2013; Long et al. 2015). Leydig (1857) reported the size and shape of the tiles forming the tessellation ("Schuppen der Knochenkruste") vary between developmental ages, locations in the skeleton and species. Woodward (1889), as part of his investigations of elasmobranch skeletal cartilage, proposed the term tesserae, which was from then on widely adopted by scientists describing mineralized, tessellated cartilage in sharks and rays. In the late 19th and early 20th centuries a number of tessellated cartilage descriptions from a variety of shark and ray species captured the variation in the tiling pattern and tesserae morphology in hand drawn illustrations (Fig. C1-4) (e.g. Müller, 1836; Leydig, 1852, 1857; Roth, 1911). The overall quality and detail of these illustrations is astounding given the techniques that were available at that time, and besides showing that tesserae vary greatly in size and geometry across species, one of their major merits was to indicate that similar mechanisms of controlling local mineral deposition (by promotion and inhibition) must exist in different shark and ray species. However, the understanding of the inception and growth of the elasmobranch skeleton and tessellated cartilage was largely based on observations and morphological descriptions from adult animals (Dean et al. 2009).

3.4 Ultrastructure and development of tessellated cartilage

The characterization of the ontogeny and ultrastructure of an age series of tessellated cartilage from round stingray *U. halleri* is subject of the first study in this thesis – "Ultrastructural and developmental features of the tessellated endoskeleton of elasmobranchs (sharks and rays)". In the following section I provide an overview of the available data summarizing the development of tessellated cartilage, including descriptions of mineral formation and tesserae ultrastructure, mechanisms of mineralization control, and the gross organisation of the skeletal tissues associated with tesserae.

3.5 Tesserae development

There are assumptions that the tesserae of young animals are quite different from the abutting, polygonal tesserae of adults, however the former have only been anecdotally described, and the steps involved in their development into adult tesserae were unknown. Embryonic elasmobranch skeletons are purely cartilaginous and unmineralized, and it appears that the calcified tessellation first arises close to parturition/hatching (in *U. halleri*, Dean et al. 2009; in *Scyliorhinus canicula*, Lorch, 1949 and Enault et al. 2015). Mineralization first appears in form of clusters of isolated nuclei of mineralized cartilage (globular cartilage), separated from one another by unmineralized cartilage, and appearing to be associated with distinct groups of chondrocytes exhibiting up-regulated ALP activity in pre-tessellate cartilage (Lorch, 1949; Eames et al. 2007). As the globules of calcified cartilage increase in size and number they appear to fuse, and by periodic apposition of new globular calcified cartilage individual tesserae are formed (Benzer, 1944; Ørvig, 1951; Kemp & Westrin, 1979; Dean et al. 2009). Whereas

cartilage is characterized by interstitial growth, tesserae appear to grow exclusively by accretion of new mineral to existing tesserae edges (Dean et al. 2009).

As animals age (and tesserae grow), tesserae appear to come in contact with the fibrous perichondrium which is reflected in the ultrastructure of older tesserae. In association with the perichondrium, slender, needle-like crystals form rough tesseral edges, which are distinct from the (embryonic, lateral and) rather smooth chondral edges characterized by globular calcification (Fig. D2-3) (Ørvig, 1951; Kemp & Westrin, 1979). Within adult tesserae, there are ultrastructural differences between the outer, perichondral and inner, chondral region, in that the former lacks basophilic contour lines (Liesegang lines; described in detail below) (Kemp & Westrin, 1979). Additionally, lacunar spaces in the outer, perichondral zone of adult tesserae, exhibit flat and compressed cells (and lacunar spaces) similar to perichondral fibroblasts (Tretjakov, 1926; Kemp & Westrin 1979), whereas those of the inner, chondral zone appear more roundish/oval similar to those in the unmineralized cartilage core (Kemp & Westrin, 1979; Clement, 1992; Dean et al. 2010). These differences lead to the description of two tesseral portions: a perichondral, cap and chondral, body zone (Kemp & Westrin, 1979), suggesting that tesserae are not just simple blocks of mineralized cartilage and two distinct mechanisms of tessellated cartilage growth may exist – the development of tesserae and these two zones, however, was never investigated in detail. The study of tesserae from varying specimens at different ages, and from different skeletal locations, and the use of different techniques with changing perspectives have limited our understanding of the development and ultrastructure of tessellated cartilage. Furthermore, as elasmobranchs' perichondrium and cartilage were believed to be patterned on different collagens –type-I and type-II collagen, respectively– like mammals' and other vertebrates', it has been debated whether tesserae are more like bone (Coll I) or calcified cartilage (Coll II) (see below).

3.6   The control of cartilage mineralization

There is growing evidence that chondrocytes in unmineralized cartilage orchestrate the mineralization of tessellated cartilage by controlling where mineral is deposited. This is suggested by observations of up-regulated alkaline phosphatase (ALP) expression and extracellular concentration in pre-tessellate tissue/locations (Lorch, 1949; Eames et al. 2007) and in adult tessellated cartilage at tesserae's chondral borders, where ALP is believed to cleave 'inactive' phosphate polymers to initiate apatite bio-mineralization (Omelon et al. 2014). The control of tesserae growth by chondrocytes is further supported by cytoplasmic expression of other proteins linked to mammalian skeletal growth and mineralization, including: calcium- binding osteopontin (OPN) and osteonectin (ON, also known as SPARC) (in *S. canicula*: Egerbacher et al. 2006, although ON & OPN expression occurred also at non-mineralizing regions; Venkatesh et al. 2014), parathyroid-related protein regulating chondrocyte differentiation (PTHrP; *M. antarcticus*: Fig. 2b in Trivett et al. 2002; Vortkamp et al. 1996), and matrix

Gla protein preventing ectopic calcification (MGP; *P. glauca*: Fig. 3H in Ortiz-Delgado et al. 2005) (see Dean et al. 2015 for review).

Chondrocytes bordering tesseral edges likely also control mineralization inhibition (e.g. at intertesseral joints) possibly by regulating the degradation of proteoglycans (from long to short amino acid chains) in the Coll II matrix, which were shown to inhibit mineralization in vitro (Gelsleichter, 1995) and progressively decrease in concentration/length towards calcification fronts, to be almost completely degraded in mineralized cartilage (Takagi et al. 1984). Further evidence is based on the fact that chondrocytes are incorporated alive into tesserae via a process of encapsulation, in which globular mineralized tissue engulfs cells into lacunar spaces in the mineralized matrix (Fig. D1) (Tretjakoff, 1926; Halstead, 1974; Kemp & Westrin, 1979; Takagi et al. 1984; Bordat, 1988; Clement et al. 1992; Dean et al. 2008, 2009, 2010). The intratesseral cells appear to be capable of maintaining a 'pericellular envelope' of unmineralized cartilage (Kemp & Westrin, 1979), and likely remain alive due to the continuity of the uncalcified ECM in canalicular networks (i.e. inter-lacunar passages), which may allow for nutrient flow and signaling between cells (Fig. D1) (Dean et al. 2010).
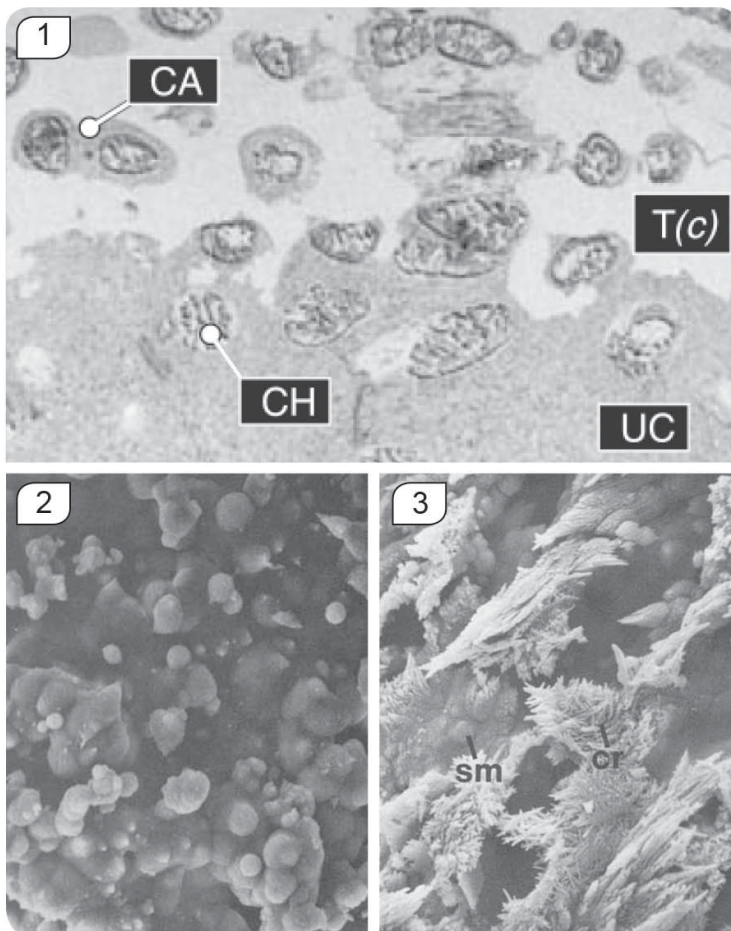
Figure D. Chondrocytes and cartilage mineralization.

1) Scanning electron microscope (SEM) image of tesserae in a vertical view showing chondrocytes become embedded in the mineralized matrix, and appear to maintain a pericellular, unmineralized zone of cartilage between cell wall and lacunar wall (from Dean et al. 2009) 2-3) SEM image of 2) globules of calcified cartilage on the chondral surface of tesserae (globular cartilage) and 3) slender, needle-like crystals forming rough perichondral tesseral edges (prismatic cartilage) (Kemp & Westrin, 1979).

3.7 Tesserae ultrastructure – Liesegang lines

Early light microscopy images and illustrations, in particular Tretjakov's (1926) detailed illustrations of demineralized tesserae sections in vertical and planar view, showed fine details of intratesseral features of the organic matrix and suggested that the heterogeneity of the soft tissue may be reflected in mineral density variation in tesserae (Fig. E1) (*Raja clavata*, Tretjakov, 1926; *Myliobatis aquila*, Bargmann, 1939; *Galeus canis*, Schmidt, 1952). Ørvig (1951) provided extensive drawings and images of sections of tesserae from both fossil and recent specimens, showing that tesserae exhibit repetitive motives of parallel and concentric lines appearing to mirror a tessera's edges (Fig. E2). He interpreted these basophilic lines as growth and developmental pattern, representing variations in the degree of calcium salt depositions, concluding that these lines mirror individual, successive calcifications events (Ørvig, 1951).

The phenomenon of periodic and concentric mineral precipitation bands –variously called Liesegang 'lines', 'rings' or 'bands'– has been recognized in a variety of biological, chemical and geological systems for over a century (Liesegang, 1907; see Stern, 1967 for a bibliography of Liesegang rings). Liesegang lines appeared to be a regular feature of tesserae and have been observed in both recent and extinct elasmobranch species (e.g. plates 6–7 in Ørvig, 1951; figs 2–7 in Applegate, 1967; fig. 16 in Kemp & Westrin, 1979; fig. 10 in Peignoux-Deville et al. 1982; fig. 2 in Takagi et al. 1984; fig. 6 in Bordat, 1988; plate 5 in Clement, 1992). However it was not clear whether these lines were variations in elemental composition or mineral density or both, when shown in demineralized histology sections (Applegate, 1967; Bordat, 1988; Kemp & Westrin, 1979; Takagi et al. 1984; Clement, 1992) or transmitting (and polarized) light microscopy imaging of mineralized sections (Peignoux-Deville et al. 1982). Johanson et al. (2010) presented the first backscattered SEM image suggesting a heterogonous mineral distribution in a tessera of "chondrichthyan cartilage" (species unknown, pers. comm.) (Fig. E3; fig. 7F in Johanson et al. 2010).

3.8 Tessellated cartilage and associated tissues interaction

Elasmobranch tesserae are sandwiched between the cartilaginous core and the overlying fibrous perichondrium wrapping each skeletal element (Leydig, 1852; Benzer, 1944; Applegate, 1967; Kemp & Westrin, 1979; Clement, 1992; Dean et al. 2009). Tesserae are anchored to these tissues and firmly held in place by fibres on both chondral and perichondral side (Fig. C5-8) (Bormuth, 1933; Bargmann, 1939; Schmidt, 1952; Kemp & Westrin, 1979; Clement, 1992). The latter exhibits thick fibre bundles inserting from the perichondrium into tesserae (Fig. C9) (Ørvig, 1951; Kemp & Westrin, 1979), resembling 'Sharpey's fibers' typically seen in vertebrate bony tissues (where mammalian tendons attach to bone and dental ligament attaches to teeth) (Sharpey, 1848; Kölliker, 1864; Boyde & Jones, 1968; Jones & Boyde, 1974). Tesserae can abut against one another at their lateral edges (e.g. Leydig, 1852; Roth,

1911), and in regions where tesserae are not in direct contact they appear to be linked to one another via a fibrous tissue composed of a highly ordered and oriented fibrous matrix, that is birefringent using polarized light microscopy (Fig. C10-11) (Tretjakoff, 1926; Bormuth, 1933; Bargmann, 1939; Schmidt, 1952; Bordat 1988; Clement, 1992).
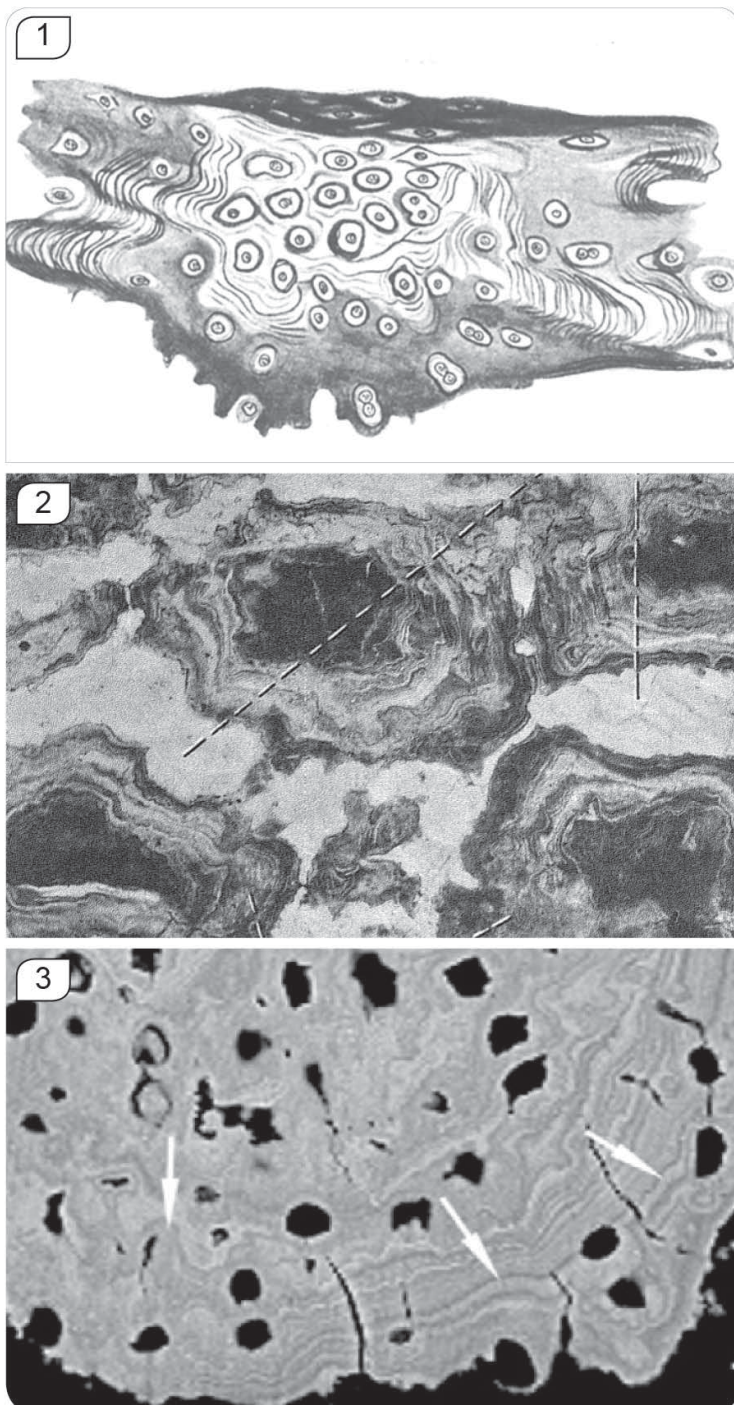
Figure E. Internal ultrastructural features of tessellated cartilage.

1) Detailed illustration of intratesseral features in a vertical section of a tessera from *Raja clavata* (Tretjakov, 1926). 2) Adjacent tesserae from a Triassic species (*Paleobatis polaris*) showing layers (Liesegang lines) in the mineralized matrix mirroring the tesseral shape, suggesting tesserae grow by deposition of new material on existing edges of tesserae (Ørvig, 1951). 3) Until today, the first image of Liesegang lines in a tessera captured with backscattered SEM (Johanson et al. 2010).

3.9 Calcified cartilage or bone? – Collagens in elasmobranch tessellated cartilage

The collagenous compositions of adult tesserae and associated tissues of *U. halleri* is subject of the second study in this thesis: "Calcified cartilage or bone? – collagens in the tessellated endoskeleton of cartilaginous fish (sharks and rays)". Tesserae are sandwiched between two types of soft tissues, perichondrium and cartilage, fuelling the debate about the origin of the underlying soft tissue that patterns tesserae mineralization. Both perichondrium and cartilage exhibit different collagenous compositions (largely type-I and type-II collagen, respectively), leading to the question whether tesserae are more like bone or calcified cartilage. In the following section I provide an overview of the constituents of skeletal tissues in elasmobranchs and vertebrates, in general.

3.10 The building-blocks of vertebrate mineralized tissues

Vertebrate mineralized tissues require the presence of organic templates guiding the growth of the mineralized tissue by patterning mineral deposition on protein-based macromolecules, typically collagen fibrils and fibers. A collagenous framework is not only a prerequisite for crystal deposition, but it also plays a vital role in determining the mechanical properties of the tissue (Landis et al. 1996; Ferguson et al. 2003; Fratzl et al. 2004; Gupta et al. 2005; Seto et al. 2008). Mineralized skeletal tissues, such as bone and calcified cartilage use the same mineral a carbonated apatite with high ion-substitution potential (Urist, 1961; Applegate, 1967; Fratzl et al. 2004; Wopenka & Pasteris, 2005), and varying mineral densities and crystal orientations (Landis et al. 1996; Roschger et al. 1998; Zizak et al. 2003).

In contrast, there is largely a dichotomy in the organic building blocks, because mainly two collagen types are used to pattern the majority of vertebrate skeletal tissues: the mineral deposition in bone formation is patterned on collagen type-I (Coll I) (Landis et al. 1996; Fratzl et al. 2004). About 90% of the organic bone mass is collagen type-I, the rest are non-collagenous proteins (e.g. glycoproteins, osteopontin, osteonectin) (Reinholt et al. 1990; Denhardt & Guo 1993; Termine et al. 1981; Curry 2008). In contrast, in unmineralized hyaline cartilage, representing the majority of skeletal cartilage in vertebrates (see below; Poole 1997; Hunziker 2002) and mineralized cartilage, collagen type-II (Coll II) is the major organic component, often associated with glycosaminoglycans (e.g. chondroitin sulfate) (Fratzl, 2008).

3.11 The diversity of vertebrate skeletal tissues

The variations in skeletal tissue composition within vertebrates are immense and next to bone and cartilage, many intermediate tissues are described (e.g. endochondral, perichondral, intramembranous and chondroid bone; calcified cartilage; chondroid; hyaline, fibro or elastic cartilage). These tissue variations form a continuum and sometimes aren't perceptibly different from one another, but

certainly bone and cartilage are quite distinct and form the extremes (Beresford, 1981; Hall, 2005; Witten et al. 2010; Cole 2011). Cell type, density and shape (e.g. chondrocytes, osteocytes, osteoblasts: Farnum et al. 2002; Witten et al. 2010; Cooper et al. 2013), as well as cell products (proteoglycans and collagens, Poole & Pidoux, 1989; mineral deposition promoting proteins, Termine et al. 1981) are the major defining parameters of skeletal connective tissues.

3.12 Collagens in vertebrate cartilage and bone

Bone, for example, is an exclusive vertebrate tissue and subdivided in three major types, all of which are patterned on Coll I: 1) endochondral bone [develops from cartilage and represents the major bony tissue in vertebrate skeletons], 2) perichondrial bone [develops from the perichondrium], and 3) intramembranous bone [develops in mesenchymal cells]. In contrast, cartilage is subdivided in 3 types based on the collagens it is composed of and the differences in tissue histology: 1) hyaline cartilage [a collagen type-II based tissue with a high proteoglycan and water content, forming the embryonic endo-skeleton and articulations in adult vertebrates], 2) elastic cartilage [rich on elastin and elastic fibers, present in the outer ear, pinnae of mammals, in bones or joints] and 3) fibrous cartilage [rich on collagen type-I, found in ligaments and tendons]. Further, in endochondral bone formation, the mineralization of cartilage at the bone-cartilage-interface region is patterned on collagen type-II, and collagen type-X was also identified in calcified cartilage but appears to be absent in both unmineralized cartilage and bone (Poole & Pidoux, 1989; Gannon et al. 1991). In summary, characterizing a tissue based on the presence of collagens can be quite challenging due to the many intermediate tissues and the vast number of collagen types that exist (Donoghue et al. 2006; Hall, 2005; Hall & Witten, 2007; Fratzl 2008).

3.13 Collagens in tessellated cartilage

The building blocks of the organic tissue –the collagens– that pattern tesserae and connect them with surrounding tissues have never been clarified unambiguously. It is not clear whether elas-mobranch tessellated cartilage is patterned on Coll I and therefore bone-like, on Coll II and therefore effectively calcified cartilage, or on some hybrid combination of collagens (e.g. calcified cartilage with a "thin veneer of bone" sensu Kemp & Westrin, 1979), similar to the intermediate tissue architecture of chondroid/chondroid bone (Beresford, 1981; Witten & Hall, 2002; Witten et. al, 2010).

Previous studies on the collagenous composition of tessellated cartilage showed contrary results, often involved techniques that did not allow localization of collagen types in specific regions, because they were largely not aimed at determining the collagen types in tesserae specifically. Some studies used homogenized tissue and/or non-specific "cartilage tissue" (i.e. possibly mixing cartilage, perichondrium and tesserae: Peignoux-Deville et al. 1982; Rama & Chandrakasan, 1984; Sivakumar & Chandrakasan, 1998; Mizuta et al. 2003), while others investigated non-tessellate adult cartilages (Conrad et al. 1981),

embryonic pre-tessellate cartilage (Eames et al. 2007), or tesserae in early developmental stages (Enault et al. 2015). As a result, it was unclear on which tissue types tesserae growth is patterned, limiting our ability to compare tesserae with other mineralized vertebrate skeletal tissues and defining similarities and differences in cartilage ultrastructure and mineralization pathways.

3.14   Ectopic mineralization as a response to damage in elasmobranch skeletons

The third chapter of this thesis comprises an ultrastructural analysis of a previously unrecognized, aberrant type of cartilage mineralization called endophytic masses (EPMs), associated with tessellated cartilage in several shark and ray species. Elasmobranch skeletons appear to have limited healing capability (Ashhurst, 2004; the first study) and their tissues' mechanisms for avoiding damage or managing it when it does occur are largely unknown. In this way, the ultrastructural differences between tesserae and EPMs, with the latter appearing to form in response to tissue damage or breakdown of mineral inhibiting mechanisms, offer valuable insights into cartilage mineralization in health and disease. In the following section I provide an overview of the known ectopic mineralizations occurring in sharks and rays, and start with a brief comparative overview of the remodeling properties of bone and (calcified) cartilage.

3.15   Remodeling of bone, but not cartilage

Bone is a dynamic material with the ability to remodel its mineralized matrix and strengthen the skeleton to adapt to mechanical loading, but also to repair mineralized tissue damage (e.g. cracks) by absorbing old, fractured and subsequent depositing of new mineralized matrix. These processes were shown to work only in non-critical (< 1mm) size defects, for example, where mineralized and heterogeneous matrix spans and stabilizes the fracture gaps and facilitates repair in bone calluses (Hoerth et al. 2014). A prerequisite for those remodeling processes is sensing where damage occurs, which in bone is supposedly regulated by osteocytes housed in lacuno-canalicular networks (Bonewald, 2011). Elasmobranch cartilaginous skeletons, however, lack evidence of tesserae remodeling and cannot repair tesserae in response to damage as shown in-vivo with experimental fracture of skeletal elements, leading to unmineralized cartilage callus formation, but not healing (Ashhurst, 2004; Clement, 1986, 1992). The unmineralized lacuno-canalicular network in tesserae (see Fig. D1 and "The role of chondrocytes in cartilage mineralization") may allow signaling between intra-tesseral cells and those of the surrounding matrix, however, there is no evidence to date of cell-cell communication in tessellated cartilage.

3.16   Types of ectopic mineralization in elasmobranchs

There are relatively few reports on mineralization that is ectopic (at an abnormal place) in elasmobranch fish compared to the number of studies on mammalian aberrant mineralized tissues. Those

described in elasmobranchs are often characterized in a manner of gross tissue organisation on the sub-centimetre scale. For example, some authors have observed mineralized fusions of tesserae (Applegate, 1967; Maisey, 2013), or massive "hypercalcified" masses on the perichondral side of the tesseral layer (Fig. 10 in Maisey, 2013) resulting in continuously mineralized skeletal crusts. These types of mineralization are described in both recent and fossil elasmobranchs, and little is known about their ultrastructure, and even less about their growth.

Another idiopathic mineralization type is often observed in correlation with spinal deformation in sharks that were caught by net fishing and held in captivity. It is characterized by mineralized masses encasing portions of the vertebral column, occurring within vertebrae and outside the notochordal sheath (Hoenig & Walsh, 1983; Officer et al. 1995; Porter et al. 2006; Huber et al. 2013). Animals with this ectopic mineralization often have buckled backs and whereas the spinal deformation is likely coincident with tissue damage, it is not clear whether the perichondral mineralization is caused by breakdowns of mechanisms regulating mineral inhibition or tissue damage. Unfortunately, data on the ultrastructure of these mineralized tissues is scarce and comparisons –similar to those made in the discussion of the third study of this thesis– with other vertebrate ectopic and pathologic mineralization (e.g. chondrocalcinosis, osteophytes) cannot be made.

ABBREVIATIONS

Methods

BSE	backscatter electron microscopy
EDS	energy dispersive X-ray spectroscopy (also EDX)
IHC	immunohistochemistry
µCT	micro-computed tomography
PLM	polarized light microscopy
SAED	selected area electron diffraction (also SAD)
SEM	scanning electron microscopy
sr-µCT	synchrotron radiation-µCT
TEM	transmission electron microscopy

Tesserae

bl	bright laminae in spokes
bz	body zone
ch	chondrocyte (also CH)
Coll xy	collagen type-xy

cz	cap zone
dl	dark laminae in spokes
DW	disc width
fas	fiber attachment surface
fb	fiber bundles spanning the ifz
fls	filled lacunar spaces also FLS
ics	intertesseral contact surfaces at the icz
icz	intertesseral contact zone border the iss
ifz	intertesseral fibrous zone at the itj
ij	intertesseral junction
iss	interstitial space between ics
is	inter-spoke area
itj	intertesseral joint
ja	joint axis
jc	joint- adjacent cells
ls	lacunar spaces (also LS)
p	perichondrium (also P, PC)
sp	spokes
T	tessera/e (also t & tc)
Tr	trabeculae
UC	unmineralized cartilage

Other tissues

ACC	articular calcified cartilage
Chc	chondocranium
CR	crystals
EIM	exophytic idiopathic mineralization
EPMs	endophytic masses
FHB	femoral head bone
HAC	hyaline articular cartilage
HDMP	hyperdense mineralized protrusions
JC	joint capsule
Ri	ribs
Ros	rostrum
SCB	subchondral bone
Vb	vertebrae

4. Ultrastructural and developmental features of the tessellated endoskeleton of elasmobranchs (sharks and rays)

Ronald Seidel,[1] Kady Lyons,[2] Michael Blumer,[3] Paul Zaslansky,[4] Peter Fratzl,[1] James C. Weaver[5] and Mason N. Dean[1]

[1]*Department Biomaterials, Max Planck Institute of Colloids and Interfaces, Potsdam, Germany*
[2]*Department of Biological Sciences, California State University Long Beach, Long Beach, CA, USA*
[3]*Division of Clinical and Functional Anatomy, Medical University of Innsbruck, Innsbruck, Austria*
[4]*Julius Wolff Institute, Berlin-Brandenburg Center for Regenerative Therapies (BCRT), Charité Universitätsmedizin Berlin, Berlin, Germany*
[5]*Wyss Institute for Biologically Inspired Engineering, Harvard University, Cambridge, MA, USA*

ABSTRACT

The endoskeleton of elasmobranchs (sharks and rays) is comprised largely of unmineralized cartilage, differing fundamentally from the bony skeletons of other vertebrates. Elasmobranch skeletons are further distinguished by a tessellated surface mineralization, a layer of minute, polygonal, mineralized tiles called tesserae. This 'tessellation' has defined the elasmobranch group for more than 400 million years, yet the limited data on development and ultrastructure of elasmobranch skeletons (e.g. how tesserae change in shape and mineral density with age) have restricted our abilities to develop hypotheses for tessellated cartilage growth. Using high-resolution, two-dimensional and three-dimensional materials and structural characterization techniques, we investigate an ontogenetic series of tessellated cartilage from round stingray *Urobatis halleri*, allowing us to define a series of distinct phases for skeletal mineralization and previously unrecognized features of tesseral anatomy. We show that the distinct tiled morphology of elasmobranch calcified cartilage is established early in *U. halleri* development, with tesserae forming first in histotroph embryos as isolated, globular islets of mineralized tissue. By the sub-adult stage, tesserae have increased in size and grown into contact with one another. The intertesseral contact results in the formation of more geometric (straight-edged) tesseral shapes and the development of two important features of tesseral anatomy, which we describe here for the first time. The first, the intertesseral joint, where neighboring tesserae abut without appreciable overlapping or interlocking, is far more complex than previously realized, comprised of a convoluted bearing surface surrounded by areas of fibrous attachment. The second, tesseral spokes, are lamellated, high-mineral density features radiating outward, like spokes on a wheel, from the center of each tessera to its joints with its neighbors, likely acting as structural reinforcements of the articulations between tesserae. As tesserae increase in size during ontogeny, spokes are lengthened via the addition of new

lamellae, resulting in a visually striking mineralization pattern in the larger tesserae of older adult skeletons when viewed with scanning electron microscopy (SEM) in backscatter mode. Backscatter SEM also revealed that the cell lacunae in the center of larger tesserae are often filled with high mineral density material, suggesting that when intratesseral cells die, cell-regulated inhibition of mineralization is interrupted. Many of the defining ultrastructural details we describe relate to local variation in tissue mineral density and support previously proposed accretive growth mechanisms for tesserae. High-resolution micro-computed tomography data indicate that some tesseral anatomical features we describe for *U. halleri* are common among species of all major elasmobranch groups despite large variation in tesseral shape and size. We discuss hypotheses about how these features develop, and compare them with other vertebrate skeletal tissue types and their growth mechanisms.

Keywords: calcified cartilage; development; elasmobranchs; skeleton; tesserae; ultrastructure.

4.1 INTRODUCTION

Whereas the vast majority (~ 98%) of vertebrate species have bony endoskeletons, the skeletons of elasmobranch fishes (sharks, rays and relatives) are comprised largely of unmineralized hyaline-like cartilage (Leydig, 1852; Hall, 2005; Currey, 2002; Atkins et al. 2014). As unmineralized cartilage is considerably less stiff than bone (Ashby et al. 1995), it is remarkable that sharks and rays represent such an evolutionary successful taxon, constituting some of the largest and fastest marine apex predators for more than 400 million years (Maisey, 2013; Long et al. 2015). The high performance of elasmobranch cartilage is surely linked to the fact that the majority of the skeleton is essentially armored: the uncalcified cartilaginous core of each piece of the skeleton is covered by a layer of mineralized tiles called tesserae, and then further wrapped in an outer sheath of fibrous connective tissue (perichondrium; Fig. 1; Leydig, 1852; Benzer, 1944; Applegate, 1967; Kemp & Westrin, 1979; Clement, 1992; Dean et al. 2009).

The mineralized cortex of elasmobranch cartilage has profound functional implications, reinforcing the skeleton and providing a stiff surface for muscular attachment. To cope with the mechanical demands of the adult animal, most vertebrates almost completely replace their embryonic cartilaginous skeletons with bone during development. Bone is a dynamic material where cells orchestrate removal, deposition and remodeling of mineralized tissue, allowing ongoing growth and damage repair, even under the regular loading regimes of daily life (Hall, 2005; Currey, 2002; Atkins et al. 2014). In contrast, cartilage has limited repair ability (Ashhurst, 2004; Hall, 2005) and, when mineralized, apparently cannot remodel; hence, a continuous, mineralized cartilage cortex could grow only by apposition and,

therefore, only thicken. The tessellation of the elasmobranch skeleton, however, provides space for growth in between tesserae, and it is theorized that new mineralized tissue is deposited at tesseral edges during development (Clement, 1992; Dean et al. 2009). The combination of mineralized tissue and unmineralized intertesseral joints is, therefore, vital to elasmobranch skeletal biology, providing both cortical stiffness for mechanical function and room for interstitial growth (between tesserae; Clement, 1992; Dean et al. 2009), while also likely permitting flexibility under some loading conditions (Liu et al. 2010; Fratzl et al. 2016).

The growth and mechanics of tessellated cartilage skeletons rely on the maintenance of linked, but separated, tiles; however, it remains unclear how the tessellated pattern is established and maintained, how tesserae interact during growth, and how tesseral morphology changes with age. There is some suggestion that the tessellations of young animals are quite different from the abutting, polygonal
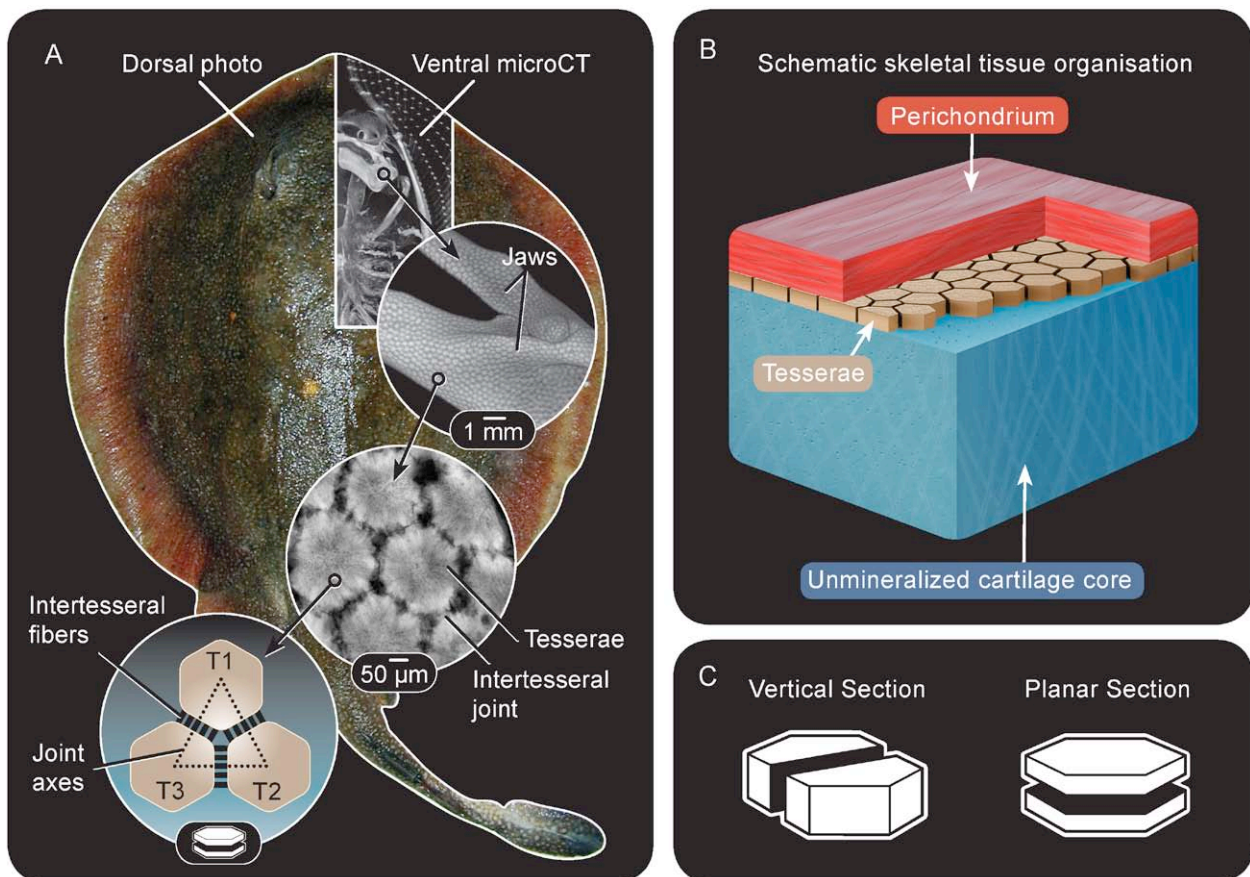
Fig. 1 Tessellated endoskeleton of elasmobranchs (sharks and rays).
(A) Photograph of round stingray *Urobatis halleri* and insets of micro-computed tomography (µCT)-images showing the jaws, covered in tesserae. The final inset shows a schematic view of three tesserae (T1–3) and their non-mineralized fibrous connections. (B) Schematic of the organization of elasmobranch tessellated cartilage: skeletal elements are comprised of an uncalcified cartilage core and armored with a hard outer layer of mineralized tesserae and unmineralized fibrous perichondrium. (C) These icons are used throughout the article to indicate the tesseral views and sectioning planes used in this study, providing consistent anatomical perspectives.

tiles of adults. Embryonic elasmobranch skeletons are uncalcified, and it appears that tessellation first arises close to parturition/hatching, in the form of clusters of isolated nuclei of mineral, associated with groups of chondrocytes and alkaline phosphatase (ALP) activity, and separated from one another by unmineralized cartilage (Benzer, 1944; Ørvig, 1951; Eames et al. 2007; Maisey, 2013). However, young animal tessellations have only been anecdotally described and the steps involved in their development into adult tesserae are unknown.

As a consequence, we are missing crucial steps in our understanding of tesseral development and mineralization, largely due to research being focused either only on a narrow age range (e.g. young, pre-tessellate animals: Eames et al. 2007; early tessellate animals: Enault et al. 2015; adult animals: Schmidt, 1952; Moss, 1968; Kemp & Westrin, 1979; Clement, 1992) or on extinct tissues, where species' age determination is more speculative (e.g. Ørvig, 1951; Schaeffer, 1981; Maisey, 2013; Long et al. 2015). Tesserae are small (typically less than 500 µm in all dimensions) and numerous, and available data suggest there could be a great variability of adult tesseral sizes and shapes across the skeletal surface and species. However, cross-study comparisons are nearly impossible, as there has been no standardization in the sectioning planes, skeletal elements or species investigated. As a result, our understanding of tesseral ultrastructure has also suffered and been limited entirely to two-dimensional perspectives with little anatomical context.

Here, we aim to characterize the development of tesserae at the ultrastructural level to render a three-dimensional concept of tesserae and define diagnostic structural features. We use polarized light microscopy (PLM), electron microscopy [scanning electron microscopy (SEM), transmission electron microscopy (TEM)] and X-ray micro-computed tomography (laboratory and synchrotron radiation-based micro-computed tomography, µCT and SR-µCT, respectively) to describe the changes tesserae undergo during ontogeny in the round stingray *Urobatis halleri*. Using a standardized sectioning technique, we present sections of ontogenetic series of tesseral mats in order to define age- and location-specific tesseral characteristics, including aspects of size and shape, mineral accretion processes, mineral density distribution, and the interaction of tesserae and soft tissue. Further, we investigate variation in tesserae shape across adults of a variety of shark and ray species, to highlight common structural aspects of elasmobranch tessellated cartilage in general.
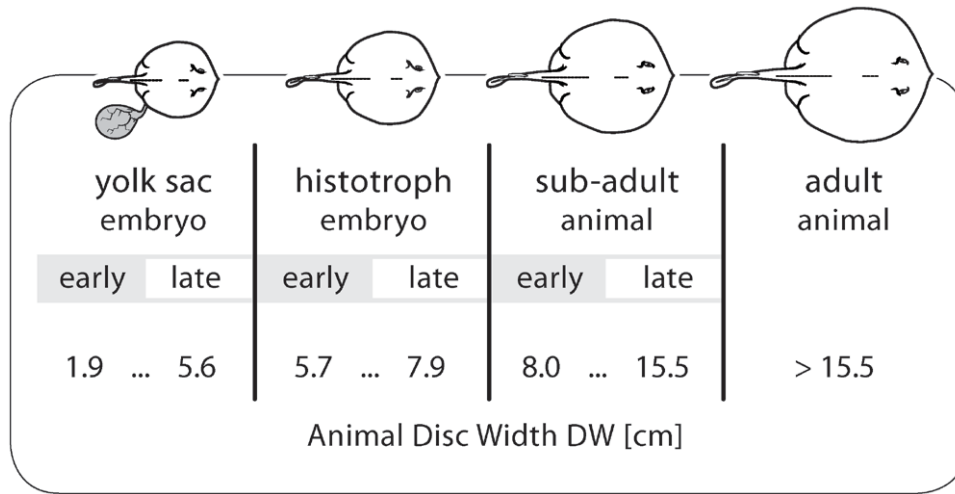
4.2   MATERIALS & METHODS

4.2.1   Specimens

The round stingray *U. halleri* was chosen for this study because of the availability of full onto-genetic series, and of published developmental and structural data (Dean et al. 2009, 2010; Omelon et al. 2014), but also because the size of *U. halleri* skeletal elements and tesserae is particularly suit-able for scanning in high-resolution laboratory and SR-µCT scanners. Note, throughout this article, we use the term 'skeletal element' to indicate a single, discrete piece of the elasmobranch skeleton, because an accepted term for elasmobranch skeletal elements is currently lacking in the literature. All specimens were donated from another study (Lyons et al. 2014), collected by beach seine from collec-tion sites in San Diego and Seal Beach, California, USA. The animals were shipped on dry ice and stored in a freezer at 20 °C until sample preparation. Speimens were re-thawed in warm water, before their skeletal elements (pectoral bar, propterygium and hyomandibula) were carefully removed and stored either in 75% ethanol at 4 °C or immediately processed for embedding (see below). We used these skeletal elements in our study because of their elongated and rodlike shape, facilitating sample preparation and providing large flat surfaces covered with tesserae. The first appearance of tesserae in *U. halleri* was previously reported for animals with a disc width (DW) of approximately 6.0 cm (Dean et al. 2009, 2010; Omelon et al. 2014). DW is a common size metric for batoid fishes and refers to the lateral dimension of the animal. Specimens for this study ranged from yolk sac embryos (1.9–5.6 cm DW), to histotroph embryos (lacking yolk sacs and feeding on intrauterine milk; 5.7– 7.9 cm DW), to sub-adults (8.0–15.5 cm DW), to adults (> 15.5 cm DW; Table 1); ontogenetic stage determination was according to Hale & Lowe (2008).

4.2.2   Micro-computed tomography

To examine the development of tesserae across whole skeletal elements, we performed µCT scans of hyomandibulae from animals at four ontogenetic stages: 7.0 cm DW (female); 11.0 cm DW (male); 14.4cm DW (female); 19.0cm DW (female). Note, in this study inter-sex comparisons are possible, because there are no appreciable differences in size between males and females of *U. halleri*, particularly for the sub-adult stages (Hale & Lowe, 2008). After dissection, the skeletal elements were dehydrated in an ascending alcohol series and stored until scanning in 75% ethanol. Samples were mounted in clay, sealed in ethanol-humidified plastic tubes and scanned with a Skyscan 1172 desktop µCT scanner (Bruker microCT, Kontich, Belgium). Scans for all samples were performed with voxel sizes of 4.89 µm, at 59 kV source voltage and 167 lA source current, over 360 ° sample rotation. Virtual cross-sections of skeletal elements in Fig. 2 are averages of 20 (cross-section) images (100 µm), gener-ated in ImageJ.

Table 1: Developmental stages of round stingray *Urobatis halleri*.

yolk sac embryo		histotroph embryo		sub-adult animal		adult animal
early	late	early	late	early	late	
1.9 … 5.6		5.7 … 7.9		8.0 … 15.5		> 15.5

Animal Disc Width DW [cm]

To examine interspecific, gross structural variation in tesserae, as well as the shape variation of intertesseral joints, we performed SR-µCT scans of mineralized tissue from the lower jaws of a variety of elasmobranch fishes, including nine batoid species (*Dasyatis sabina, Myliobatis californica, Narcine bancroftii, Pteroplatytrygon violacea, Raja eglanteria, Raja stellulata, Rhinoptera bonasus, Torpedo californica, U. halleri*) and four shark species (*Heterodontus franciscii, Notorynchus cepedianus, Somniosus pacificus, Squatina californica*). For each species, tissue samples, typically several centimeters square and ~ 1 cm thick, were excised from flat portions of the surfaces of the skeletal elements (mid-shafts of the lower jaws). The perichondrium was not removed before excision; samples were, therefore, expected to contain all components of tessellated cartilage: a layer of tesserae, sandwiched between perichondrium and uncalcified cartilage. All samples were freeze-dried for better stability in scanning, mounted with beeswax directly onto sample stubs, and scanned using high-resolution propagation phase-contrast X-ray micro-tomography at the beamline ID19 of the European Synchrotron Radiation Facility (ESRF, Grenoble, France). Samples were imaged with voxel sizes of 0.35–1.75 µm, using a multilayer monochromator, beam energy of 30 keV, propagation distance of 20–50 mm, 0.5–1.0 s exposures, in continuous mode and over 180 ° sample rotation. Anatomy and ultrastructure from all µCT scans were investigated in two-dimensional slices and three-dimensional volumetric reconstructions using ZIB-Amira software (Zuse Institute Berlin, Germany).

4.2.3 Scanning electron microscopy

To examine the development of tesserae on the ultrastructural level, we performed SEM in combination with a backscatter electron detector (backscatter SEM) of vertical and planar sections of tesserae (Fig. 1C) from animals at four ontogenetic stages: 6.0 cm DW (female); 7.5 cm DW (female); 8.5 cm DW (female); 20.0 cm DW (male); and 24 cm DW (female; Fig. 3). Pectoral bars were dissected

from *U. halleri*, bisected longitudinally and trimmed down to tessellated strips with little uncalcified cartilage backing. We air-dried and simultaneously flattened the tesseral layer between Teflon plates to prevent sticking. Dried samples were cut into smaller pieces and placed in a custom-built PMMA (plastic resin) holder, according to the desired orientation (vertical or planar). Samples were embedded in PMMA, cut in slices (300 ± 100 µm thick; Buehler IsoMet low speed saw) and mounted on a PMMA object slide using double-faced adhesive tape. Sections were polished with sandpaper plates with descending grain sizes (Logitech PM5 Precision Lapping and Polishing Machine), and finally using a soft polishing plate with diamond spray (0.25 µm grain size).

Backscatter SEM, via the detection of backscattered electrons, allows visualization of differences in either tissue elemental density (e.g. mineral density) or elemental composition as variation in gray-scale values. Images were acquired of polished samples in backscatter mode using a Field Emission-Environmental Scanning Electron Microscope (FE-ESEM, FEI Quanta 600F) in environmental mode (i.e. at low vacuum without sputtering) with an acceleration voltage of 10–12.5 kV. To determine the nature of the grayscale variation observed in backscatter SEM, we used a Tescan Vega-3 SEM equipped with a Bruker X-Flash 5030 energy-dispersive spectrometer (EDS). All EDS spectra and elemental maps were acquired at 20kV acceleration voltage at 15mm working distance, and paired with images of the same regions of interest taken under the same conditions in backscatter mode.

4.2.4 Polarized light microscopy

To examine the orientation of collagen in and between tesserae, we performed PLM on planar sections of tesserae from *U. halleri* (13 cm DW, section thickness about 250 µm). The collagen fibers showed maximum birefringence at ± 45 ° relative to the position of the polarizer and analyzer. A lambda filter (or first-order retardation plate) was used in the optical path of the microscope, to convert variations in the monochromatic birefringent signal to color, to further distinguish among different orientations of collagen fibers in the sample.

4.2.5 Light microscopy

Samples of the anterior shoulder girdle (propterygium) were collected from an adult male *U. halleri* (20.0 cm DW), immediately fixed with 4% paraformaldehyde (PFA) in phosphate-buffered saline (PBS; 0.1 M), stored for 6 h in this solution at room temperature, then rinsed in PBS. Samples were stored in PBS (0.1 M, 0.05% sodium azide) before being processed for microscopy. The propterygium was examined because its shape offers comparatively large regions of flat skeletal surface, where tesserae are relatively uniform in their cross-sectional shapes.

Samples were decalcified with ethylenediaminetetraacetic acid (EDTA) for 1 week, dehydrated in graded isopropanol and xylene series, and embedded in paraffin using a routine histological infil-

tration processor (Miles Scientific, Naperville, IL, USA). Serial cross-sections (7 µm) were made on a HM 355S microtome (Microm, Walldorf, Germany), and three sections per slide mounted on SuperFrost"Plus slides. Sections were stained with haematoxylin and eosin (H&E; Shandon Varistain 24-4, Histocom Vienna, Austria).

4.2.6 Transmission electron microscopy

Specimens were immediately fixed in 4% PFA buffered in PBS after collection, post-fixed in 1% osmium tetroxide in distilled water for 24 h at 4 °C, then rinsed, and decalcified as described before, dehydrated in graded ethanol series and embedded in EPON resin. Ultrathin cross-sections (90 nm) were cut on the same microtome (see above) with an ultra-diamond knife, mounted on dioxan-formvar coated slot-grids (#G2500C, Christine Gro€pl, Elektronenmikroskopie, Tulln, Austria), and stained with uranyl acetate and lead citrate (Leica Ultrostainer, Leica Microsystem, Wetzlar, Germany). The ultrathin sections were examined with a Philips CM 120 TEM at 80 kV (FEI, Eindhoven, the Netherlands) equipped with a MORADA digital camera (Olympus SIS, Mu€nster, Germany) using Olympus TEM Imaging Platform software.

4.3 RESULTS

4.3.1 Tessellated cartilage development

Tesserae exhibited shape and size changes during development that were visible in both µCT (Fig. 2) and backscatter SEM (Fig. 3). In µCT, tesserae could be seen to be irregularly shaped in histotrophic embryos and young sub-adult animals (Fig. 2), but more regularly geometric in older subadults and adults (Fig. 2). In histotrophic animals especially, it was often difficult to detect the boundaries of individual tesserae as they typically had low densities (X-ray attenuation) at their margins (Fig. 2). Tesserae did not develop uniformly across the skeleton in terms of their size and degree of mineralization, but rather varied considerably across different regions of the same skeletal element. In µCTs of hyomandibulae of four developmental stages of *U. halleri* (Fig. 2), individual tesserae were first discernible at the ventral and chondocranial edges of hyomandibulae (Fig. 2A, asterisk and circle, respectively), whereas the rest of the skeletal element appeared largely unmineralized. This was verified by virtual/digital cross-sections through hyomandibulae, which also showed that in older animals tesserae are considerably thicker in curved regions compared with planar regions (Fig. 2, third row of images).

Backscatter SEM supported the previously mentioned observation of the increase of tesseral size with age, but also showed age-related decreases in the distance between tesserae and the peri-
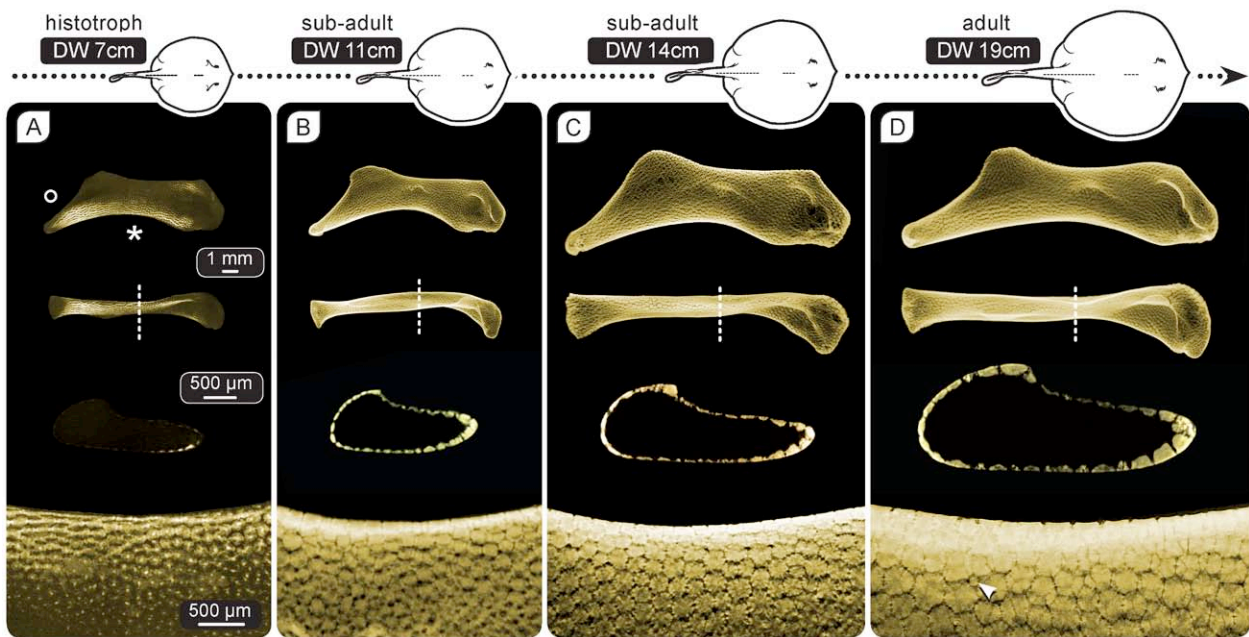
Fig. 2 Armoring the endoskeleton – the development of calcified, tessellated cartilage.
Micro-computed tomography (lCT) imaging of the left hyomandibula of four different developmental stages (indicated at the top of each column) of the round stingray *Urobatis halleri*. The top and second rows show lateral and ventral views, respectively, of the whole skeletal element. In lCT, the earliest tesserae were observed in animals with a disc width (DW) of ~ 7 cm (histotroph animals; A), with the degree of mineralization increasing with age. Tesserae do not form simultaneously over the entire skeletal element, rather appearing first in ventral and chondocranial portions (asterisk and circle, respectively). Cross-sections of the skeletal element (third row, section position indicated by the white lines in the second row) show an increase in number, width and depth of tesserae with age. Note the tesseral layer appears to be thicker in stark convex areas (averaged images over 100 μm = 20 images). Small tesserae amidst big tesserae suggest the development of new tesserae among existing ones (arrowhead, D bottom row). Scale bars in (A) apply also to (B–D).

chondrium, in the distance between adjacent tesserae, and in the homogeneity of cell distribution and mineral density in tesserae (Fig. 3). In the youngest animals investigated (yolk sac embryos, ≤ 5.6 cm DW), there was no evidence of mineralization (data not shown). There was very little mineralized tissue in embryos at the early histotrophic stage: skeletal elements are mostly a core of unmineralized cartilage, with relatively uniform chondrocyte density, wrapped in an outer perichondrium (Fig. 3A,B). Tesserae at this ontogenetic stage are poorly formed, appearing as small patches of mineralized tissue (~ 75– 100 μm wide and ~ 30–50 μm deep), ~ 10–30 μm below the perichondrium, and separated from one another by ~ 50 μm gaps (Fig. 3B). The mineralized tissue is globular in appearance, forming thin and often incomplete dividers between adjacent chondrocytes. At a higher magnification, the tissue appears to be formed from conglomerations of small spherical mineralized globules(~ 1–3 μm). These are visible in particular at the margins of tesserae (Fig. 3B).

The typically described adult tesseral morphology (i.e. geometric blocks of mineralized tissue; for instance, see Bargmann, 1939; Kemp & Westrin, 1979) first appeared in our investigated specimens at the young sub-adult stage (Fig. 3C,D). With age, tesserae increased in width (~ 75–350 μm) and depth (~ 30–250 μm; Fig. 3E–H), as shown also in our μCT data (Fig. 2); note, however, that these measurements are from two-dimensional backscatter SEM slices (i.e. they may not capture the maximum dimensions of a tessera) and that tesserae varied considerably in size, even within a single skeletal element (e.g. see arrowhead in Fig. 2D).

As the size and shape of tesserae continued to change with age, the morphology of their contact zones changed as well. In late histotrophic animals, tesserae were generally in close contact (i.e. in contrast to the case in younger animals, Fig. 3B): tesserae had irregular margins (in both vertical and planar sections) that were in contact with adjacent tesserae for their entire length (i.e. with no visible intertesseral gap in planar sections; Fig. 3D). In older sub-adult animals, tesseral margins became more
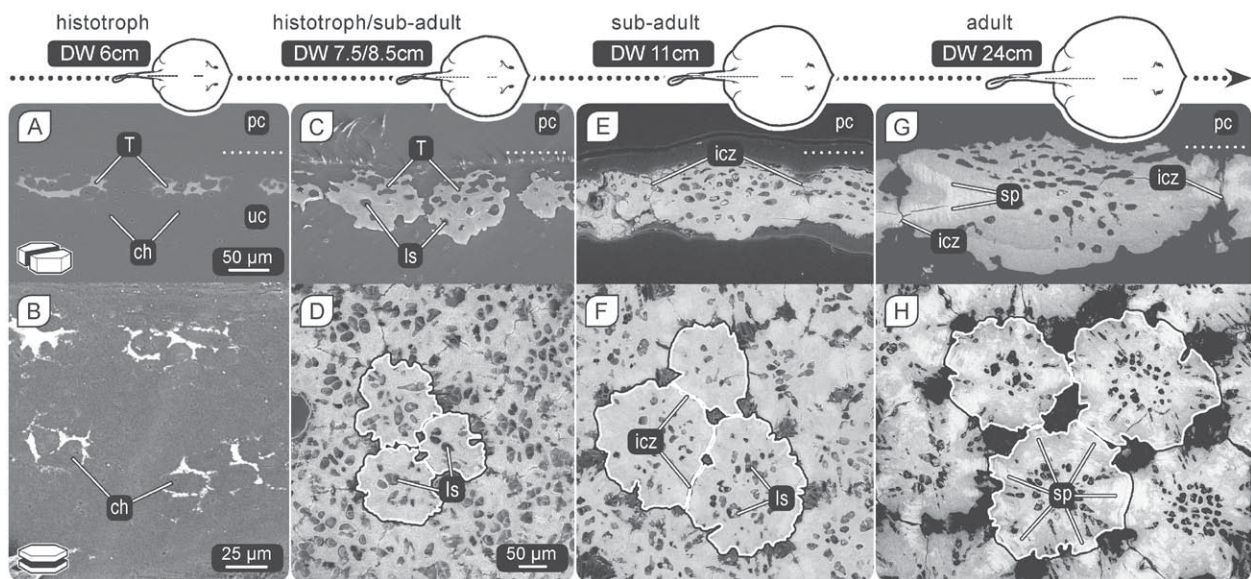

Fig. 3 Tiling a growing surface – development of tesserae.
Vertical sections (upper row) and planar sections (lower row) of tesserae from an age series of *Urobatis halleri*. All images are from backscatter scanning electron microscopy (SEM) and therefore show mineralized tissue and variations in mineral density. (A, B) The first, poorly formed tesserae (T) were visible, in animals with ~ 6 cm disc width (DW), as thin strips of globular mineralized tissue between chondrocytes (ch), in the uncalcified cartilage core (uc) some distance from the perichondrium (pc). As animals grow (moving from left to right in the figure), tesserae approach the perichondrium, growing larger and closer together, and tiling becomes more regular, especially after tesserae come into contact. (C, D) As tesserae grow, chondrocytes are entombed in the mineral phase, enclosed in lacunar spaces (ls). (E, F) Once tesserae come into contact, areas of higher mineral density (spokes, sp) develop at the margin of the tesserae, associated with the intertesseral contact zone (icz) of abutting tesserae. Spokes elongate as tesserae grow. Note in (E) and (G) that lacunar spaces at the perichondral side of tesserae are flatter and oriented parallel to the perichondrium, compared with the round lacunar spaces in the chondral portion of tesserae. Scale bar in (A) applies also to (C, E, G); scale bar in (D) applies also to (F, H).
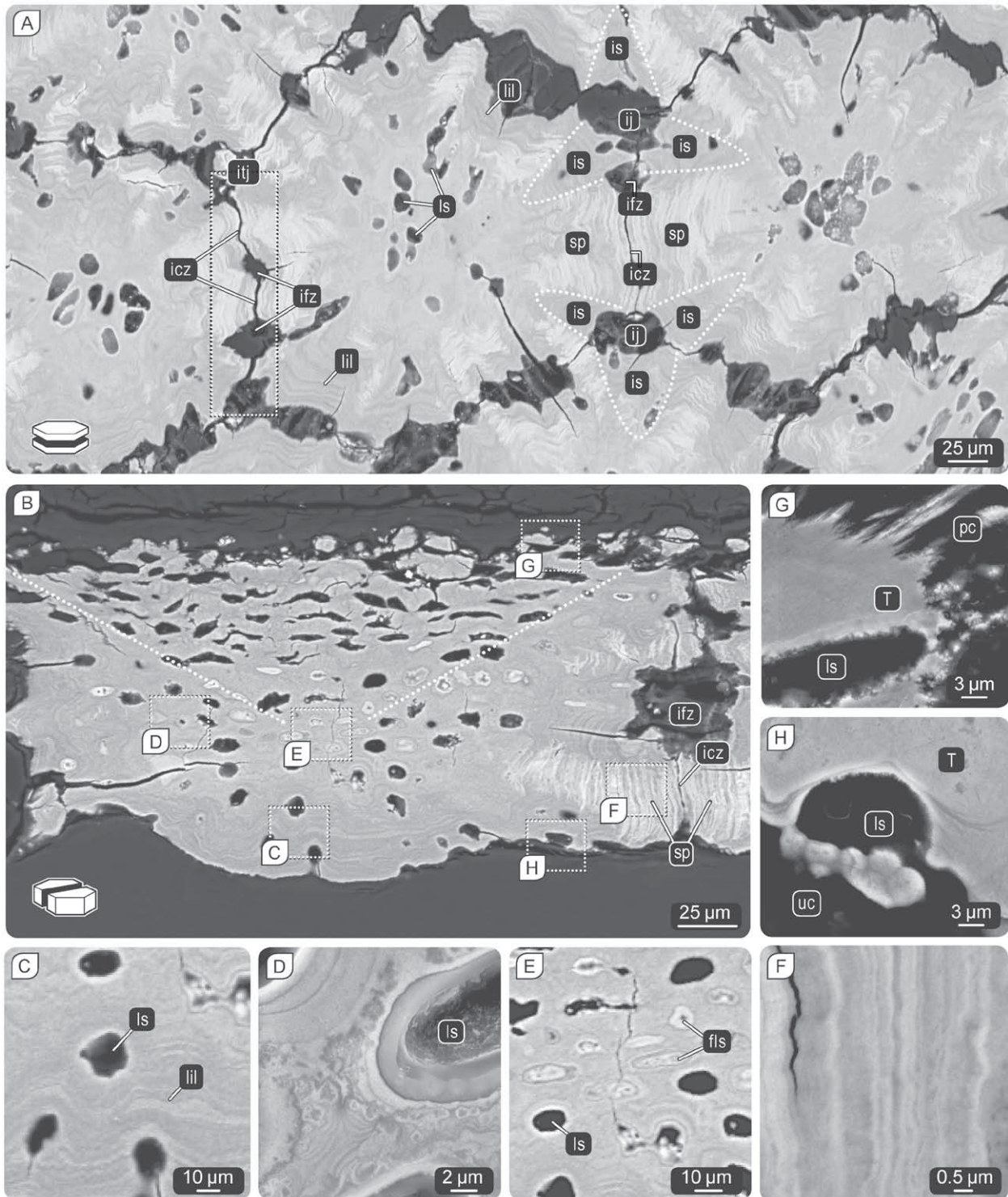
Fig. 4 Heterogenic ultrastructure – mineral density variation in tesserae [backscatter scanning electron microscopy (SEM)].

(A, B) Planar (A) and vertical (B) sections of tesserae of *Urobatis halleri* reveal several distinct types of mineral density variation in tesserae suggesting a variety of mineralization processes. Spokes (sp) are the most prominent features of sub-adult and adult tesserae. They are acellular, hyper-mineralized, laminated wedges, radiating from intertesseral contact zones (icz), but not the uncalcified fibrous zones (ifz) of intertesseral joints (itj). In (A), interspoke regions (is) (flanking spokes) are coincident with fibrous zones, contain lacunar spaces (ls) and exhibit Liesegang lines (lil). The intertesseral junction (ij), the region between three (or more) tesserae, is comprised of unmineralized cartilage ▲

containing cells and few fiber bundles. In (B), the white dashed line indicates the two portions of tesserae, with the cap zone on top and the body zone below (perichondral and chondral side, respectively). (C) Liesegang lines are bands of different mineral density following the contours of tesseral margins, and were found mostly in the chondral portion of tesserae and edges bordering intertesseral fibrous zones (ifz) between abutting tesserae. (D) Filigreed pattern in the center of tesserae, could also be found between Liesegang lines. (E) Lacunar spaces (ls), housing cells, could be found throughout tesserae, except in regions with spokes (sp). Note the variation in shape and distribution of lacunar spaces in the tessera in (B). Lacunae located towards the perichondral edge were considerably flatter and together formed an inverted pyramid shape. Filled lacunar spaces (fls) were found in the middle of older tesserae [animals > 11 cm disc width (DW)] and showed a higher mineralization compared with the rest of the tessera body. (F) Magnification of a spoke showing the oscillating mineral density of spoke laminae. (G) Rough mineralization front on the perichondral side and (H) globular mineralization front on the chondral side of tesserae.

planar, resulting in smoother intertesseral contact zones (ICZ) of adjacent tesserae and an overall more regular, polygonal tiling pattern (Fig. 3F). This sub-adult change in tesseral morphology was also coincident with the development of hypermineralized tesseral 'spokes' described below.

Tesserae in the early histotrophic stage showed uniform density of lacunae, the holes in tesserae that contain living cells (Fig. 3C,D). With increasing tesseral age, lacunar density became visibly patchier. The shape and distribution of lacunar spaces varied with location in the tessera; notably, lacunae were absent from high mineral density regions associated with ICZ (see below; Figs. 3G,H and 4A,B). Lacunae located towards the perichondral edge were considerably flatter, compressed in the perichondral–chondral direction (Figs 3G and 4B). Altogether, when observed in vertical sections, the flat, perichondrally associated lacunae formed an inverted pyramid shape in the upper portion of tesserae (the 'cap' zone of Kemp & Westrin, 1979), with all other cell lacunae being rounder (located in the lower, 'body' zone portion of tesserae; Fig. 4B). The lenticular lacunar morphology appeared approximately in the sub-adult stage, at the time when the gap between tesserae and perichondrium closed, bringing tesserae in contact with the fibrous perichondrium (Fig. 3C,E,G).

4.3.2 Tesseral spokes and other features of mineral density variation

A pronounced change in tesseral mineral density (visualized in backscatter SEM imaging) was observed during tesseral development. This began approximately in the late histotrophic stage when tesserae first came into contact with one another and planar contact surfaces began to form, resulting in tesserae appearing to have more linear margins and overall geometric shapes (Fig. 3D,F,H). At this point, at the margins of tesserae, exclusively in the regions bordering the planar intertesseral contact surfaces, laminae of higher mineral density tissue began to form (Fig. 4A). From this stage onward, as tesserae grew wider by accretion of new mineral, new highly mineralized laminae were added at their edges, at the ICZ. At any given intertesseral joint, the most recently deposited lamina (i.e. at the tesseral

edge) was the same length as the ICZ. As a result, as tesserae and their associated contact zones grew larger with age, the swaths of high mineral density increased in length (via addition of new laminae distally, at the tesseral edge) and became more wedge shaped (by each successive added lamina being wider than the previous). The length of each lamina (i.e. the width of the spoke) varied from ~ 10 μm close to the center of tesserae to ~ 50 μm at the edges of adult tesserae.

The high mineral density regions appeared in planar view like spokes on a wheel (Figs 3H and 4A). In vertical views, the shape of these 'spokes' was more variable, and was dependant on the nature of the points of contact of adjacent tesserae: tesserae were typically not in contact over the entire peri-chondral–chondral distance of the joint, rather there could be multiple points of contact with spokes radiating from each (Figs 3G and 4B). From EDS data (not shown), we verified that these contrast differences (and all other features involving backscatter SEM contrast variation, see below), were due to local differences in the extent of mineralization, rather than variation in elemental composition (e.g. the introduction of high atomic number elements that could also account for backscatter SEM contrast variation). This is further supported by the observation from EDS data that oscillations in backscatter SEM contrast could be matched to local oscillation in calcium and phosphorus content.
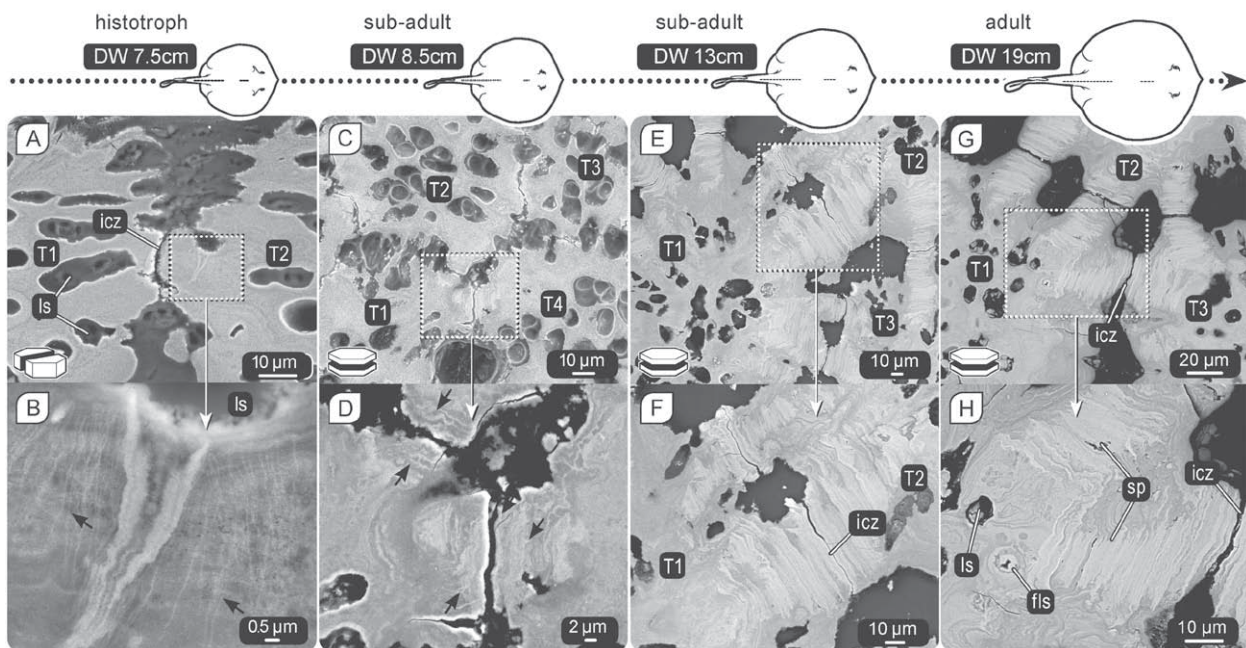
Fig. 5 Ultrastructural reinforcement linked to growth mechanisms – development of spokes in *Urobatis halleri*. (A, B) Spokes (sp) first appeared in animals of ~ 7.5 cm disc width (DW), coincident with intertesseral contact zones (icz) and approximately when adjacent tesserae (T) first came into contact. Faint 'wispy' lines more or less parallel to the tesseral margin were often visible near the tesseral edges in the periods before spokes formed. (C–F) As animals age, tesserae grow and intertesseral contact zones (icz) widen, spokes lengthen and widen at their distal ends, their distinct laminar structure of oscillating mineral density becoming more obvious. Spokes converge toward the center of tesserae; in some tesserae, adjacent spokes merge proximally (e.g. G, H), suggesting early contact of tesserae at this region in the beginning of spokes development. Filled lacunar spaces (fls), lacunar spaces (ls).

Fig. 6 Spoke laminae and the underlying soft tissue – spoke ultrastructure in adult specimens of *Urobatis halleri*.

(A, B) Spoke (sp) laminae in adjacent tesserae mirror each other's shape (arrowheads) and suggest the shape of younger tesseral margins [backscatter scanning electron microscopy (SEM) images]. (C, D) Though the resolution is lower, micro-computed tomography (lCT) is capable of visualizing spokes and spoke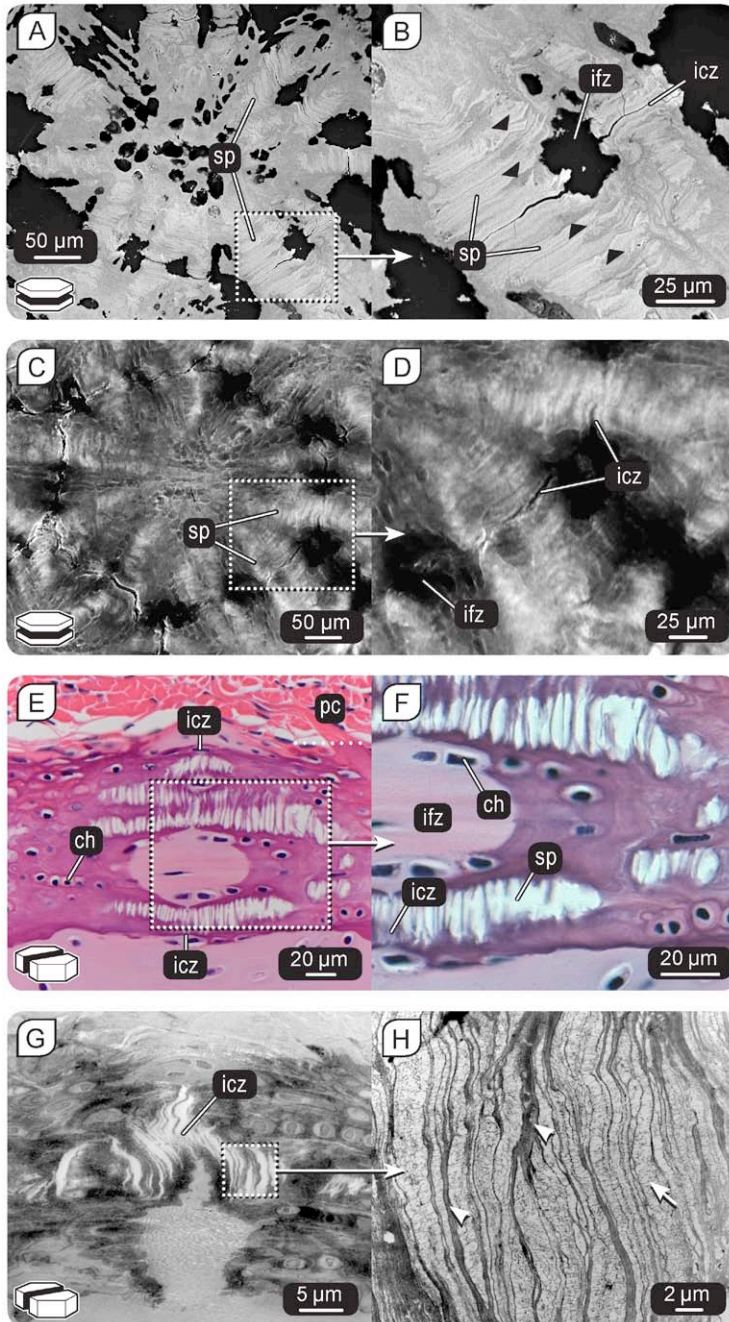 laminae. (E, F) Histological staining [haematoxylin and eosin (H&E)] and (G, H) transmission electron microscopy (TEM) of decalcified, vertical thin sections, showing the organic tissue underlying spokes, which also exhibits a laminar pattern. H&E and TEM sections show bands of thick organic tissue (arrow heads) alternating with gaps/light areas of low organic content (arrow), presumably correlating with areas of lower and higher mineral density spoke laminae in backscatter SEM, respectively.

Adult spokes were characterized by laminae (~ 100 nm–2 µm thick) of varying mineral density, arranged in series parallel to the plane of the ICZ (Figs 4A,B,F, 5E–H and 6A–D). Brighter (higher mineral density) laminae typically bordered darker (lower mineral density) laminae, resulting in spokes having an appearance of oscillating mineral density at higher magnifications (Fig. 4F). Evidence of spokes first appear in the histotrophic stage in the form of periodic, 'wispy' lines (~ 100 nm) of higher mineral density, arrayed parallel to ICZ (Fig. 5A,B).

In the regions of tesserae lacking spokes, mineral density was generally lower, and we observed additional forms of mineral density variation. For example, Liesegang lines, concentric lines following the contours of adjacent tesseral structural features (e.g. tesseral margins, lacunar spaces), were often observed and were similar in morphology to those described by previous authors for other species (e.g. Weidenreich, 1930; Bargmann, 1939; Ørvig, 1951; Kemp & Westrin, 1979). In our samples, Liesegang lines were found particularly near the chondral edge of tesserae and could in some cases be very long, following nearly the entire contour of a tessera's chondral margin (Fig. 4B). Backscatter SEM revealed that Liesegang lines were bands of variable mineral density, appearing as light (higher mineral density) and dark (lower mineral density) bands following each other in succession (Fig. 4C). In more central areas of tesserae, the mineral density variation often appeared with an even finer degree of detail, forming a series of thin, filigreed patterns (Fig. 4D). Neither Liesegang lines nor the filigreed mineral density variation were visible in the perichondral portion of tesserae, which instead had a similar fibrous appearance to the overlying perichondrium but was mineralized (Figs 4B and 8F). 'Normal' lacunar spaces (housing living cells) were found in all tesseral regions, except those with spokes; however, lacunar spaces located in the middle of adult tesserae (i.e. equidistant between chondral and perichondral portions) were occasionally filled, to varying degrees, with mineralized tissue (Fig. 4B). Filled lacunae and spokes represented the features of highest mineral density in adult tesserae (Fig. 4E).

The pronounced laminar morphology seen in the spokes of adult tesserae first appeared in young sub-adults, where spokes were short and consisted of few laminae (Fig. 5C,D). The length of spokes (i.e. the number of laminae) increased with age (Fig. 5C–H). Spoke laminae close to the contact zone mirrored the shape of the tesseral margin (Fig. 6A,B). The morphology of laminae in spokes tended to change with distance from the contact zone and in a similar way in opposing tesserae: the specific appearance (e.g. contour and mineral density) of a given lamina at a particular distance from the contact zone was similar to that of a lamina the same distance away in the opposing tessera (Fig. 6B, arrowheads). The organic matrix underlying spokes, visible in demineralized paraffin histology (6 μm) and ultrathin TEM sections (90 nm), also exhibits a laminar pattern, consisting of parallel bands of thicker fibrous tissue (~ 0.5–2.0 μm wide; Fig. 6E–H, arrowheads in H) separated by gaps filled with looser, less organized fibrous material (Fig. 6H, arrow).

4.3.3 Intertesseral joints

In early histotrophic animals, the gap between tesserae is large and filled with unmineralized tissue (containing cells and fiber bundles; Fig. 3A,B). Tesserae come into contact in the mid-histotrophic stage, which results in the formation of what we define as the intertesseral joint, comprised of regions of intimate abutment of the two opposing edges of adjacent tesserae (ICZ) and small gaps
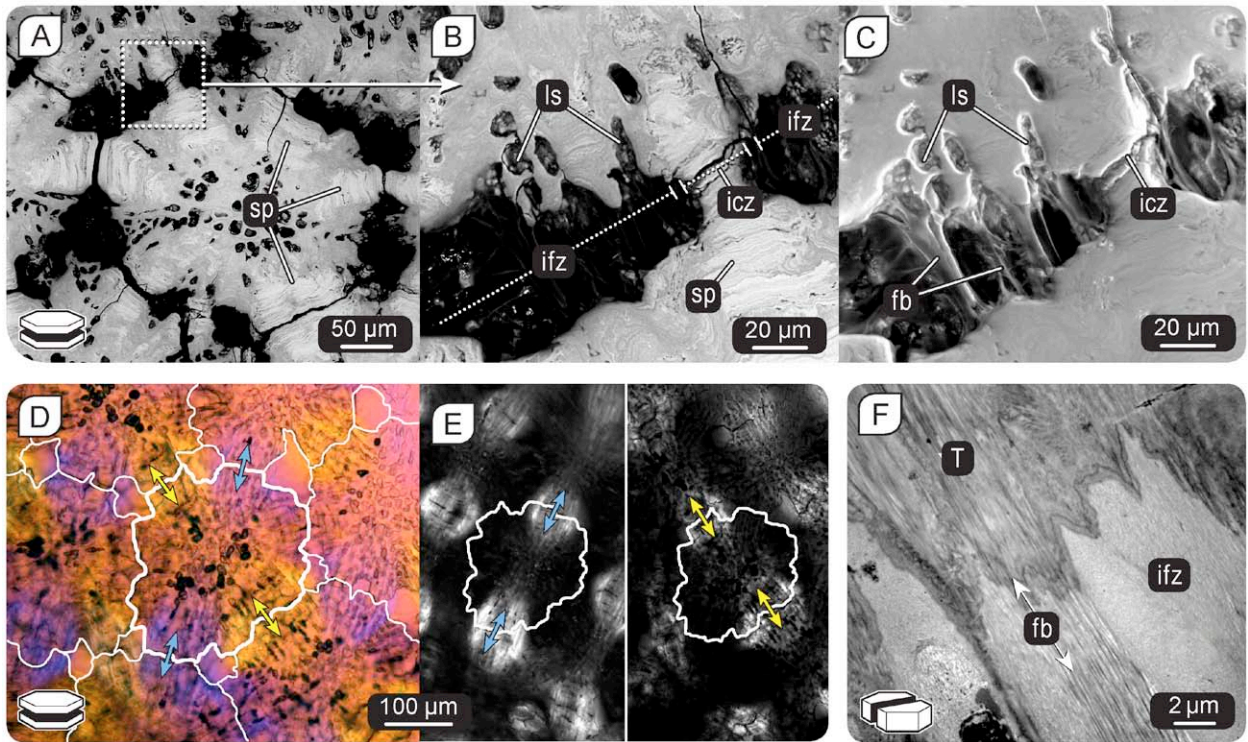
Fig. 7 Flexible linkage of tesserae – collagen fibers at the intertesseral joints.
(A–B) Backscatter scanning electron microscopy (SEM) of a planar section of tesserae (*Urobatis halleri*), with a focus on the intertesseral joint and the contact zone of two abutting tesserae. A comparison of backscatter SEM (B) and environmental SEM (C) images of the same joint area illustrates the complexity of intertesseral joints (itj), including intertesseral contact zones (icz) with spokes (sp) and unmineralized intertesseral fibrous zones (ifz) containing cells and fiber bundles (fb). Strings of cells were sometimes seen continuing between the ifz and adjacent tesserae (in lacunar spaces; ls); (D, E) Intertesseral collagen fibers are arrayed perpendicular to the plane of contact zones, as shown by polarized light microscopy (PLM) of adjacent tesserae in planar view visualizing the common orientation of joint collagen fibers bundles on opposite sides of tesserae (blue and yellow arrows), with (D) and without (E) the lambda filter. (F) TEM of a joint region of a vertical section, showing that fiber bundles pass uninterrupted from tesserae (T) into the unmineralized fibrous zone of the intertesseral joint.

containing cells and fiber bundles (intertesseral fibrous zones, IFZs; e.g. Figs 7B,C, 8D and 9). There is very little space between ICZ in *U. halleri* (< 2 μm); however, we observed no complex or large inter-digitations at these interactions (Figs 9 and 10A). As tesserae increased in size with age, the dimensions (i.e. the width and depth) of intertesseral joint regions also increased.

In the fibrous zones of intertesseral joints (i.e. where adjacent tesserae are not in direct contact), unmineralized fiber bundles span the distance between tesserae (Figs 6A,E,F and 7A–C). These fibers bundles were aligned in dense, parallel arrays, linking non-spoked regions of adjacent tesserae. Strings of several cells in end-to-end series were typically visible between intertesseral fibers (Fig. 6E,F), visible continuing into adjacent tesserae as strings of lacunae oriented toward the tesseral center (Fig. 7B,C). Under polarized light, planar sections of tesserae show patches of coloration associated with inter-
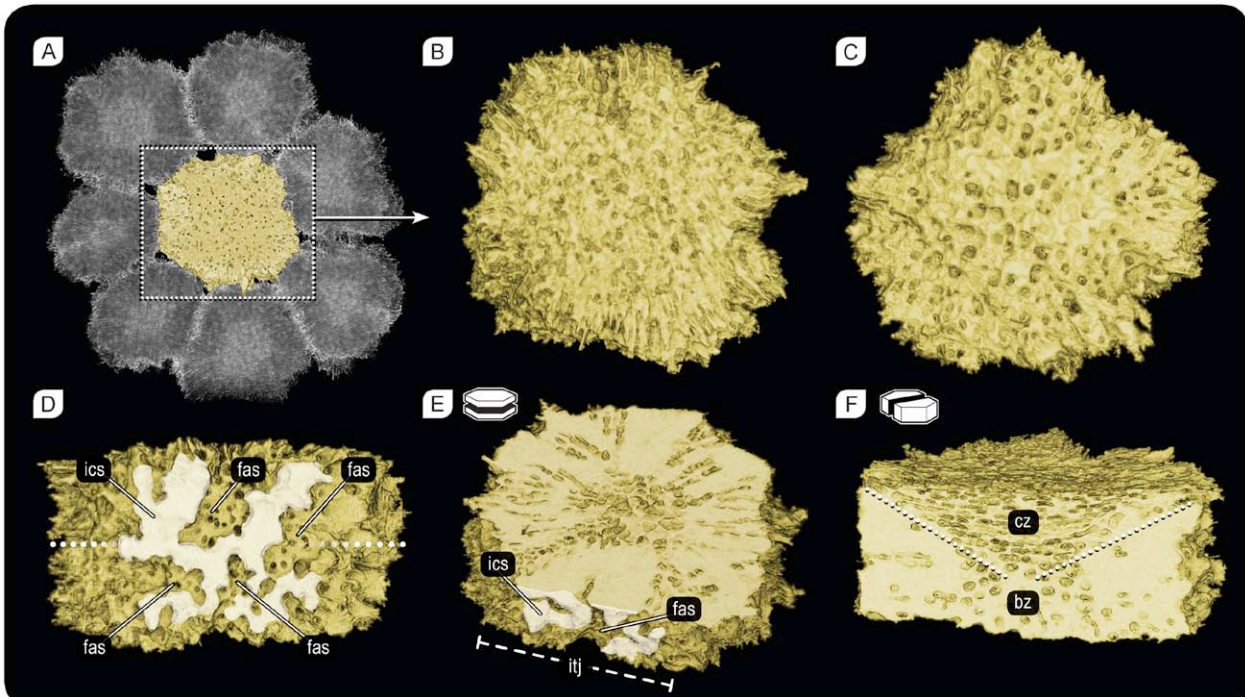
Fig. 8 Micro-computed tomography (lCT) imaging of *Urobatis halleri* tesserae.
(A) Adjacent tesserae in planar view. (B) Rough perichondral surface of a tesserae and (C) smoother chondral surface of a tesserae. (D) Lateral view of the joint face of a tessera from the abutting tessera's perspective, showing the complex arrangement of ICZ surface (ics, brighter area) surrounded by fibre attachment surfaces (fas) where fibers tether the two tesserae together. (E) Planar section through the middle of a tessera [from the sectioning plane shown with a dashed line in (D)] showing acellular regions in the periphery corresponding to spokes and the inter-tesseral contact surface (ics), and the rough fibre attachment surface (fas). (F) Vertical section through the center of a tessera showing a dashed line separating the cap zone (cz, perichondral portion, exhibiting an inverted cell pyramid with its base on the perichondral side) from the body zone (bz, chondral portion), containing cells in the center and acellular regions in the periphery, which correspond to spokes and ICZ.

tesseral joints (indicating areas of aligned birefringent material). Intertesseral joints on opposite sides of the same tessera exhibited similar coloration (e.g. blue arrows in Fig. 7D, indicating similar alignment), and joints at acute angles to each other exhibited different coloration (e.g. blue vs. yellow arrows in Fig. 7D,E). The birefringence indicates that the alignment of fibrous material in intertesseral joints is perpendicular to contact zones of adjacent tesserae, with fibers extending into both tesserae that share a joint. TEM images of demineralized intertesseral joint regions show joint fiber bundles extending uninterrupted from the joint space into tesserae (Fig. 7F).

In two-dimensional sections of joints (either vertical or planar), the proportions of IFZ and ICZ depend on the location of the cutting plane (Figs 7B,C and 9). This is due to the spatially complex, three-dimensional interactions of fibrous and contact zone regions (Fig. 8). In vertical views of tesserae (i.e. from the perspective of a neighboring tessera), the two regions of the joint are distinguishable by their appearance: where tesserae are in contact (ICZ) the tesseral sides exhibit a smoother surface texture (intertesseral
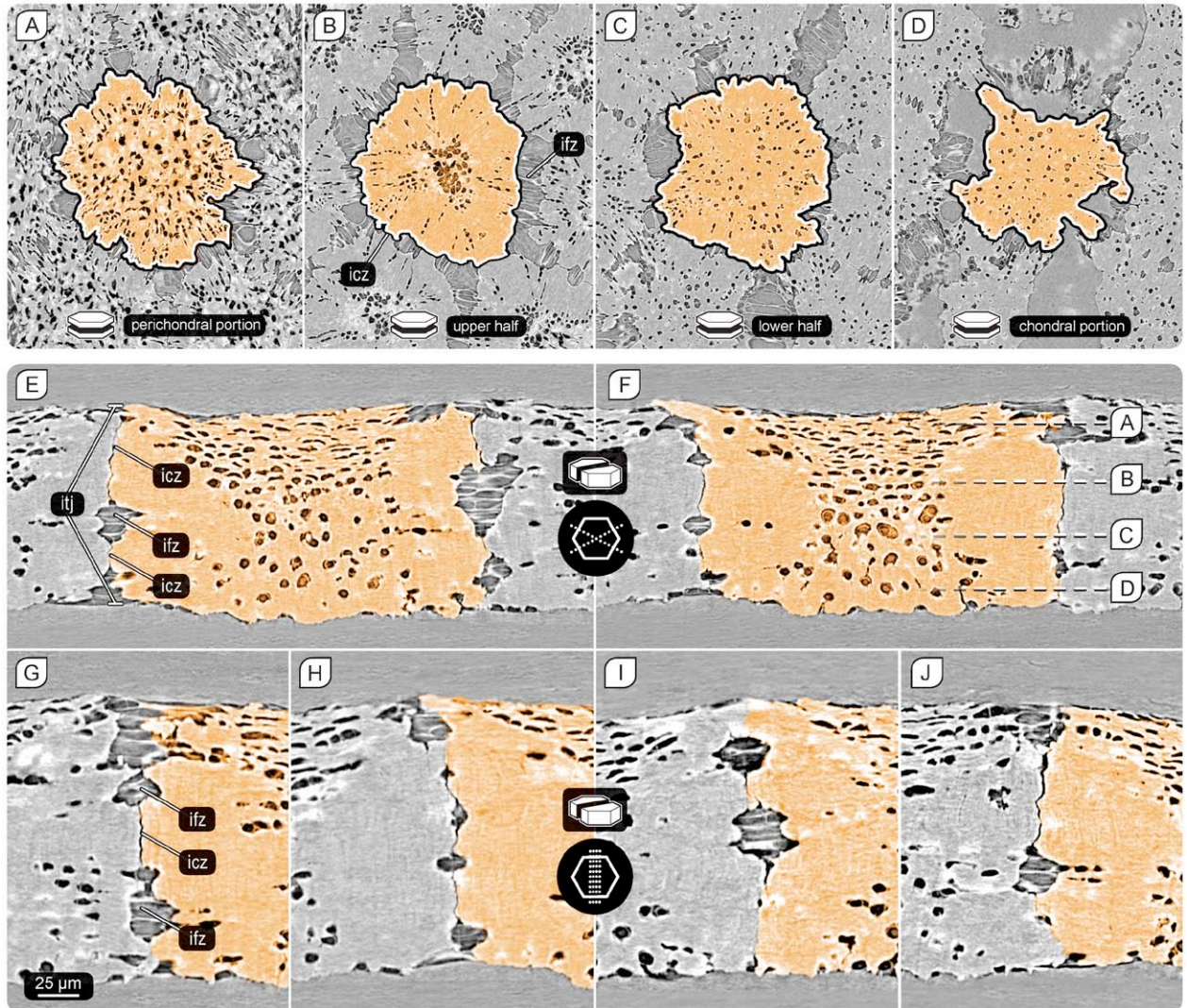
Fig. 9 Intertesseral joint morphology of *Urobatis halleri*.

Intertesseral joint morphology varies considerably with the sectioning plane through a tessera. The same tessera, sectioned in different orientations and planes, is shown in all images in the figure, highlighted in yellow; inset icons indicate section orientation and location. (A–D) Planar virtual sections through synchrotron radiation-based micro-computed tomography (SR-lCT) scans of adjacent tesserae at different depths. (E, F) Morphological comparison of opposing intertesseral joints of a tessera. (G–J) Comparison of serial vertical sections through an intertesseral joint of abutting tesserae. Where tesserae are in contact, the contact zones (icz) are rather flat, showing no interdigitations. Abutting tesserae, however, are never in contact over their entire lateral edges; instead cells and intertesseral collagen fibers are maintained in fibrous zones (ifz) adjacent to contact zones. For clarity, in all images, surrounding material (e.g. perichondral and chondral tissue) has been replaced with gray background post-scan.

contact surface), whereas the surrounding IFZ exhibit rougher walls, pock-marked with cellular lacunae (fiber attachment surface, Fig. 8D). The fibrous zones are typically slightly recessed and concave with respect to the contact surfaces (Fig. 9). The arrangement of the zones is mirrored in the adjoining tessera, such that the smooth contact surfaces of adjacent tesserae are touching and forming a bearing surface, whereas the opposing concave fibrous zones form a cavity filled with fibers spanning the joint space (Fig. 9E–J). Virtual
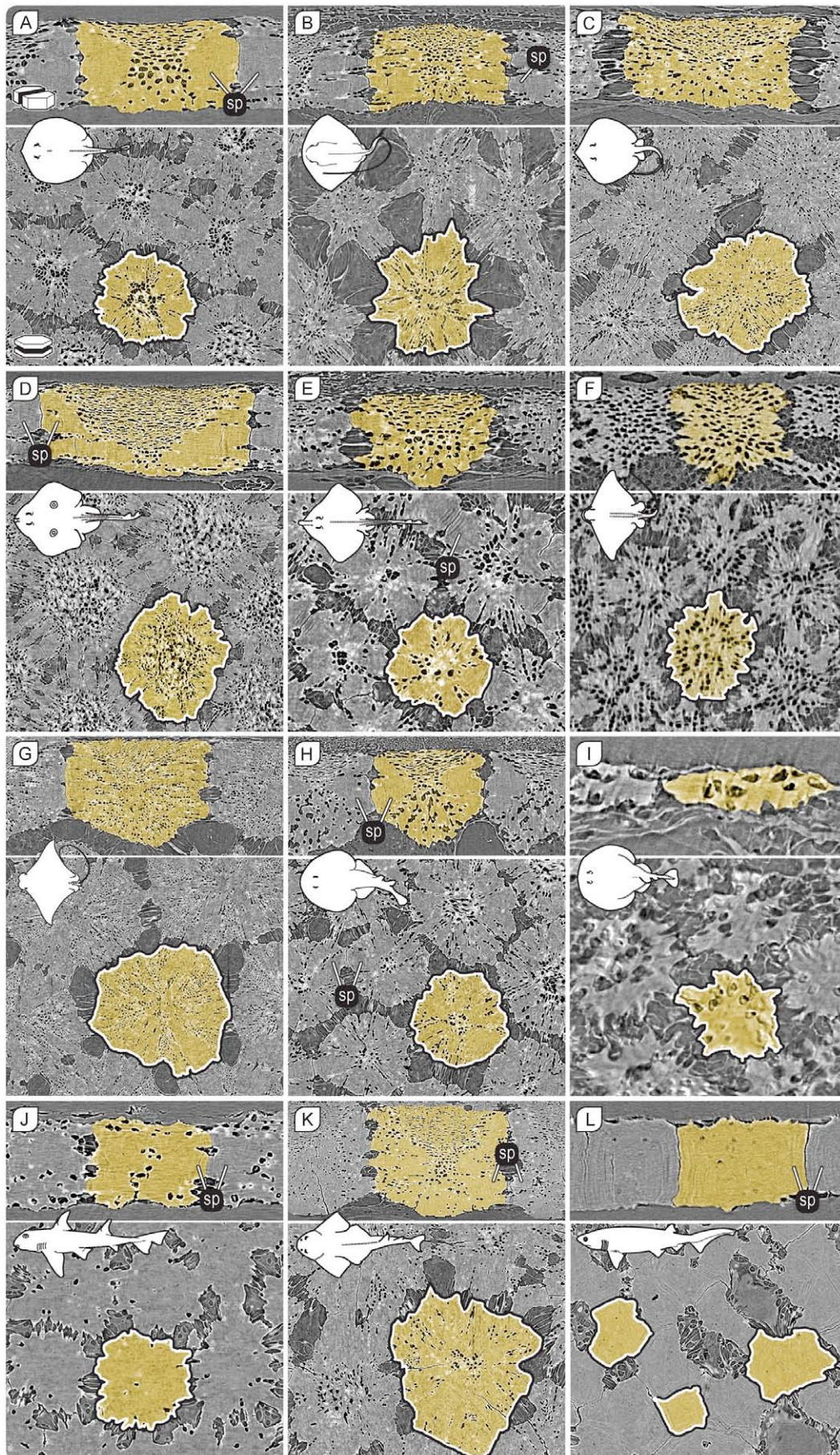
◀ **Fig. 10 Tesserae shape variation across different shark and ray species.**

Virtual sections of synchrotron radiation-based micro-computed tomography (SR-lCT) scans through the centers of adjacent tesserae in vertical (upper) and planar view (lower row). Despite a great variability in tesseral morphology, we observed commonalities in the morphology of the intertesseral joints, the arrangement and size of lacunar spaces, and the presence of spokes (sp). Lacunar spaces (black dots inside tesserae) are ~ 5–10 µm wide in all images. (A) *Urobatis halleri*, (B) *Pteroplatytrygon violacea*, (C) *Dasyatis sabina*, (D) *Raja stellulata*, (E) *Raja eglanteria*, (F) *Myliobatis californica*, (G) *Rhinoptera bonasus*, (H) *Narcine bancroftii*, (I) *Torpedo californica*, (J) *Heterodontus franciscii*, (K) *Squatina californica*, (L) *Notorynchus cepedianus*.
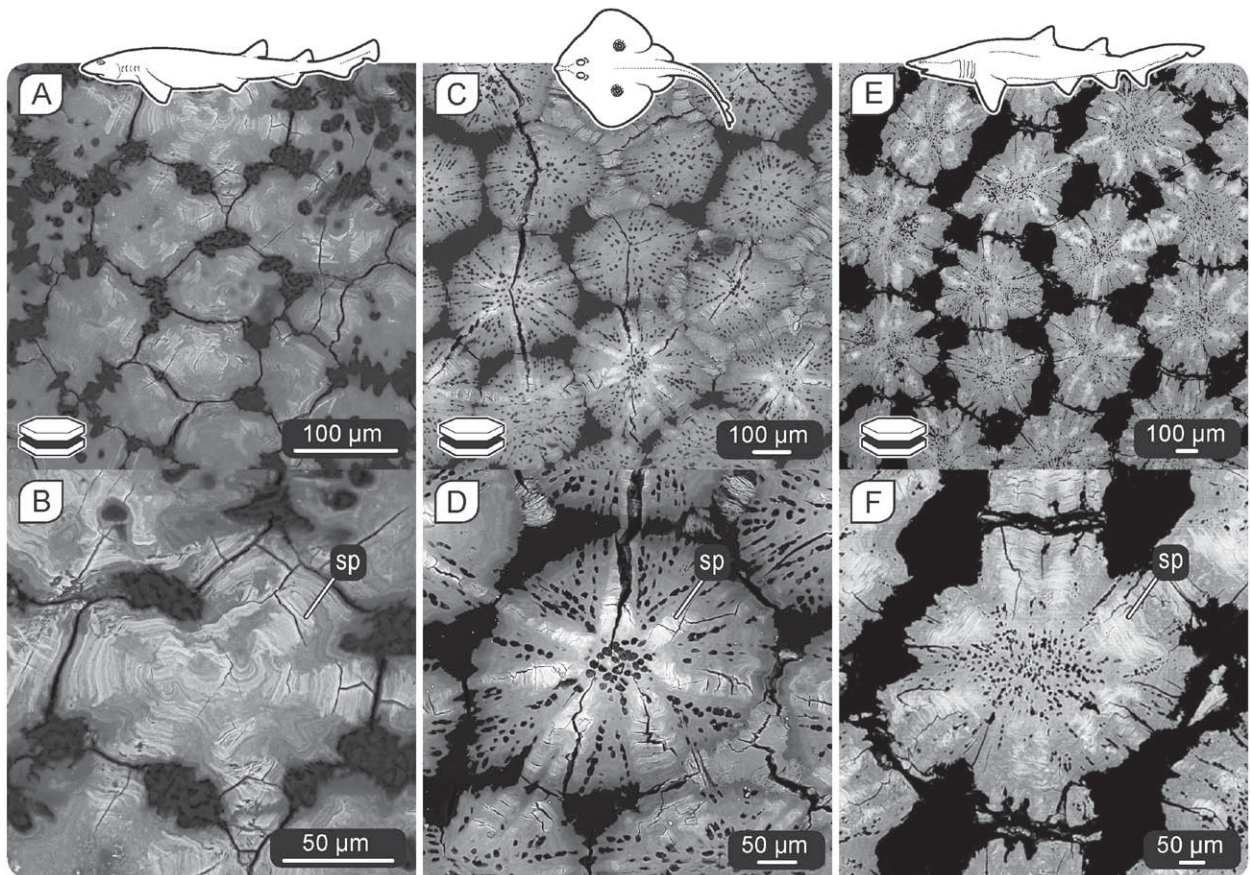

Fig. 11 Mineral density variation and tissue reinforcement – spokes in other elasmobranch species.

(A, B) *Scyliorhinus retifer*, (C, D) *Leucoraja naevus*, (E, F) *Carcharias taurus*. Note that spokes are present in all species, and that all spokes lack cells and exhibit the same hyper-mineralization and laminar structure as the spokes of *Urobatis halleri*.

sections of μCT-scanned tesserae (Fig. 8E) confirm our backscatter SEM observations (e.g. Figs 4–6) that acellular and cellular areas are associated with intertesseral contact surfaces and fibrous zones, respectively.

4.3.4 Interspecies comparisons

Many common features were observed among the tesserae of adult *U. halleri* and those of other elasmobranch species investigated by SR-μCT (Fig. 10) and backscatter SEM (Fig. 11). With the exception of the sleeper shark (S. pacificus; not shown), lower jaw cartilages from all examined species exhibited tesserae. Lacunar spaces were visible in great numbers in all species' tesserae, except for those of the sevengill shark *N. cepedianus*, which contained either very few or no lacunar spaces (Fig. 10L). In vertical sections through the center of tesserae, the flat, perichondrally associated lacunae formed an inverted pyramid shape, similar to what we observed in *U. halleri* (Fig. 10A–E,H,K). As in *U. halleri*, aligned collagen fibers span the IFZ between tesserae, and spokes were present at points/zones of intertesseral contact in most of the examined species (Figs 10 and 11).

All types of mineral density variation reported for *U. halleri* tesserae (i.e. Liesegang lines, spokes and filled lacunae) were also observed in other species' tesserae using SR-μCT (Fig. 10), most clearly though in backscatter SEM (Fig. 11). The most prominent difference among species was the variation in tesseral shape and size: tesserae ranged from stellate (Fig. 10B) to nearly circular (Fig. 10H) in planar view, and from rather flat discs (Fig. 10I) to rectangular blocks (Fig. 10D) in vertical view.

4.4 DISCUSSION

4.4.1 General growth and ultrastructure concepts

Our data show that the characteristic tessellated pattern of the adult elasmobranch skeleton is absent before birth in *U. halleri*. In fact, in yolk sac embryos of *U. halleri*, tesserae could not be detected using μCT and backscatter SEM. At the early histotroph stage, the tessellated mineralization of the cartilage surface appeared patchy in μCT, being most developed along the ventral margin of skeletal elements towards the chondocranium (Fig. 2A). Further, the existing tesserae differed in the degree of mineralization, which suggests that the formation of tesserae is locally controlled (see below). In later developmental stages, all investigated skeletal elements were completely sheathed in mineralized tesserae, which varied in thickness but appeared to have a similar degree of mineralization (Fig. 2B–D). In adult specimens, the size and shape of tesserae varied between regions on the skeletal element, with generally thicker tesserae in strongly convex areas (e.g. the dorsal and ventral margins of hyomandibulae; Fig. 2C,D). Tesserae continued to increase in both depth and width with age, which agrees with previous observations of *U. halleri* (Dean et al. 2009) and one other elasmobranch species (*Squalus*

acanthias: Benzer, 1944), and supports the idea that accretion (i.e. deposition of mineralized tissue at tesseral margins) is a central mechanism of mineralized tissue growth in this system.

We demonstrate that adult *U. halleri* tesserae exhibit highly heterogeneous calcification, forming features such as spokes, Liesegang lines and filled (hypermineralized) lacunae (Figs 4–7, discussed each in turn below). We believe that Liesegang lines and spokes reflect successive, accretive mineralization events, following the contours of nearby features (e.g. lacunar spaces, tesseral edges), and in this way are structural records of the former shapes and locations of tesseral borders (mineralization fronts). In this growth model, the oldest portions of tesserae are closest to the center of each tile. Our ultra-structural data support the theory that new layers are built on top of older ones without remodelling: we never observed intersections of consecutive Liesegang lines or abrupt cessation of the pattern that might suggest local restructuring of tissue, supporting previous assertions that elasmobranchs lack the ability to repair skeletal damage (Clement, 1986; Ashhurst, 2004; Huber et al. 2013). This is in contrast to, for example, osteonal bone where newer osteons intersect and interrupt older ones, providing a visual record of remodelling activity (Atkins et al. 2014). Calcium-labeling of developing skeletons (e.g. with calcein) may help to determine how these patterns relate to mineral deposition.

4.4.2 Liesegang lines as records of accretive growth

Liesegang lines have been observed in the tesserae of both extant and extinct elasmobranch species (e.g. plates 6–7 in Ørvig, 1951; figs 2–7 in Applegate, 1967; fig. 16 in Kemp & Westrin, 1979; fig. 10 in Peignoux-Deville et al. 1982; fig. 2 in Takagi et al. 1984; fig. 6 in Bordat, 1988; plate 5 in Clement, 1992; fig. 7F in Johanson et al. 2010). Our backscatter SEM data demonstrate that Liesegang lines are bands of varying mineral density and not simply homogeneously mineralized layers added on top of previous layers. This is supported by the few other published backscatter SEM images of tesserae, which depict similar features (from *U. halleri*: fig. 2A in Omelon et al. 2014; fig. 1F in Dean et al. 2015; from an unnamed species and sectioning plane: fig. 7F in Johanson et al. 2010). Kemp & Westrin (1979) suggested that Liesegang lines in tesserae might be caused by periodic secretion of enzymes or other cell products in

the uncalcified extracellular matrix (ECM); however, it is possible that these structures are formed without such control. The phenomenon of periodic and concentric precipitation bands – variously called Liesegang 'lines', 'rings' or 'bands' – has been recognized in a variety of biological, chemical and geological systems for over a century (Liesegang, 1907; see Stern, 1967 for a bibliography of Liesegang rings). Although there is still no unified theory as to their formation, it is generally accepted that the Liesegang line pattern can be created by an oscillating chemical reaction between components diffusing in a medium (Liesegang, 1907; Thompson, 1942; Henisch, 2005; Kuz'min et al. 2013). The interaction results in periodic precipitation and depletion events that need not be biologically regu-

lated. This implies that if components for mineralization are available at the mineralization front, then the concentric Liesegang bands characteristic of tesserae could form passively from cycles of nucleation and depletion. In this scenario, regulation would primarily be necessary in the processes that deliver materials for mineralization to mineralization fronts (e.g. potentially via vesicular transport; Kemp & Westrin, 1979; Clement, 1986; Bordat, 1988; Takagi et al. 1984) and in those that prepare them for assembly (e.g. the interaction of the enzyme ALP with polyphosphates, liberating inorganic phosphate for skeletal mineralization; Omelon et al. 2014).

Our data suggest that Liesegang lines are associated with mineralization events where the concentrations of organic and inorganic components vary inversely. In decalcified sections of tesserae examined with TEM (Fig. 6H), Liesegang lines in the body zone continued to be visible as collagenous bands of varying electron density that inversely mirrored the local mineral density variation (Blumer et al. 2015). There is also likely concomitant variation in non-collagenous matrix organic components (e.g. proteoglycans), as Liesegang lines exhibit varying degrees of basophilia (affinity to the hematoxylin stain in H&E histology; Blumer et al. 2015). This may represent cyclic variation in the concentrations of negatively charged glycosaminoglycans (and proteoglycans) in the mineralizing ECM. Elasmobranch proteoglycans have been shown to be effective inhibitors of hydroxyapatite crystal formation (Gelsleichter et al. 1995); Liesegang lines could reflect the degree to which proteoglycans in successive bands are dismantled to facilitate mineralization. In this way, the relationship between mineralization processes and the ultrastructure, mineral density and staining of Liesegang bands, stands to greatly inform our understanding of growth and mineralization regulation processes of tesserae.

4.4.3 Proposed phases of tesseral growth and skeletal mineralization

Liesegang lines and the filigreed pattern between them are characteristic of the chondral portion of adult tesserae, but are not found in the cap zone or the lateral portions of tesserae, neighboring ICZs (Figs 4B and 8F). We believe these differences in ultrastructure between the chondral portion and the rest of a tessera reflect the history of growth, how and when the tessera came into contact with surrounding tissues (e.g. perichondrium, adjacent tesserae) during ontogeny. From this, we propose several different phases in the developmental progression of tessellation.

The first phase we propose for *U. halleri* cartilage calcification (Fig. 12A–D) constitutes the early development of tesserae in histotrophic animals, when tesserae are still separated by uncalcified cartilage matrix (Fig. 3A,B). Tesserae of young animals of other species have also been reported as separate (non-abutting) mineralized islands (Bordat, 1988; Maisey, 2013), suggesting this may be common young morphology among elasmobranch tessellations. Tesserae in *U. halleri* are apparently first formed by the accretion of numerous small globules of mineralized cartilage, filling the interstices between cells (Fig. 3A,B; Benzer, 1944; Ørvig, 1951; for other species see also Bordat, 1988); these
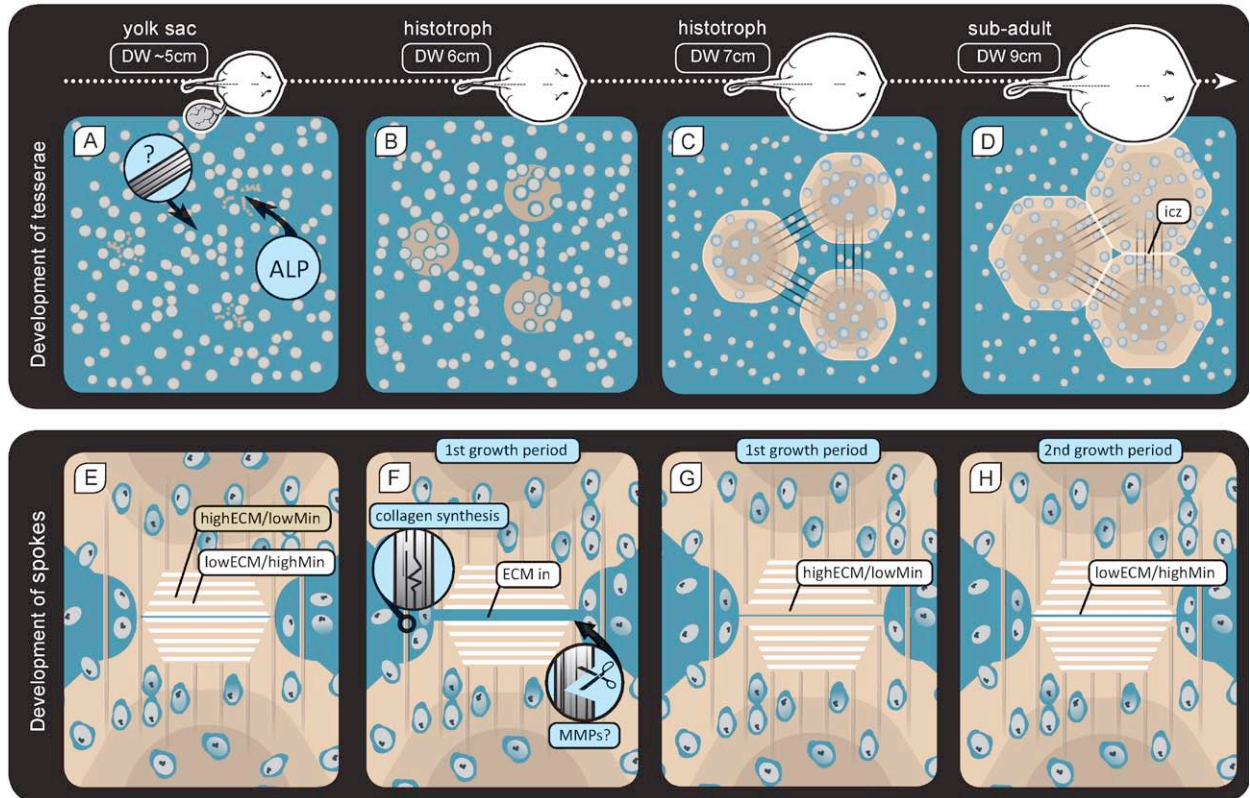
Fig. 12 Hypothesis of the development of tesserae and spoke laminae.
(A–C) Schematic of the tesseral development when tesserae are separated from each other. (A) Minute mineralized globules develop between chondrocytes, associated with localized alkaline phosphatase (ALP) activity (Eames et al. 2007). We observed no evidence for specific orientation of collagen fibers at this stage. (B) 'Proto-tesserae' (~ 100 μm wide) are agglomerations of mineralized globules. The obvious collagen fibers of the developing intertesseral joints appear to develop around this age. (C) Tesserae grow by accreting new mineral at their margins, forming Liesegang lines of varying mineral density (see Fig. 4). (D) The second growth phase of tesserae (D–H) begins when adjacent tesserae come into direct contact at the intertesseral joints, coincident with the appearance of spokes. (E–H) Abutting tesserae of sub-adult and adult animals, illustrating the development of spoke laminae in a cycle of two alternating growth periods: a high-extracellular matrix (ECM)/low mineral content growth period, forming dark bands (F–G), and a low-ECM/high mineral content growth period, forming bright bands (H). We observed neither fibrous matrix nor cells in the contact zones between tesserae. (F) In the high-ECM/ low mineral content period, we propose that small amounts of distance are created in contact zones by the breaking down (perhaps by matrix metalloproteinases, MMPs) and rebuilding of collagen in the adjacent fibrous zones. ECM from the fibrous zones is directed to fill the space (F) and is then mineralized (G) In the low-ECM/high mineral content period (H), tesseral edges bordering the contact zone accrete hyper-mineralized tissue with little to no ECM.

isolated tesserae apparently continue to accrete mineral at their margins, resulting in the Liesegang lines described above. We saw no evidence in *U. halleri* to support Bordat's (1988) hypothesis that tesserae start as separate perichondral and chondral structures that grow together, suggesting that Bordat's observations for *S. canicula* could have been artifacts of sectioning young tesserae with deeply fluted edges. Based on our ultrastructure and ontogeny data and the general model of accretionary
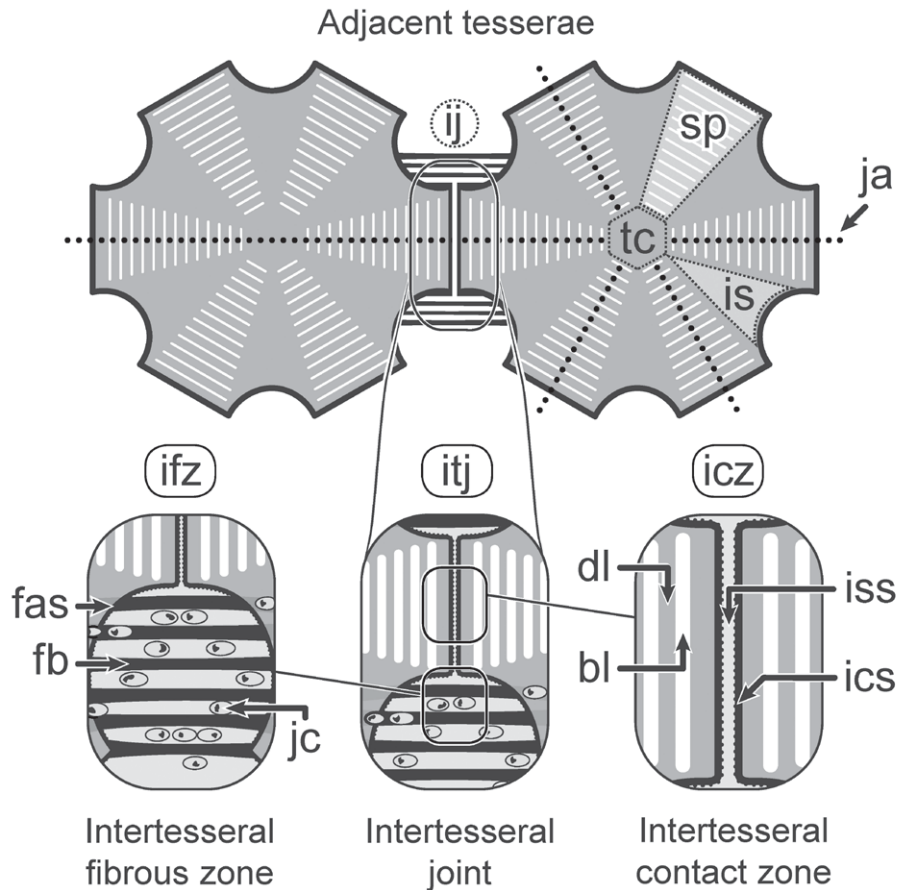
Fig. 13 Schematic of two abutting adult tesserae in planar view, summarizing diagnostic ultrastructural features defined in this study.
Compare with the previous, more simplistic notion of tesserae in Fig. 1. The two predominant portions of the intertesseral joints are displayed: (1) intertesseral fibrous zones, containing cells and fibrous tissue connecting adjacent tesserae; and (2) intertesseral contact zones, where the tesserae abut against one another. Spokes are coincident with contact zones and are acellular, whereas the rest of the tesserae body contains lacunar spaces, which house cells (not shown). bl, bright laminae in spokes; dl, dark laminae in spokes; fas, fiber attachment surface with fb, fiber bundles spanning the ifz, intertesseral fibrous zone at the itj, intertesseral joint; ics, intertesseral contact surfaces at the icz, intertesseral contact zone border the iss, interstitial space; is, inter-spoke area; ja, joint axis; jc, joint-adjacent cells; sp, spokes; tc, tesserae; ij, intertesseral junction.

growth proposed above, we believe these 'proto-tesserae' correspond to the central region (body zone) in adult tesserae. Unlike in older tesseral mats (> 10 cm animal DW), we saw no evidence for the presence of an organized collagenous network, comprised of parallel aligned fiber bundles, connecting the early centers of tesserae (or scaffolding the early growth). Therefore, based on PLM, the lack of birefringent collagen fiber bundles between tesserae in very young *U. halleri* skeletons suggests that other organizing mechanisms, apart from a collagen network, define the initial tessellation pattern. Eames et al. (2007) demonstrated discrete zones of activity of ALP in embryonic, pre-tessellated swell sharks

Cephaloscyllium ventriosum that appeared to predict the locations of future tesserae. ALP has been localized to mineralization fronts in adult *U. halleri* tesserae (Omelon et al. 2014), and is also known to be present in adult elasmobranch blood (Urist, 1961, 1962, 1967). It is reasonable to assume that ALP is active in early (phase I) tesserae, in *U. halleri* and other elasmobranch species; however, this has yet to be demonstrated. The source of ALP in elasmobranch skeletons and the mechanisms coordinating its localized, punctate expression in pre-tessellated skeletons also remain to be investigated.

The second proposed phase of tesserae growth (Fig. 12D–H) begins when tesserae grow into contact with the perichondrium and into direct contact with one another, coincident with the first signs of hyper-mineralized tesseral spokes (see below). At this point, the cap zone begins to form. The presence of thicker, Type I collagen fibers from the perichondrium (Blumer et al. 2015) appears to alter the nature of the interaction between mineral and organic materials, as the ultrastructure of cap zone tissue is visibly different from that of body zone tissue (Figs 4G and 8B; Kemp & Westrin, 1979; Clement, 1992). Our backscatter SEM images and SR-µCT reconstructions agree with Kemp & Westrin (1979), who showed that in macerated samples of adult tesserae, the rough perichondral tesseral surface was covered with aligned hydroxyapatite crystallites whereas the opposing chondral surface showed globular calcification (Figs 4H and 8C; Kemp & Westrin, 1979; Clement, 1992). The overall mineral densities of *U. halleri* cap and body zones, however, do not differ significantly according to our backscatter SEM imaging (e.g. Fig. 4B).

4.4.4 Spoke ultrastructure and development

Under backscatter SEM imaging, spokes are the most prominent feature of tesserae in sub-adult and adult *U. halleri*. Spokes were never observed in the isolated (non-abutting) tesserae of histotroph animals, and so we hypothesize that their formation is dictated by the interaction of adjacent tesserae at contact zones. Backscatter SEM imaging shows that spoke laminae from two abutting tesserae with similar distance to the ICZ mirror each other's morphology, even those laminae that are far from the joint (Fig. 6B). Therefore, we propose that spokes' laminae, like Liesegang lines, depict stages of growth in tesserae, and because the appearance of spokes is coincident with the development of the intertesseral joint, spokes' laminae reflect the shapes of former contact zones of abutting tesserae.

As far as we are aware, spokes have never been described as features of tesserae, although we believe they appear in the figures of multiple previous studies of a variety of elasmobranch species (e.g. Fig. 13 in Kemp & Westrin, 1979; Fig. 2 in Lee et al. 1984; Fig. 1 in Bordat, 1988; Fig. 3H in Ortiz-Delgado et al. 2006; Fig. 6E in Johanson et al. 2010; and perhaps in the oldest tessellated shark fossil, Fig. 8B,C in Long et al. 2015). Our backscatter SEM and SR-µCT data for multiple shark and batoid species further verify that spokes are common features of tesserae (Figs 10 and 11). The reason for spokes being overlooked by previous authors surely relates, to a large degree, to the dearth of published

backscatter SEM images of tesserae, but is also likely a function of ultrastructural aspects of the spokes themselves and their response to sample preparation. Spokes are characterized by alternating laminae of high and low mineral content. TEM imaging of decalcified sections through abutting tesserae revealed that the organic matrix underlying spokes is similarly patterned, where the density of organic tissue is the inverse of the mineral density (Fig. 6H; Blumer et al. 2015). The high mineral density laminae have such low organic content, that when samples are decalcified and mineral is removed, these bands are nearly devoid of supporting tissue (Fig. 6E–H). As a result, spokes appear merely as a series of gaps in the tissue in decalcified sections, and therefore could easily be taken as artifacts (e.g. 'knife stutter' in sectioned tissue).

The consistent location of spokes, their lack of cells, and their distinct laminated structure (in particular the high mineral density 'bright' laminae), imply that their development may differ from that of the periodic Liesegang lines. We hypothesize a specific growth mechanism for spokes, concurrent with the lateral enlargement of tesserae in the second proposed phase of tesseral growth. The model is predicated on several observations from this study: (i) there is very little room for growth between tesserae at contact zones; (ii) the narrow interstitial spaces at contact zones appear to be devoid of cells and low in matrix content; (iii) spoke laminae from two abutting tesserae with similar distance to the ICZ mirror each other's morphologies; and (iv) spokes are comprised of alternating high and lower mineral density bands that appear to be patterned on very low and higher organic tissue frameworks, respectively.

Based on these observations, we hypothesize a two-period growth cycle for spokes, beginning at the first contact of adjacent tesserae (i.e. the start of the second phase of tesseral growth): (i) a high-ECM/low mineral content growth period; and (ii) a low-ECM/high mineral content period (Fig. 12). At the start of the high-ECM/low mineral content growth period, tesserae are in close contact and tethered together by intertesseral fibers (Fig. 12E); therefore, intertesseral growth must involve an elongation of intertesseral collagen fibers, linking two adjacent tesserae, to 'make room' for the deposition of new mineralized material (i.e. at the distal ends of spokes). However, as inter-tesseral collagen fibers extend uninterrupted into tesserae (i.e. with no exposed ends for new tissue addition; Fig. 7F; see also Blumer et al. 2015), fiber elongation must involve a severing of individual fibers (e.g. via matrix metalloproteinases or other enzymes) in order to introduce interstitial length (Fig. 12F). As this 'slack' is added into the system, new ECM, perhaps produced and directed by joint-adjacent cells (see below), would fill the gap between the two tesserae and mineralize (Fig. 12G). This would result in a comparatively low mineral density and high organic content mineralized layer, a dark spoke lamina in backscatter SEM. The mechanisms underlying the second growth period (Fig. 12H), the subsequent deposition of a low-ECM/high mineral content band (bright spoke lamina), are less obvious. Perhaps apatite continues to nucleate on the exposed, distal edge of dark spoke laminae after the available ECM has been mineralized. At this stage, these hypotheses of spoke growth are based purely on the

laminated morphology of the tissue; high-resolution in situ analyses of enzyme and cellular activity at contact zones are required for support of these hypotheses.

The apparent lack of cells in the interstitial space between tesseral edges at contact zones of *U. halleri* (Figs 7A–C, 9 and 10) is counterintuitive, as there is growing evidence that cells are involved in tesseral mineralization (Trivett et al. 2002; Egerbacher et al. 2006; Ortiz-Delgado et al. 2006; Omelon et al. 2014). Also, the apparent lack of ECM in the ICZ goes against our observations that dark spoke bands are based on organic material (e.g. the collagen in the uncalcified cartilage matrix). We, therefore, posit that the fiber- and cell-rich IFZ at the joints (Figs 8D and 9E–J) are involved in the regulation of spoke growth (e.g. via expression of enzymes and growth factors) and the determination of where and when mineralization occurs at joints. In this way, the cell-rich fibrous zones adjacent to contact zones may also play a role in maintaining the patency of intertesseral joints (i.e. the non-fusion of adjacent tesserae), which is critical to skeletal growth. Although we have never observed fusions of adjacent tesserae, previous authors have reported these in other species (Applegate, 1967; Maisey, 2013), suggesting that the inhibition of joint mineralization can either break down or be relaxed.

4.4.5 The role of cells, micropetrosis and interspecific variation in tesserae

The variation we report in lacunar shape among different tesseral regions (cap and body zone) is likely tied to their different tissue associations. Whereas the rounder body zone lacunae were present from the inception of tesserae, the flatter cap zone lacunae did not appear until the second phase of growth. The shape distinction between the cap zone and body zone lacunae and the inverted pyramid shape formed by the former was observed in a variety of species in this study (Fig. 10), implying that the growth phases proposed above could be shared among different taxa. Some species, however, showed strikingly different morphologies, exhibiting tesserae with nearly only flattened lacunae (i.e. similar to cap zone lacunae; Fig. 10D: *R. stellulata*) or rounded lacunae (i.e. body zone-like; Fig. 10I: *T. californica*), and/or tesserae with comparatively few lacunae (Fig. 10J: *T. californica*) or almost no lacunae at all (Fig. 10L: *N. cepedianus*). Despite some apparent commonalities among tesserae (e.g. flat, non-interdigitating contact zones, spokes and filled lacunae, see below), the observed shape variation in lacunae and whole tesserae (Figs 10 and 11) suggests that there may be species-level variation in tesseral growth mechanisms. The tessellated cartilage system may, therefore, provide a naturally diverse palette for investigating cellular and ECM associations in vertebrate skeletal mineralization processes.

The cells within tesserae provide another indication that elasmobranch chondrocytes can control mineralization of their local environment. As tesserae thicken during ontogeny, chondrocytes from the underlying uncalcified cartilage are incorporated alive into tesserae via a process of encapsulation, whereby globular mineralized tissue engulfs cells into lacunar spaces in the mineralized matrix (Tretjakoff, 1926; Halstead, 1974; Kemp & Westrin, 1979; Takagi et al. 1984; Bordat, 1988; Dean et al.

2008, 2009, 2010). A surrounding layer of uncalcified cartilage is engulfed with each chondrocyte, and fills the space between the cell and lacunar walls (Kemp & Westrin, 1979; Bordat, 1988; Dean et al. 2010). Intratesseral cells likely remain alive due to the continuity of the uncalcified ECM in canalicular networks (i.e. inter-lacunar passages), which would permit the transmission of nutrients, but also enable communication between cells (Dean et al. 2010). This arrangement is quite different from the calcified cartilage of other vertebrates (e.g. anywhere endochondral ossification occurs, such as at the end of long bones or the growth plate) where chondrocytes undergo apoptosis during mineralization, resulting in a largely acellular mineralized matrix (Kirsch et al. 2003). The intratesseral cell network is, therefore, in a manner, more similar to the lacunar–canalicular network connecting living, entombed cells (osteocytes) in bone. Osteocytes are believed to monitor their mechanical environment through this network, allowing them to respond to the changes in bulk tissue strain that would result from new or extreme loading regimes or bone fracture (Currey, 2002; Atkins et al. 2014). The intratesseral cellular network could, therefore, provide a similar basis for monitoring the skeleton's mechanical environment. However, the tendril-like cell processes that link bone cells for cell–cell communication are apparently missing in intertesseral chondrocytes and chondrocytes in general (Dean et al. 2009, 2010). If elasmobranchs are indeed incapable of repairing their skeletons (Clement, 1986; Ashhurst, 2004), then monitoring the health of deep intratesseral tissue may be irrelevant and intratesseral cells may instead survive only to provide some assistance (e.g. via synthesis of ECM and/or collagen synthesis) for cells 'downstream' in the lacunar–canalicular network at the mineralization fronts at the periphery of tesserae. Recent identification of lacunar spaces within the calcified cartilage of the chondricthyan fossil Gogoselachus, believed to possess an early transitional type of tesserae, suggests that further studies of lacunar morphology may provide insight also into the evolution of tesserae and the skeletal biology of extinct taxa (Long et al. 2015).

The intratesseral lacunar–canalicular network relies on the incorporation and maintenance of open, matrix-filled spaces in tesserae, and likely requires the continued inhibition of mineralization local to incorporated chondrocytes (Dean et al. 2015). It is plausible that, as chondrocytes age, a breakdown of the inhibitory process that maintains the capsular zone leads to the progressive mineralization and decrease in size of lacunar spaces. This is supported by our observations and observations of other authors (Bordat, 1988; fig. 7F in Johanson et al. 2010) that mineral-filled lacunar spaces were located primarily in the middle of tesserae (Fig. 4B,G), which we believe to contain the oldest entombed cells. The mineralization of lacunae could be triggered by cell death, distal blockages in the lacunar– canalicular network, and/or tesserae reaching a critical size that limits central cells' access to nutrients. There are few available data on the biology of elasmobranch chondrocytes; however, assuming a no-remodeling, accretive growth model for tesserae, it may be possible to use the occurrence of hypermineralized lacunae to estimate the lifespan of elasmobranch chondrocytes. We first noted hypermineralized

lacunae in sub-adult animals (11 cm DW), which, based on available age and growth data for *U. halleri*, could indicate that elasmobranch chondrocytes survive for approximately 1 year (Hale & Lowe, 2008). This would suggest a much shorter lifespan than the ~ 20 year half-life proposed for mammalian chondrocytes (Stockwell, 1967; Bobacz et al. 2004). Backscatter SEM revealed that the mineralized, filled lacunar spaces in *U. halleri* are highly mineralized compared with the rest of the tesseral body, which we assume is in part due to the low organic content of the non-mineralized matrix in lacunar spaces before they mineralize. We observed filled lacunae in backscatter SEM images of tesserae from several other genera as well (e.g. Amblyraja, Leucoraja, Negaprion, Raja and Scyliorhinus), indicating that this feature is not unique to *U. halleri*.

Tesseral lacunar hypermineralization is curiously similar to the phenomenon of 'micropetrosis' in bone, whereby osteocyte lacunae are filled with high mineral density material (Frost, 1960; Remaggi et al. 1996; Carpentier et al. 2012). This has been observed in humans more than other mammalian taxa (Frost, 1960) and seems to be linked to lifespan, with the incidence of micropetrotic lacunae increasing with age (Remaggi et al. 1996; Busse et al. 2010; Carpentier et al. 2012). Human micropetrosis results in an occlusion of the lacunar–canalicular network (Frost, 1960; Carpentier et al. 2012), but it is unknown whether the phenomenon is the result of an active cellular process (e.g. via matrix vesicle-mediated mineralization) or a byproduct of cell death (e.g. via removal of mineralization inhibitors and/or apoptotic-body facilitated mineralization; Kirsch et al. 2003; Busse et al. 2010). Human micropetrotic material is comprised of accretions of hypermineralized spherites (Carpentier et al. 2012) that appear similar in form to the globular mineralization we observed along tesseral chondral edges and sometimes lining the walls of intratesseral lacunae (data not shown), suggesting some mineralization processes may be shared between bone and tesseral lacunar hypermineralization.

4.5 CONCLUSIONS

In summary, our analysis of the ontogeny of *U. halleri* tesseral ultrastructure has shown that, although the tessellated pattern is established early in development as an array of mineralized islands, the characteristic tessellated morphology of elasmobranchs does not form until these nodes grow together to form abutting, geometric tiles. Although adjacent adult tesserae are in close contact, at the ultrastructural level they are not entirely flat-edged: the intertesseral joint space is a complex arrangement of spatially discrete, planar contact zones with no interdigitations, interspersed with concave pockets of fibrous/cellular material (Fig. 13). The combination of mineralized bearing surfaces and fibrous attachments are likely the structural bases for intertesseral joints functioning effectively in both compression and tension loading (Liu et al. 2010, 2014; Fratzl et al. 2016).

All edges of tesserae appear to serve as surfaces for mineral deposition during ontogeny, leaving

telltale marks in tesseral ultrastructure. Particularly under backscatter SEM imaging, these features may provide reliable determination of ontogenetic stage, but also clues – via aspects of cell shape and spoke presence and morphology – to the developmental mechanisms of less-studied taxa, which exhibit different tesseral shapes and/or lacunar arrangements. The hypermineralized features we have described have implications for the mechanics of the tesseral mat (e.g. load-channelling through joints and spokes to avoid cell damage), but also suggest some commonalities with bony skeletons (e.g. micropetrosis). This could indicate that some mineralization processes involved in the generation and maintenance of the tessellated morphology are deeply conserved, both among vertebrate taxa and across skeletal tissue types.

4.6   ACKNOWLEDGEMENTS

4.7   AUTHORS CONTRIBUTION

R Seidel, MN Dean: data acquisition, data analyses, illustrations, writing of the manuscript. K Lyons, M Blumer, P Zaslansky, P Fratzl, JC Weaver: data acquisition, reviewing of the manuscript.

4.8   REFERENCES

Please see the concatenated reference list at the end for all citations provided within this thesis.

> TRANSITION:

In this chapter I presented data focussing largely on the characterization of the mineral phase of tessellated cartilage. Ontogenetic series of tesserae presented in vertical and planar sections/views revealed the development of the characteristic tiling pattern observed in adult tessellated cartilage in stingray *Urobatis halleri*, as well as intra-tesseral features of mineral density variation appearing to be a result of tesserae interaction, growth and mineral deposition.

In the following chapter I present data on the soft tissue, the collagenous composition, underlying tessellated cartilage, aiming to answer a long-standing question: "Are tesserae are more like bone or calcified cartilage"? <

5. Calcified cartilage or bone? Collagens in the tessellated endoskeletons of cartilaginous fish (sharks and rays)

Ronald Seidel [a], Michael Blumer [b], Elisabeth-Judith Pechriggl [b], Kady Lyons [c], Brian K. Hall [d], Peter Fratzl [a], James C. Weaver [e], Mason N. Dean [a]

[a] Department Biomaterials, Max Planck Institute of Colloids & Interfaces, Potsdam, Germany
[b] Division of Clinical and Functional Anatomy, Medical University of Innsbruck, Innsbruck, Austria
[c] Department of Biological Sciences, California State University Long Beach, Long Beach, CA, USA
[d] Department of Biology, Dalhousie University, Halifax NS Canada
[e] Wyss Institute for Biologically Inspired Engineering, Harvard University, Cambridge, MA, USA

ABSTRACT

The primary skeletal tissue in elasmobranchs –sharks, rays and relatives– is cartilage, forming both embryonic and adult endoskeletons. Only the skeletal surface calcifies, exhibiting mineralized tiles (tesserae) sandwiched between a cartilage core and overlying fibrous perichondrium. These two tissues are based on different collagens (Coll II and I, respectively), fueling a long-standing debate as to whether tesserae are more like calcified cartilage or bone (Coll 1-based) in their matrix composition. We demonstrate that stingray (*Urobatis halleri*) tesserae are bipartite, having an upper Coll I-based 'cap' that merges into a lower Coll II-based 'body' zone, although tesserae are surrounded by cartilage. We identify a 'supratesseral' unmineralized cartilage layer, between tesserae and perichondrium, distinguished from the cartilage core in containing Coll I and X (a common marker for mammalian mineralization), in addition to Coll II. Chondrocytes within tesserae appear intact and sit in lacunae filled with Coll II-based matrix, suggesting tesserae originate in cartilage, despite comprising a diversity of collagens. Intertesseral joints are also complex in their collagenous composition, being similar to supratesseral cartilage closer to the perichondrium, but containing unidentified fibrils nearer the cartilage core. Our results indicate a unique potential for tessellated cartilage in skeletal biology research, since it lacks features believed diagnostic for vertebrate cartilage mineralization (e.g. hypertrophic and apoptotic chondrocytes), while offering morphologies amenable for investigating the regulation of complex mineralized ultrastructure and tissues patterned on multiple collagens.

Keywords: Vertebrate skeleton, tesserae, cartilage, chondrocytes, collagens

5.1 INTRODUCTION

The skeletons of most vertebrates undergo a major material and tissue transition during ontogeny. Embryonic vertebrate skeletons are primarily comprised of hyaline cartilage, a gel-like, aneural and avascular tissue produced by chondrocytes, originating from mesenchymal scleroblasts of the peri-chondrium (Hall, 1975, 2005; Staines et al., 2013). During development, this primary cartilage is largely replaced by endochondral bone via a calcification process (known as endochondral ossification) that involves drastic alterations to tissue composition, cellular morphology and protein expression, relative to that seen in resting cartilage. Chondrocytes near the mineralization front are enlarged in volume by 10–40× (hypertrophy; Farnum et al., 2002; Cooper et al., 2013), accompanied by a local up-regulation of type-X collagen (Coll X), alkaline phosphatase (ALP) (Heinegård and Oldberg, 1989; Gannon et al., 1991; Stephens et al., 1992), and vascular endothelial growth factor (VEGF) (Studer et al., 2012), the latter promoting vascularization (Maes et al., 2010; Dirckx et al., 2013).

The transition from hypertrophic cartilage to bone demands a complete change in the fibrous scaffolding of the tissue, whereby collagenous and non-collagenous proteins (e.g. proteoglycans) are degraded by matrix metalloproteinases (e.g. MMP13, membrane type 1-MMP; Poole, 1991; Holmbeck et al., 1999). The result is a shift in the type-II collagen (Coll II)-based extracellular matrix composition of cartilage to the type-I collagen (Coll I)-based matrix of bone (Hall, 2005; Fratzl, 2008). It has been widely accepted that chondrocytes do not survive this process (e.g. Maes et al., 2010), dying either by apoptosis or perhaps by phagocytosis during matrix mineralization (reviewed in Hinton et al., 2017). Recent findings, however, argue that some chondrocytes contribute to the osteocyte pool, transforming directly into bone matrix-secreting cells in developing long bone growth plates and fracture calluses (reviewed in Hinton et al., 2017). This challenge to the dogma of chondrogenesis and osteogenesis as separate processes also raises the argument that the role of chondrocytes may be more variable than typically believed.

The endoskeletons of sharks and rays (elasmobranchs) differ from those of other vertebrates in that they are comprised predominantly of a hyaline-like cartilage that persists throughout life and is never converted to or replaced by bone (Daniel, 1922; Applegate, 1967; Kemp and Westrin, 1979; Clement, 1992; Dean and Summers, 2006; Dean et al., 2009; Seidel et al., 2016). During ontogeny, however, the matrix undergoes a distinctive calcification, developing an outer calcified rind comprised of minute, polygonal tiles (tesserae), sandwiched between the cartilaginous core and the outer, fibrous perichondrium (Fig. 1; Kemp and Westrin, 1979; Dean et al., 2009; Seidel et al., 2016). Tesserae, therefore, intervene between connective tissues comprised of different collagens – Coll II in cartilage and Coll I in perichondrium (Conrad et al., 1981; Eames et al., 2007; Egerbacher et al., 2006). However, it is not clear whether elasmobranch tesserae are patterned on Coll I (i.e. bone-like), on Coll II (i.e. effectively calcified cartilage), or on some hybrid combination of collagens (e.g. calcified cartilage with

a "thin veneer of bone" sensu Kemp and Westrin, 1979), similar to the intermediate tissue architecture of chondroid bone (Beresford, 1981; Witten and Hall, 2002; Witten et al., 2010). Previous studies characterizing elasmobranch skeletal collagens were largely not aimed at determining the collagen types in tesserae specifically (Table 1). Some used 'homogenized' tissue and/or non-specific 'cartilage tissue' (i.e. likely mixing cartilage, perichondrium and tesserae: Peignoux-Deville et al., 1982; Rama and Chandrakasan, 1984; Sivakumar and Chandrakasan, 1998; Mizuta et al., 2003), while others investigated embryonic cartilage that had not yet formed tesserae (Eames et al., 2007), tesserae in early developmental stages (Enault et al., 2015), or adult cartilages that lacked tesserae (Conrad et al., 1981).

Enault et al.'s (2015) recent molecular study of vertebrate skeletal tissues, including tessellated cartilage of the catshark *Scyliorhinus canicula*, provided the most tesserae-specific examination into elasmobranch skeletal collagens to date, demonstrating Coll II immunostaining and a complete absence of Coll I reactivity in tesserae. However, other evidence argues that Enault et al.'s use of embryonic specimens (≤9 cm total length, TL) may have biased their results toward an earlier developmental stage of tesserae and so may not provide a complete window into elasmobranch skeletal organization. Firstly, immunohistochemical work by Egerbacher et al. (2006) on older *S. canicula* specimens (29–35 cm TL) suggested an alternative constitution for tesserae, with a purely Coll I composition and with Coll II localized only in the unmineralized cartilage of the skeletal core. Secondly, although recent developmental and ultrastructural data of tesserae from round stingray *Urobatis halleri* (Seidel et al., 2016) showed that tesserae form beneath the cartilage surface in embryos, supporting previous observations in other elasmobranchs (Wurmbach, 1932; Schmidt, 1952; Kemp and Westrin, 1979; Bordat, 1988; Enault et al., 2015), they do not remain only associated with the unmineralized cartilage.

Urobatis halleri tesserae only later come in contact with the overlying perichondrium in sub-adult animals, a result of tesserae growing by apposition in all directions (Dean et al., 2009; Seidel et al., 2016). After this point, adult tesserae —of *U. halleri*, but also of other elasmobranchs— are comprised of two regions, distinct in the shape of their cells and lacunae and their tissue ultrastructure (Fig. 1; Kemp and Westrin, 1979; Seidel et al., 2016). Cells living in the 'cap' zone, bordering the perichondrium, exhibit a more fibroblast-like morphology with compressed, spindle-shaped lacunae (Tretjakoff, 1926; Kemp and Westrin, 1979). In contrast, cells and lacunae of the chondral 'body' zone, the region bordering the cartilage core, exhibit a rounded shape similar to that of the chondrocytes in the cartilage core (Tretjakoff, 1926; Kemp and Westrin, 1979; Clement, 1992; Dean et al., 2010). Young tesserae not yet in contact with the fibrous perichondrium possess only rounded, 'body' zone-type cells, giving them the appearance of lacking a 'cap'. Furthermore, whereas the chondral margin of the body zone (the edge bordering the unmineralized cartilage) exhibits a more globular calcification, the perichondral edge of the cap zone is rough with needle-like crystals (Orvig, 1951; Kemp and Westrin, 1979; Seidel et al., 2016), a feature typically observed in mineralizing Coll I based tissues (Boyde and Hobdell, 1968).
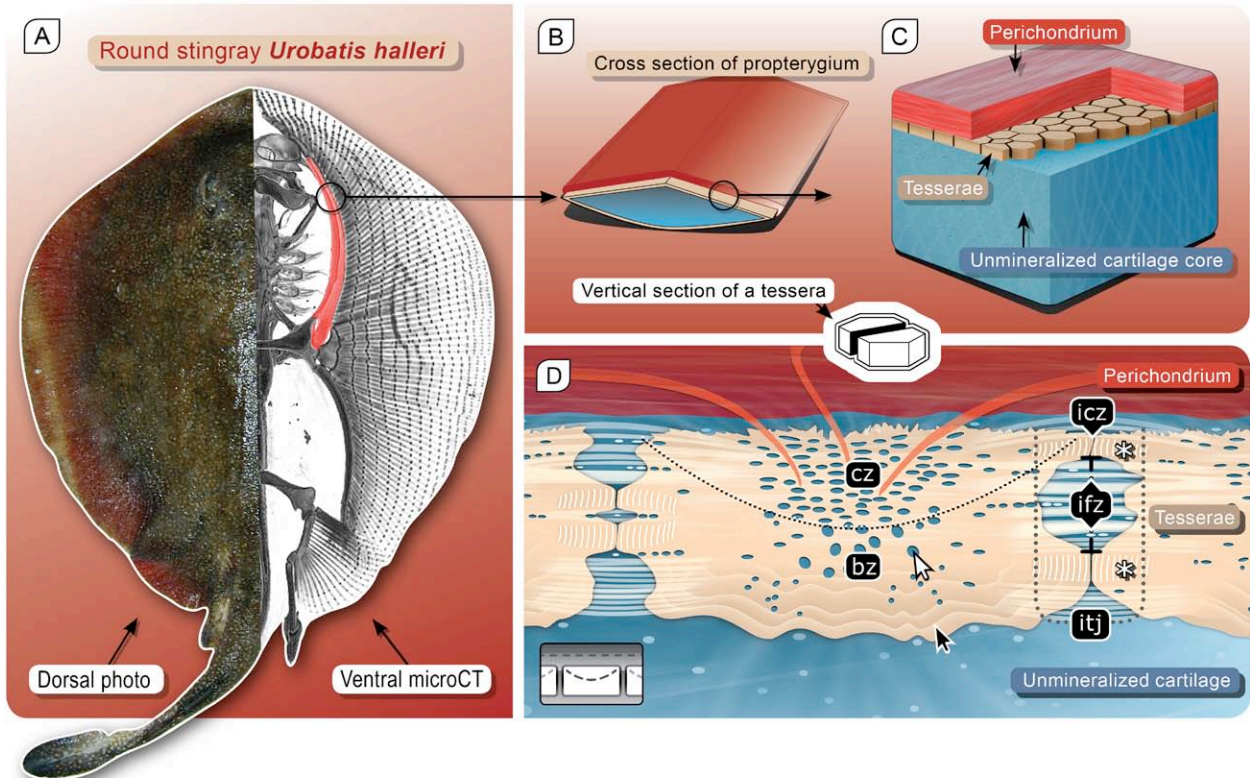
Fig. 1 Overview – Tessellated cartilage of the round stingray *Urobatis halleri*.
(A) Photograph (left) of a round stingray *Urobatis halleri* and microCT image (right) of the mineralized endoskeleton, with the propterygium (used here as a representative skeletal element) in the anterior part of the ray highlighted in red. (B) Schematic cross section of the propterygium and (C) generalized overview of the tissue architecture of elasmobranch tessellated, calcified cartilage, comprised of the unmineralized cartilage core covered in a mineralized crust consisting of small tiles (tesserae), wrapped in an outer fibrous perichondrium. In this study, all tesserae are sectioned and visualized in the vertical plane as shown by the stylized white icon. (D) Beneath the perichondrium (P) the mineralized tesserae are arranged in an array of abutting tiles, separated from one another by intertesseral joints (itj). The morphologies of intertesseral joints are complex, comprised of varying portions of fibrous zones (ifz) and intertesseral contact zones (icz) where tesserae are in direct contact and develop laminar features of high-mineralization (spokes laminae = asterisks) in the tesseral margin. Tesserae are composed of an upper 'perichondral' cap zone (cz) and a lower 'chondral' body zone (bz). Liesegang lines of periodic mineral density variation represent successive accretion of mineral to the body zone and lateral, non-spoke margins (black arrow). Living cells are housed in a network of lacunar spaces connected via small passages (canaliculi) filled with unmineralized cartilage (white arrow). The skeletal core is composed of uncalcified cartilage (UC). The icon in the lower left corner is used in all figures indicating the tissue region studied (e.g. perichondrium, cap/body zone, intertesseral joints or the unmineralized cartilage core).

These lines of evidence suggest that tesserae may exhibit different fibrous compositions at different developmental stages, dependent on interaction with the perichondrium, and that Enault et al.'s (2015) results either captured an incomplete view of the development of tesserae or cannot be standardized for all elasmobranch species. The differences in the ultrastructure of mineralization and morphology of cell lacunae between cap and body zones suggest that both the perichondrium and the hyaline-like cartilage may play a role in structuring the mineralizing matrix at tesseral edges (Fig. 1;

Table 1: Comparison of the findings of previous studies investigating the collagenous composition (Coll I and Coll II columns) of elasmobranch skeletal materials, using a variety of methods, species and sampling sites (tissues). Most studies did not investigate the collagenous composition of tesserae specifically, instead using either homogenized tissues (i.e. mixing tesserae and other mineralized and non-mineralized tissues), or young pre-tessellate animals (i.e. having only unmineralized cartilage). Note that elasmobranch vertebrae are comprised of two types of mineralized tissue: tessellated cartilage in the neural arches and so-called areolar mineralized cartilage in the centra; results from both Rama and Chandrakasan (1984) and Peignoux-Deville et al. (1982), therefore, cannot be interpreted with regard to the collagenous composition of tesserae. Egerbacher et al. (2006) and Enault et al. (2015) both investigated tesserae from a catshark (*S. canicula*), however reported contradictory results. Tissue abbreviations indicate where a collagen was found in specific tissues: BZ = tesseral body zone; CZ = tesseral cap zone; LS = matrix in lacunar spaces; PC = perichondrium; SF = Sharpey's fibers; SP = spokes; SU = supratesseral layer; T = tesserae; UC = uncalcified cartilage. Species investigated: *Carcharias (Rhizoprionodon) acutus, Cephaloscyllium ventriosum, Raja (Okamejei) kenojei, Squalus acanthias, Scyliorhinus canicula, Urobatis halleri.*

SOURCE	SPECIES	TISSUE INVESTIGATED	COLL I	COLL II	NOTES
Mizuta et al., 2003	skate (*R. kenojei*)	pectoral fin cartilage	+	+	tissues were homogenized
Sivakumar & Chandrakasan, 1998	shark (*C. acutus*)	"cartilage tissue"	+		tissues were homogenized
Rama & Chandrakasan, 1984	shark (*C. acutus*)	"vertebral cartilage"	+	+	homogenized Coll I:II ratio 1:2
Peignoux-Deville et al., 1982	shark (*S. canicula*)	neural arch	+	+	using TEM: Coll II in "calcified cartilage"
Eames et al., 2007	shark (*C. ventriosum*)	neural arch	+ (PC)	+ (PC)	young animal (pre-tesserae)
Eames et al., 2007	shark (*C. ventriosum*)	lower jaw		+ (UC)	young animal (pre-tesserae)
Conrad et al., 1981	shark (*S. acanthias*)	scleral cartilage	+ (PC)	+ (UC)	tissue naturally non-tessellated
Egerbacher et al. 2006	shark (*S. canicula*)	"entire endoskeleton"	+ (T+PC)	+ (UC)	tissue was ruptured in Coll I staining
Enault et al. 2015	shark (*S. canicula*)	cartilage, tesserae and perichondrium	+ (PC)	+ (T+UC)	young animal (early tesserae)
this study	stingray (*U. halleri*)	cartilage, tesserae and perichondrium from propterygia	+ (PC, SF, SU, CZ, upper joint fibers)	+ (SU, LS, BZ, UC, SP, joint fibers)	Coll X: SU, CH, (SP); unidentified lower joint fibers

Seidel et al., 2016). Additionally, the repetitive patterns in mineral density variation seen in tesserae (Fig. 1D, black arrow)—concentric, wave-like Liesegang bands (e.g. Peignoux-Deville et al., 1982; Takagi et al., 1984; Bordat, 1988; Clement, 1992; Seidel et al., 2016) or laminate spokes reinforcing

intertesseral joints (Seidel et al., 2016)— suggest that the underlying fibrous architecture of tesseral mineralized tissue is far more complex than currently appreciated.

Here, we investigate the collagenous composition of adult *U. halleri* tesserae and their associated surrounding tissues, including the fibrous material in intertesseral joints, perichondrium and unmineralized cartilage, using light microscopy and histological staining, electron microscopy, and immunohistochemistry. By employing the same study species, nomenclature and sectioning protocols used in Seidel et al.'s (2016) investigation of tesserae development and mineralized ultrastructure, we work within a stringent anatomical framework that allows characterization of the interaction of mineralized and unmineralized tissues in tesserae. The results clarify how the different regions within tesserae (cap and body zones) are patterned and developed, while illuminating possible homologies in mineralization processes between elasmobranch cartilage and the more widely investigated mammalian cartilage.

5.2 MATERIALS & METHODS

Skeletal samples of the anterior shoulder girdle (propterygia) were collected from a deceased adult male round stingray (*Urobatis halleri*, 20.0 cm disc width, DW), donated from another study (Lyons et al., 2014), caught by hook and line from Seal Beach, California in July 2014. Following dissection, the propterygial cartilages were immediately fixed with 4% PFA in phosphate-buffered saline (PBS, 0.1 M), stored for 6 h in this solution at room temperature, and then rinsed in PBS. The samples were stored in PBS (0.1 M, 0.05% sodium azide) and shipped to the Medical University of Innsbruck, Austria, where they were further processed for light microscopy (LM), transmission electron microscopy (TEM), and immunohistochemistry (IHC). The propterygia were examined because their shapes offer comparatively large regions of flat skeletal surface, comprised of tesserae with simple rectangular cross-sections.

The majority of our data and figures are from this single *U. halleri* specimen. However, several jaw, hyomandibular and shoulder girdle skeletal elements from other adult *U. halleri* were prepared and observed prior to this one in order to develop our specimen preparation protocols (e.g. specimens that had been frozen prior to fixation and embedding resulted in poor cellular detail and weaker immunostaining). Observations of those preliminary specimens (i.e. the localization of different collagens) support the observations reported here.

5.2.1 Tissue preparation for light microscopy (LM)

In order to corroborate our TEM and IHC identifications of different tissues, we stained sections with several histological stains for collagens and matrix components (e.g. haematoxylin and eosin, Masson's trichrome and AZAN bichrome). This allowed for comparison with mammalian cartilage

and bone, our control samples (Table 2), and previously published histological data for elasmobranch cartilage (Table 1).

Samples were decalcified with ethylenediaminetetraacetic acid (EDTA) for one week, dehydrated with a graded isopropanol and xylene series, and embedded in paraffin using a routine histological infiltration processor (Miles Scientific Inc., Naperville, IL, USA). Serial cross sections (7 μm) were made on a HM 355 S microtome (Microm, Walldorf, Germany), and three sections per slide mounted on Super-Frost®Plus slides. Sections were stained with one of the following: (1) Haematoxylin and eosin (HE) (Shandon Varistain 24-4, Histocom Vienna, Austria) are used to discern between basic components (e.g. cytoplasm, connective tissue, decalcified bone) which stain shades of red, and acidic components (e.g. nucleic acid, the territorial matrix between cells in unmineralized cartilage) which stain blue or violet and pinkish due to metachromasia (Mulisch and Welsch, 2015). (2) Toluidine blue (TB) (1% toluidine blue, 1% borax in distilled water for 1 min at room temperature), also a metachromatic stain, was also used to detect acidic tissue components (e.g. cartilage glycosaminoglycans stain purple; Geyer and Linss, 1978; Melrose et al., 2004; Sridharan and Shankar, 2012). (3) For collagen staining, AZAN bichrome (with azocarmine and aniline blue) and (4) Masson's trichrome (#3459, Carl Roth, Karlsruhe, Germany) were used. AZAN bichrome stains nuclei and cytoplasm red and collagens blue (Humason, 1962; Mulisch and Welsch, 2015; G. Klima, personal communication). Masson's trichrome stain is used to distinguish muscle tissue (red) from connective tissue (green), providing some discrimination also between Coll I-based tissues (darker green) and Coll II-based tissues (pale green) (Mulisch and Welsch, 2015; G. Klima, personal communication). Additionally, (5) orcein (# 107100 Merck, Darmstadt, Germany) staining was performed to detect elastin-containing tissues. All stainings were performed according to the manufacturer's protocol.

5.2.2 Tissue preparation for transmission electron microscopy (TEM)

Samples were postfixed in 1% osmium tetroxide in distilled water for 24 h at 4 °C. They were rinsed, decalcified as described above, dehydrated through a graded ethanol series and embedded in EPON resin. Semithin cross sections (1.5 μm) were cut on a Reichert Ultracut S microtome (Leica Microsystem, Wetzlar, Germany) with a histo-jumbo-diamond knife (Diatome, Biel, Switzerland) and stained with TB for 20 s at 60 °C. Ultrathin cross sections (90 nm) were cut on the same microtome with an ultra-diamond knife, mounted on dioxan-formvar coated slot-grids (#G2500C, Christine Gröpl, Elektronenmikroskopie, Tulln, Austria) and stained with uranyl acetate and lead citrate (Leica Ultrostainer, Leica Microsystem, Wetzlar, Germany). The ultrathin sections were examined with a Philips CM 120 transmission electron microscope at 80 kV (FEI, Eindhoven, Netherlands) equipped with a MORADA digital camera (Olympus SIS, Münster, Germany), using Olympus TEM Imaging Platform software.

5.2.3   Scanning electron microscopy (SEM)

Decalcified sections of tessellated cartilage were placed in a jar containing iodine crystals; evaporation of iodine crystals at room temperature created an iodine coating for increased soft tissue contrast in SEM (Boyde et al., 2014). Samples were examined in backscatter mode (backscatter SEM) using a Field Emission Environmental Scanning Electron Microscope (FE-ESEM, FEI Quanta 600F) in environmental mode (i.e. at low vacuum) with acceleration voltage of 10 kV.

5.2.4   Immunohistochemistry (IHC)

Vertebrate collagens are known to be highly conserved in their structure (Sivakumar and Chandrakasan, 1998; Boot-Handford and Tuckwell, 2003), and both Coll I and II, found in bone and calcified cartilage, respectively, have been identified in elasmobranch skeletal tissue in multiple studies (e.g. Conrad et al., 1981; Sivakumar and Chandrakasan, 1998; Mizuta et al., 2003). Rabbit antibodies for Coll I and II have been shown to have affinities to both chicken and elasmobranch collagens (Conrad et al., 1981; Sivakumar and Chandrakasan, 1998; Blumer et al., 2005) and were used in this study. IHC was performed on paraffin sections with the following antibodies (AB): a rabbit antibody directed against Coll I (1:100 in AB diluents; LF-68 donated by Prof. L. Fisher, National Institutes of Health, Bethesda MD, USA), a rabbit antibody against Coll II (1:200 in AB diluents; #CL50211AP, Cedarlane, Ontario, Canada), and a rabbit antibody against Coll X (1:100 in AB diluents; #ab58632, Abcam, Cambridge, UK).

Sections were deparaffinized and rinsed in PBS, and for Coll II and X collagen staining digested with protease (1 min for Coll X collagen and up to 10 min for Coll II collagen; protease 1, #5266688001, Ventana, Strasbourg, France). Subsequently endogenous peroxidase activity was blocked with 0.5% H_2O_2 in 30% methanol for 20 min in the dark. Sections were then incubated overnight at 4 °C in the primary antibody, followed by saturation of unspecific sites with 10% normal goat serum (NGS) for 20 min, and a 4-h incubation with a secondary antibody (goat anti-rabbit IgG/HRP-conjugated 1:1000 in antibody diluents) (#P0448, DakoCytomation, Glostrup, Denmark) at room temperature. The antigen–antibody complex was made visible by 0.05% 3,3-diaminobenzidine (DAB), and 0.01% hydrogen peroxide (H_2O_2) in distilled water (10–15 min in the dark). Sections were counterstained with haematoxylin. Immunohistochemical identification for Coll I and II were verified by TEM investigations of fibril morphology of the same regions in adjacent serial sections.

Negative controls were obtained by substituting the primary antibodies with antibody diluents (# 05261899001, Ventana, Strasbourg, France). They yielded no labelling. Positive controls for cartilage, collagen and bone were performed on sections of the developing femur of mouse (*Mus musculus*, C57Bl6) and chicken (*Gallus gallus*). In both species' sections, Coll I was present in the bone, the periosteum and the perichondrium. Coll II was present in the cartilage and Coll X around the hypertrophic chondrocytes of the growth plate. Here we show only data from mouse (see Section 3).

The paraffin and semithin resin sections were examined with a Zeiss Axioplan 2 (Zeiss, Oberkochen, Germany) and photographed as colour images, using a Zeiss AxioCam HR and AxioVision 4.1. software.

5.3 RESULTS

The investigated propterygia of adult *U. halleri* exhibited the morphology and tissue architecture previously described for tessellated cartilage (Kemp and Westrin, 1979; Dean et al., 2009; Omelon et al., 2014, Seidel et al., 2016): an uncalcified cartilage core sheathed in a layer of tesserae and an outer wrapping of fibrous perichondral tissue (Fig. 1). The two portions of the tesserae, the 'cap' and 'body' zones (sensu Kemp and Westrin, 1979) were readily visible due to their differential histological staining (see below) and the different shapes of cell lacunae in each region (Fig. 1D, 2A, 3A; Seidel et al., 2016). The cell lacunae in the cap zone were rather flat, with their long axes parallel to the skeletal surface. In contrast, body zone lacunar spaces and cells were predominantly round, similar in form to chondrocytes in the uncalcified cartilage core. The body zone was always larger than the cap zone, encompassing the central, lateral and chondral regions of tesserae. The cap and body zones and the intertesseral joints exhibited distinct collagen compositions.

The results are described in detail below according to the anatomical region in tesserae, with the order of explanation progressing largely in the perichondral to chondral direction. For comparative purposes, histological staining, immunohistochemistry and TEM results for specific regions of tessellated cartilage and for our mouse control samples are also summarized in Table 2.

5.3.1 Perichondrium and Sharpey's fibers

The perichondrium exhibited a strong IHC labelling for Coll I (Fig. 2A, haematoxylin counterstaining). This was supported by TEM images, showing a rich network of Coll I fibrils (each ~25–50 nm in diameter) organized into bundles (~5–15 μm). In skeletal cross-sections (i.e. tesserae vertical sections, Fig. 1B–D), the fibril bundles appeared to be arrayed in a variety of orientations, but typically largely parallel to the tesseral mat, resulting in a woven appearance of Coll I fibril bundles in some sections (Fig. 2B–D). In controls (mouse), the perichondrium also strongly stained for Coll I; however, Coll I fibril bundles were smaller, with their fibrils more irregularly arranged (i.e. not in obvious bundles). Furthermore, fibroblasts were more numerous in mouse perichondrium compared to those in *U. halleri* perichondrium (Fig. 2E, F). In some sections, larger perichondrial fibril bundles (>20 μm in diameter) inserted at steep, almost perpendicular angles into the cap zones of tesserae (Fig. 3A–G). In keeping with previous authors (Kemp and Westrin, 1979; Peignoux-Deville et al., 1982; Clement,

Table 2: Staining explanations. All histology staining and immunohistochemistry results for specific regions of tessellated cartilage (and our mouse control samples) are summarized here, according to their order of description in "Section 3". Legend: "+" = positive immunostaining; "−" = negative immunostaining; "*" = visible in TEM only, not immunohistochemistry; "?" = suggestion of positive staining, further analysis needed. For antibodies and histology staining specifics see "Section 2".

Urobatis halleri **tessellated cartilage:**

Sampling site	Immunohistochemistry				Histological stains				
	Coll I	Coll II	Coll X	TEM	HE	Masson's	AZAN	Toluidine (resin)	Toluidine (parafin)
Perichondrium	+ Fig. 2A,3B-E	- Fig. 7A,9A	- Fig. 9C	Fig. 2C,D	red Fig. 3A,6A	green Fig. 3F	blue Fig. 3G	blue Fig. 2B	none Fig. 9B
Sharpey's fibers	+ ; CZ: - Fig. 3B-E	- Fig. 9A	- 	Fig. 4A-B	purplish-red Fig. 3A,6A	green; CZ: none Fig. 3F	blue; CZ: red Fig.3G	blue Fig. 4A inset	pale blue Fig. 9B
Tesserae 'cap'	(+* Fig. 2A,3B-E,10D	- Fig. 5G-H,10G	- Fig. 9C	Fig. 4A-E,5A-B	purplish-red Fig. 3A,6A	orange-green Fig. 3F	red Fig. 3G	blue Fig. 2B,6B	pale blue Fig. 5I,9B
Tesserae 'body'	- Fig. 2A,10D	+ Fig. 5G-H,10G	- Fig. 9C	Fig. 5E-F,6E-F	purple Fig. 6A,7F	orange-green	red	blue Fig. 6B	pale blue/purple swath Fig. 5I,7E,9B
Tesserae 'spokes'	-	+? Fig. 6C,9A	+? Fig. 9C	Fig. 6D	purple? Fig. 6A,10B	green?	blue?	purple Fig. 6B,10A	purple Fig. 9B
Tesserae 'lacunae' (around IT cells)	- Fig. 3B-E	+ Fig. 5G-H,10G	- Fig. 9C	Fig. 8	pink Fig.3A,7F	pale green Fig. 3F	blue Fig.3G	pale blue Fig. 2B,6B	purple Fig. 5I,9B
Subtesseral uncalcified cartilage	- Fig. 2A	+ Fig. 7A,10G	- (cells?) Fig. 9C	Fig. 6F,7B,10J	pale pink Fig. 6A,7F,10C	pale green	blue	pale blue	pale purple, cells w/ halo Fig. 7E,9B
Supratesseral uncalcified cartilage	- Fig. 3B-E	+ Fig. 7A,9A,10G	+ Fig. 9C	Fig. 4A-B,D	pinkish-red Fig. 3A,6A	pale green Fig. 3F	blue Fig.3G	pale blue Fig. 2B	purple Fig. 9B
Intertesseral joints upper portion	(+* Fig. 10D	+ Fig. 7A,10G	*(cells?)* Fig. 9C	Fig. 10F,H	pink Fig. 6A,10B	pale green	blue	pale blue Fig. 6B,10A	pale purple, cells w/ halo Fig. 9B
Intertesseral joints lower portion	- Fig. 2A,10D	- Fig. 7A,10G	*(cells?)* Fig. 9C	Fig. 10I	pink Fig. 6A,10C	none or pale green	none or pale blue	pale blue Fig. 6B,10A	pale purple, cells w/ halo Fig. 9B

Mouse control samples:

	Coll I	Coll II	Coll X	TEM	HE	Masson's	AZAN	Toluidine blue (parafin)
Bone	+	-	-	Fig.5C-D	red	dark green	blue	none
Osteoid	+	-	-		pink	dark green	blue	none
PC	+ / Fig. 2E	-	-	Fig. 2F	red	dark green	blue	none
Uncalc. cartilage	- / Fig. 2E	+	-	Fig. 7D	pinkish-red	pale green	blue	purple
Calc. cartilage	-	+	+		pinkish-red	pale green	blue	purple

1992; Summers, 2000), we will refer to these bundles as Sharpey's fibers since they are similar in size, composition and ultrastructure to the Sharpey's fibers that connect non-mineralized Coll I-based tissues (e.g. periosteum) to mineralized Coll I-based dental or skeletal tissues (e.g. bone) (Sharpey, 1848; Kölliker, 1864; Schäfer, 1878; Stern, 1964; Boyde and Jones, 1968; Jones and Boyde, 1974).

In *U. halleri*, Sharpey's fibers displayed a strong immunolabelling for Coll I outside of the cap zone, whereas within cap zone tissue they remained unstained (Fig. 3B–E). A similar abrupt staining transition was observed in Masson's trichrome and AZAN bichrome stains, which otherwise stained the perichondrium for collagen (Table 2; Fig. 3F, G). Although these staining observations suggested that Sharpey's fibers terminate at the surface of tesserae, our TEM data confirmed that Coll I fibrils —either single fibrils or those forming Sharpey's bundles— extended uninterrupted from the perichondrium into the cap zone. Upon entering the mineralized tissue of the cap zone, Coll I fibrils became
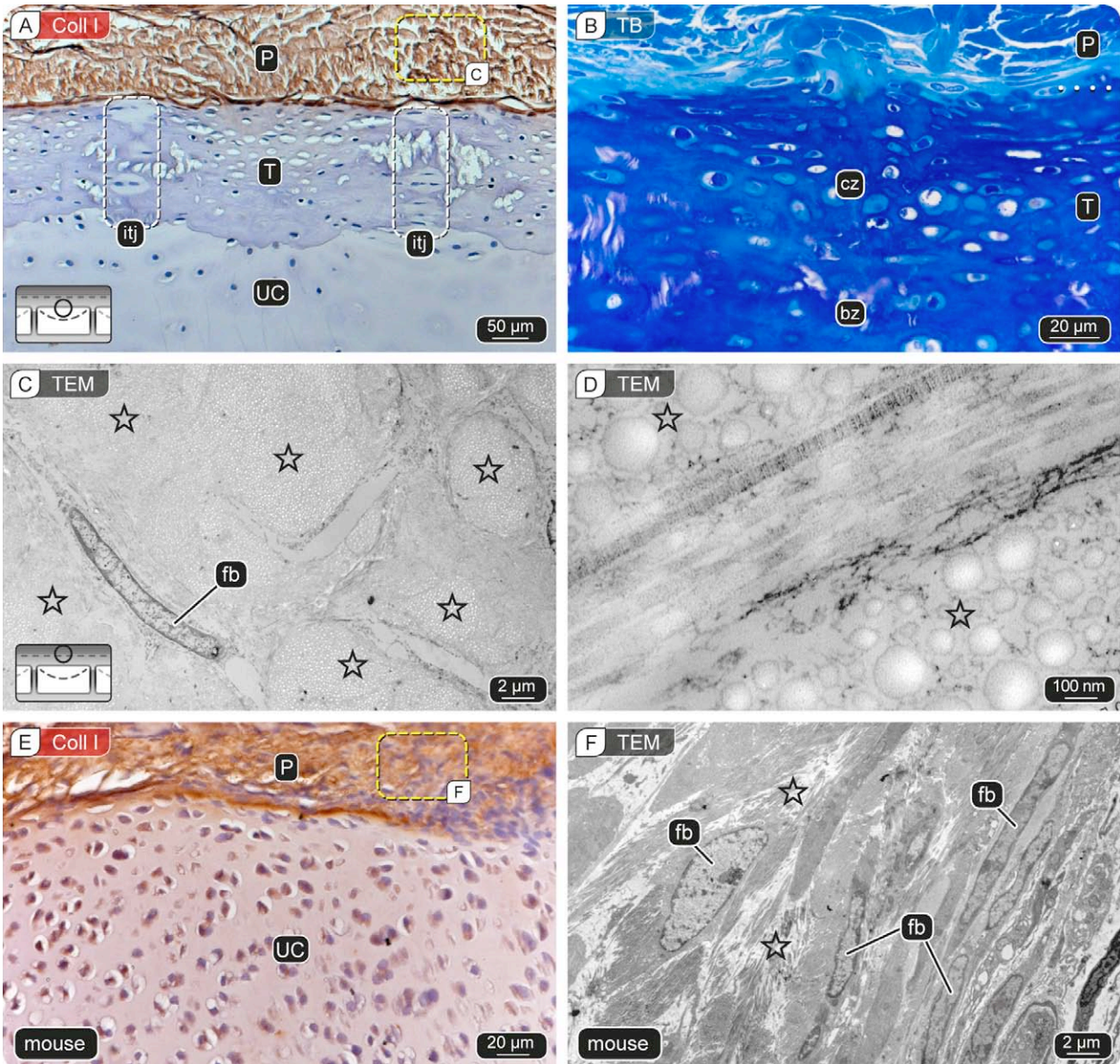
Fig. 2 IHC (Coll I), TB stain and TEM imaging of the fibrous perichondrium.

(A) Vertical sections of the perichondrium and tessellated cartilage of *U. halleri* immunohistochemically stained (IHC) for Coll I. Coll I is exclusively located in the perichondrium (P). No staining is observed in the cap and body zone of the tesserae (T), the intertesseral joint (itj) and the uncalcified cartilage core (UC). (B) Toluidine Blue counterstaining of the perichondrium (P) and a tessera (T), with cap (cz) and body zone (bz). (C) See inset in A): Transmission electron microscopy (TEM) image of cross-sectioned Coll I fibril bundles (stars) and fibroblast (fb) in the perichondrium. (D) Higher magnification of the Coll I fibril network in the perichondrium showing the banded nature of longitudinal sectioned fibrils intermingling fibril bundles of different orientation cut in cross section (asterisks). (E) IHC staining of a mouse control sample showing the perichondrium heavily labelled with Coll I antibodies, whereas the uncalcified cartilage is not stained. (F) See inset in E): TEM image of the perichondrium, showing fibroblasts (fb) are interspersed in a dense collagen (Coll I) fibril network (asterisks).
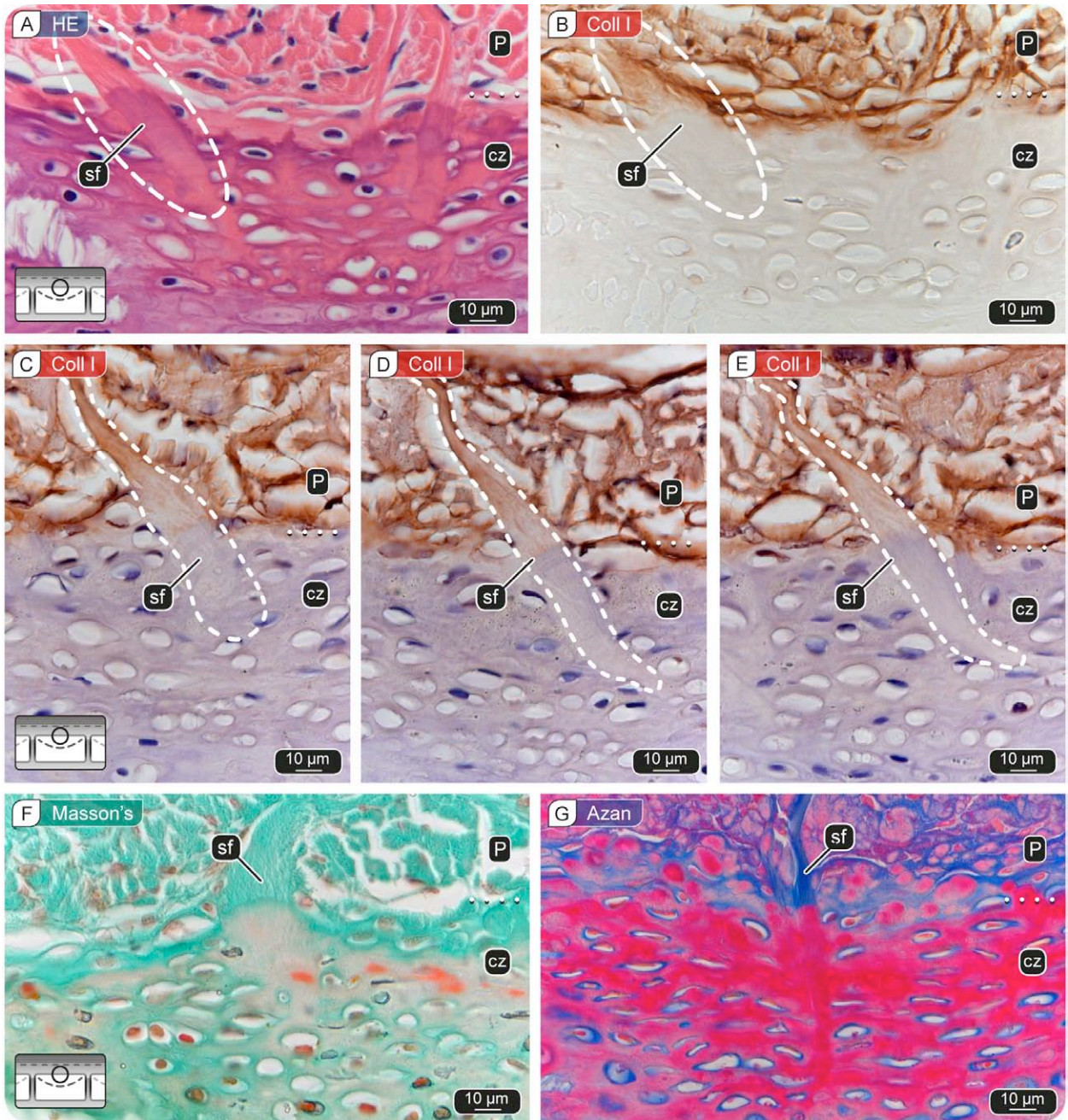
Fig. 3 IHC (Coll I) and histological staining (Masson's and AZAN) of the Sharpey's fibers.
Vertical sections of the transition region between the perichondrium and tesserae. (A) HE staining showing a thick Sharpey's fiber (sf) from the perichondrium (P) advancing deep into and ending in the cap zone (cz). (B) Coll I staining of an adjacent section, showing the same region and Sharpey's fiber (sf) entering the tessera's cap zone (cz). Both perichondrium (P) and the Sharpey's fiber are Coll I positive, however, the Sharpey's fiber staining was absent in the cap zone. The section is not counterstained. (C–E) Coll I IHC images of three consecutive sections through a Sharpey's fiber (sf), counterstained with haematoxylin. The dashed lines indicate the outline of the Sharpey's fiber. (F) Masson's trichrome, staining Coll I green (Perichondrium P), however, Sharpey's fibers (sf) did not stain in the cap zone (cz). (G) AZAN bichrome, staining Coll I as well as Coll II blue. A Sharpey's fiber (sf) in the perichondrium (P) stained blue, however, the staining changes abruptly to red at the perichondrium-tessera cap zone interface.

sheathed in an electron-dense layer, coating them for the remainder of their visible length inside the tessera (Fig. 4D, E).

5.3.2 Tesserae

As mentioned above, the cap zone of tesserae exhibited no staining for Coll I (Figs. 2A and 3B–E). TEM images showed that this region was composed of an electron-dense matrix with electron-translucent areas interspersed (Fig. 4). Although the electron density of the matrix made it difficult to recognize any structural pattern in TEM images, occasionally Coll I fibrils (distinguishable by their size and banding) could be seen coursing through the cap zone matrix (Figs. 4B, C and 5A, B), similar to the mineralized matrix in the bone control tissue (Fig. 5C, D). The cap zone remained unstained for Coll II, even after long protease treatment to expose the Coll II protein (see below). At the junction of the cap and body zones, the mineralized matrix was a mix of the two regions' ultrastructures, with cap zone Coll I fibrils interspersing sparsely with the Coll II-rich matrix of the body zone tissue (see below).

The ultrastructure of the demineralized tissue of the body zone was distinct from that of the cap zone. In particular, the body zone lacked Coll I fibrils and appeared in TEM images to be comprised of a Coll II-rich extracellular matrix, similar to that of the underlying unmineralized cartilage core (Fig. 5E, F). The body zone initially exhibited no Coll II immunostaining (Fig. 5G), however long treatments with proteases (~10 min) resulted in a positive Coll II immunostaining for the body zone in several tesserae (Fig. 5H).

Histologically, the cap and body zones were best differentiated with HE staining (with the cap zone staining purplish-red and the body zone purple, noted also previously by Kemp & Westrin 1979), and to some degree with TB-staining (Table 2). In contrast, the cap and body zones were indistinguishable with both Masson's and AZAN stains, with both tesseral zones staining orange-green in the former and staining red in the latter (Table 2). The Masson's staining of tesserae appeared to be similar to the pale green staining of the uncalcified cartilage core, but showed randomly distributed slightly orange tinged patches (Fig. 3F). These orange zones remained even after a prolonged differentiation time with Goldner solution II (phospho-wolframic acid, necessary to destain the connective tissue during the Masson's staining process) and were not seen in control samples from mouse calcified and uncalcified cartilage (data not shown).

Three large-scale structural patterns were often observed in the matrix of the body zone. Firstly, in many tesserae vertical sections, a strong TB stained swath often ran through the upper portion of tesseral body zones (the middle portion of the tessera, Fig. 5I), indicating local variation of acidophilic and basophilic matrix at the junction of cap and body zones. Occasionally, depending on sectioning plane, this swath extended uninterrupted from the lateral edge of a tessera through its center to the opposite lateral edge.
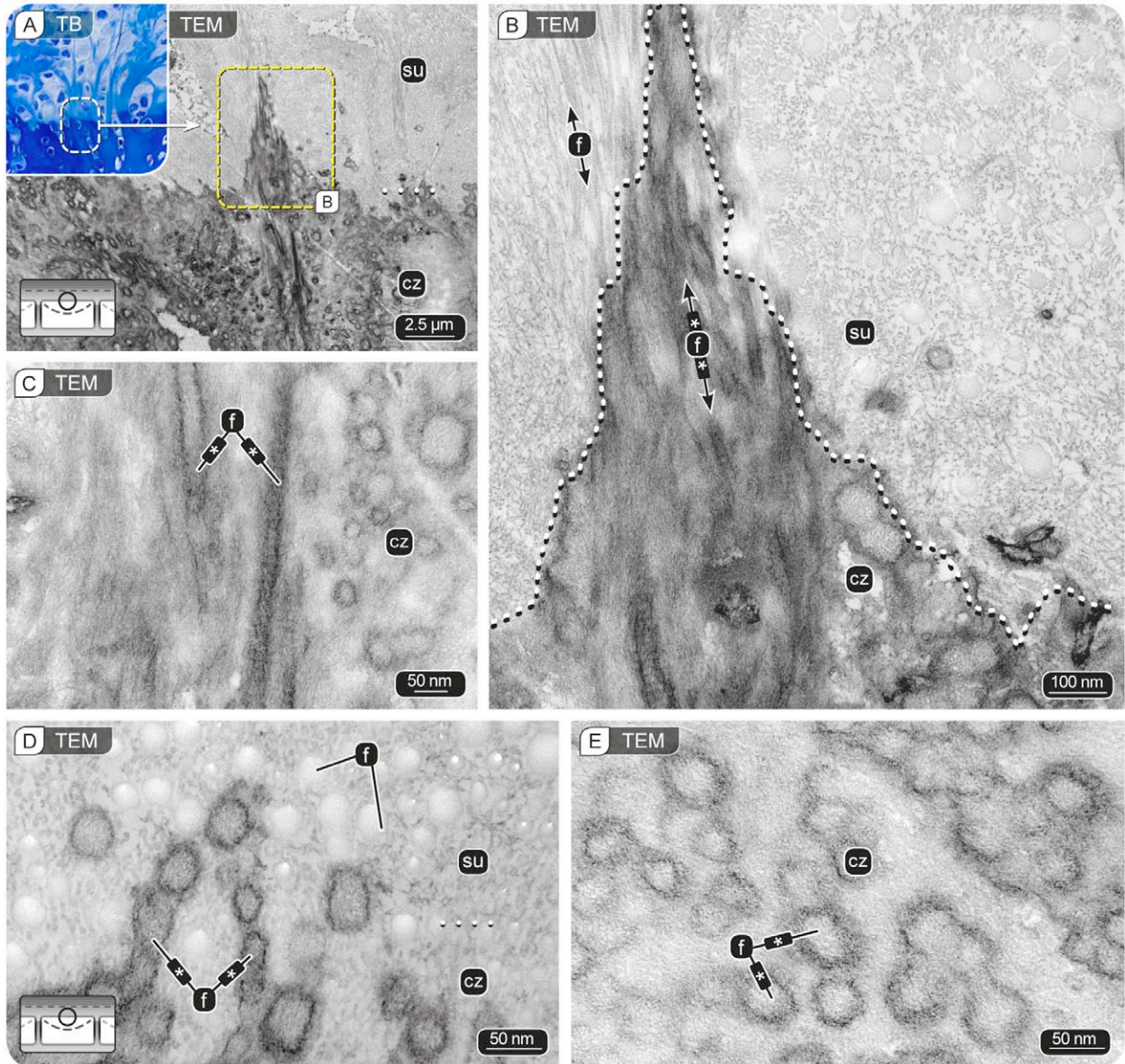
Fig. 4 TEM imaging of Sharpey's fibers and the cap zone.
Vertical sections of the transition region of the supratesseral uncalcified cartilage layer (su) and a tessera's cap zone (cz). (A) Overview (inset, light microscopy) and magnified view (TEM) of thick Sharpey's fibers inserting in a tessera's cap zone. (B) Higher magnification of the encircled area in (A), showing the supratesseral layer of uncalcified cartilage (su) with fibrils (f) embedded in a loose Coll II based matrix, and the Sharpey's fiber in the cap zone (cz) composed of numerous longitudinal-sectioned Coll I fibrils with cross-banded pattern (f). Some fibrils in the supratesseral layer and all fibrils sectioned in the cap zone exhibit a dark, electron dense hull in TEM images (asterisks in f-indicator, f*). (C) Higher magnification of the encircled area in (B), showing the banded pattern of the Coll I fibrils (f*) and the dark, electron dense hull surrounding them. (D–E) Cross-sectioned (Coll I) fibrils at the transition region between supratesseral layer and cap zone showing fibrils in the unmineralized supratesseral layer lack the dark, electron dense hull, whereas (E) collagen fibrils (f*) in the cap zone (cz) exhibit almost exclusively this electron dense layer.
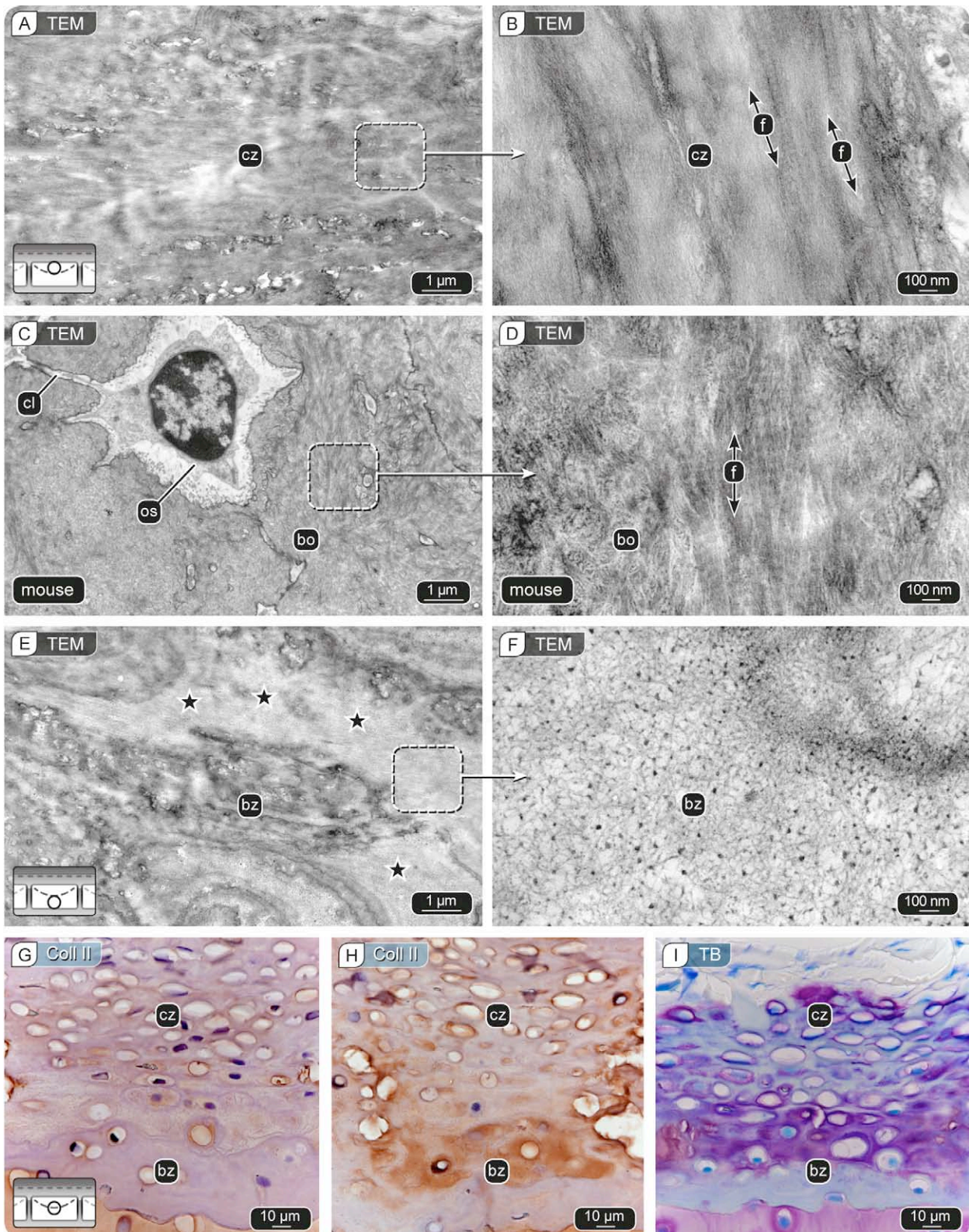
Fig. 5 TEM, IHC (Coll II) and TB stain of the cap and body zone.

(A-B) TEM section of a tessera's cap zone showing an electron dense fibrous tissue with banded Coll I fibrils (f). (C-D) TEM images of a mouse control sample showing an osteocyte (os) in its lacuna with canaliculi (cl) embedded in bone (bo), showing a Coll I fibril (f) based matrix similar to tesserae's cap zone. (E-F) TEM section of a tessera's body zone (bz) showing an amalgam of electron dense and loose matrix, with a Coll II based ground substance (stars). (G-H) The body zone initially exhibited no Coll II immunostaining, however, (H) long treatments with proteases

◀ (~10 min) revealed a positive Coll II immunostaining for the body zone in several tesserae. (I) TB staining of tesserae often resulted in swath of heavily stained tissue in the upper portion of tesseral body zones (the middle portion of the tessera), sometimes visible across the entire tessera.

A second pronounced structural feature in the body zone was associated with the laminated, high mineral density spokes that reinforce intertesseral joints (Fig. 1D asterisks; Seidel et al., 2016). In decalcified samples, spokes were visible as long swaths with an internal repetitive banding motif of alternating dense and loose fibrous material, extending from the tesseral edge at the intertesseral joint towards the tesseral center. This pattern echoes the alternating layers of higher and lower mineral density material (spokes laminae) that characterize spokes in mineralized sections (Seidel et al., 2016). Upon comparison of mineralized with non-demineralized sections, we find that the high mineral density laminae in spokes (bright bands in mineralized sections viewed in backscatter SEM) correspond to the loose fibrous, organic laminae in demineralized sections (high min/low org). In turn, low mineral density laminae correspond to the dense fibrous, organic laminae (low min/high org) (Fig. 6A–D). In demineralized HE and IHC stained sec tions (paraffin-embedded, cut with a steel knife, and examined using light microscopy), the loose fibrous laminae appeared nearly devoid of tissue (and therefore also exhibited little to no electron density in TEM sections; e.g. Fig. 6D). Laminae of the spokes also stained purple in TB sections (Fig. 6B), showed some evidence for Coll II immunostaining (Fig. 6C), sometimes a faint staining for Coll X (Fig. 9), but no evidence of Coll I immunostaining nor Coll I fibrils in TEM imaging (Table 2).

Body zone areas lacking spokes exhibited Liesegang lines (Fig. 1D, black arrow), visible as successive, concentric bands of different electron densities (~0.2–0.5 μm wide) (Fig. 6E, F). Liesegang lines have been described in tesserae from a variety of elasmobranch species in illustrations and histological stains (Bargmann, 1939; Schmidt, 1952; Kemp and Westrin, 1979; Peignoux-Deville et al., 1982; Takagi et al., 1984; Bordat, 1988). Recently, Seidel et al. (2016) demonstrated using backscatter SEM on mineralized sections, that Liesegang bands vary in their mineral densities. In the current study, we found that, as with spokes, Liesegang bands of lower electron density in our demineralized sections corresponded to the bands of high mineral density (low org/ high min) visible in BSE.

5.3.3 Sub- and supratesseral uncalcified cartilage

Immunohistochemistry of sections of the uncalcified cartilage core of the propterygia resulted in negative Coll I and strong positive Coll II staining (Fig. 7A). TEM images of the same region obtained from adjacent sections showed a loose, disorganized network of small (~10nm in diameter) unbanded collagen fibrils in an otherwise electron-translucent ground substance (Fig. 7B), exhibiting a similar ultrastructural appearance to control mammalian uncalcified cartilage samples (Fig. 7C, D).
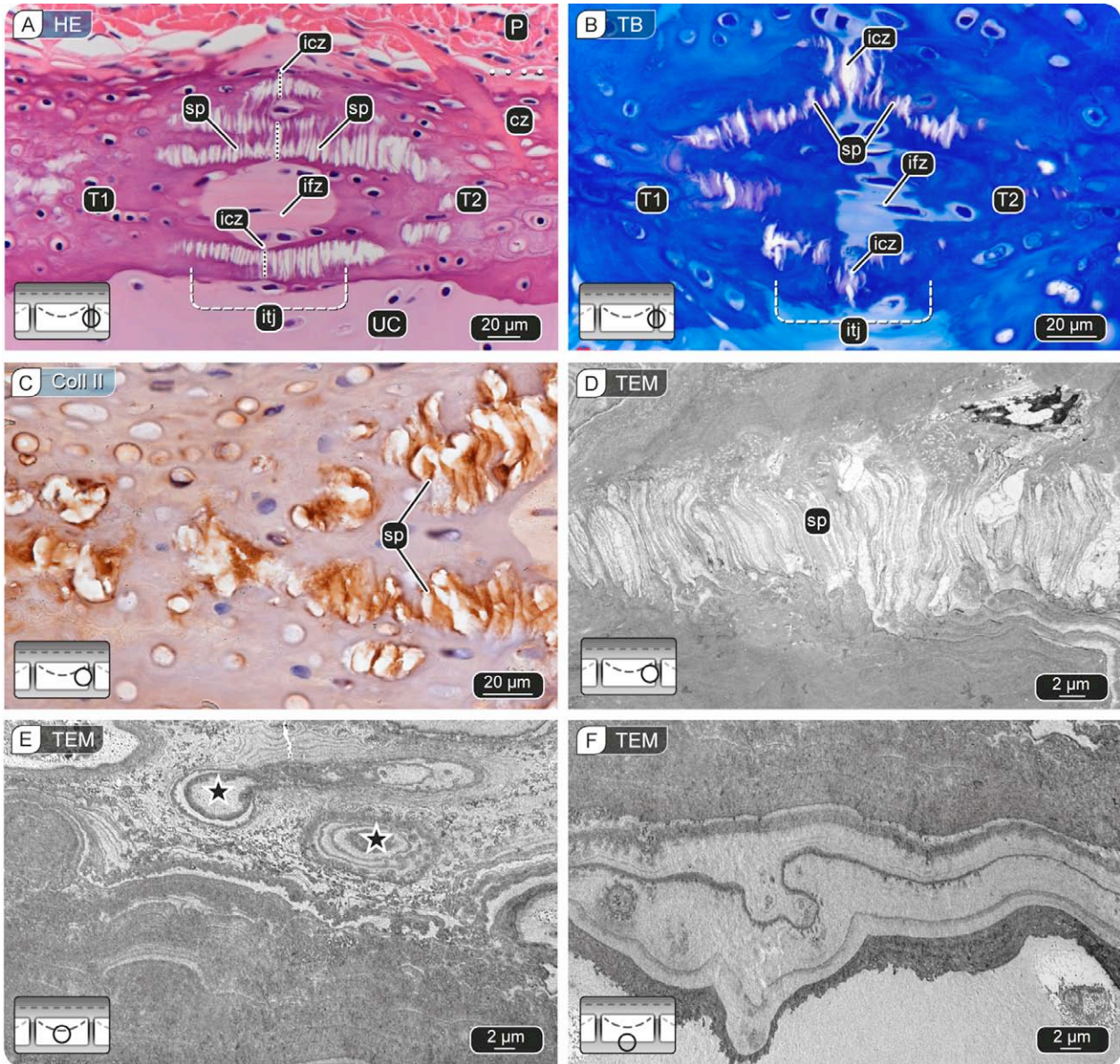
Fig. 6 Histological staining (TB and HE), IHC (Coll II) and TEM imaging of spokes and Liesegang lines.
(A) Demineralized HE stained sections of two adjacent tesserae (T1-2), showing the intertesseral joint (itj) comprised of intertesseral contact zones (icz) and intertesseral fibrous zone (ifz). These tesserae abut against one another on the perichondral and chondral side of the joint, leaving a gap of unmineralized cartilage (UC), comprised of fibrils, cells and extracellular matrix (ifz) in the middle region of the joint. Both (decalcified) tesserae exhibit spokes (sp), that are found strictly at the intertesseral contact zones and consist of repetitive patterns of vertical laminae (spokes laminae) parallel to the icz. (B) Section through an intertesseral joint showing spokes laminae stained purple in TB staining. (C) Zoomed in view on spokes laminae showing a positive immunostaining for Coll II. (D) TEM image showing the loose fibrous tissue bands of spokes are well preserved in resin embedded samples. Cells and lacunar spaces were never observed or could not be identified unambiguously in spokes. (E-F) Tissue bands of different electron densities (Liesegang lines) reflect local structural features. For example, (E) Liesegang lines radiate concentrically outward from cell lacunae walls (stars) until they meet Liesegang lines associated with other structural features. (F) Liesegang lines at tesseral edges often form long bands parallel to the chondral edge of a tessera.

In some histology sections, the uncalcified cartilage exhibited a network of narrow (<1 μm in diameter) but typically quite long (>1 mm) strand-like structures, radiating out from the chondral edge of tesserae deep into the cartilage core linking cell groups in series (Fig. 7E, F), similar to those described in early studies of elasmobranch cartilage (e.g. Hasse, 1879; Roth, 1911). The strand-like structures stained with both HE and TB stains (red in the former and deep purple in the latter) in elasmobranch, but also chicken and mouse unmineralized cartilage (data not shown), however, they were not observed in TEM sections. SEM imaging of iodine vapor-coated decalcified sections (7 μm thickness; Boyde et al., 2014) also revealed the strand-like structures at the chondral edge of tesserae, arguing that these are real features and not artifacts (Fig. 7G).

Chondrocytes in the subtesseral uncalcified cartilage core were typically rounded ellipses in cross-section in clusters of two to four cells. Each cell was surrounded by a purple metachromatic halo when stained with toluidine blue (TB) (Fig. 7E). Neither hypertrophic cells nor positive Coll X immunostaining were observed in the subtesseral uncalcified cartilage core. However, chondrocytes in the cartilage near the mineralization front showed some faint Coll X cytoplasmatic staining (see below). Chondrocytes at the chondral edge of tesserae were partially enclosed by calcified cartilage, but still surrounded by unmineralized matrix continuous with the hyaline-like cartilage core (Fig. 8A). Deeper into tesserae, away from the chondral margin, cells were completely encompassed by calcified tissue, yet always maintained a "pericellular envelope" (Kemp and Westrin, 1979) of uncalcified cartilage, occupying the ~1–2μm gap between the cell and the walls of its lacuna (Fig. 8B, C). The unmineralized pericellular cartilage stained similarly to the uncalcified cartilage core with all histological stains. There was no visible difference in the ultrastructure of the pericellular uncalcified cartilage in the cap or body zone, both exhibited a Coll II-rich matrix (Fig. 8B, C insets). The walls of lacunae were fringed by an electron-dense layer that was more pronounced in the body zone compared to that in the cap zone (Fig. 8B, C). In some sections, canaliculi —short passages filled with uncalcified cartilage, forming a continuous network through tesserae— were visible linking adjacent lacunae (Fig. 8B; Ørvig, 1951; Dean et al., 2010).

In many cross sections of propterygia from *U. halleri*, we observed a thin layer (~10 μm thick) of unmineralized cartilage between the perichondrium and tesseral cap. In order to distinguish it from the 'subtesseral' uncalcified cartilage core, we termed this thin layer 'supratesseral uncalcified cartilage'. This layer extended along the tops of tesserae, dipping also into the upper portions of intertesseral joints (see below). Coll I fibrils and fibril bundles from the perichondrium (e.g. Sharpey's fibers, see above) passed through the supratesseral layer to insert into the cap zone of tesserae (Figs. 3 and 9A, B). The ultrastructure of the ground substance of the 'supratesseral uncalcified cartilage' was similar to that of the unmineralized cartilage core, with both IHC and TEM imaging indicating a Coll II based matrix (Fig. 4B and 9A). Masson's and AZAN staining resulted in similar results for supra- and
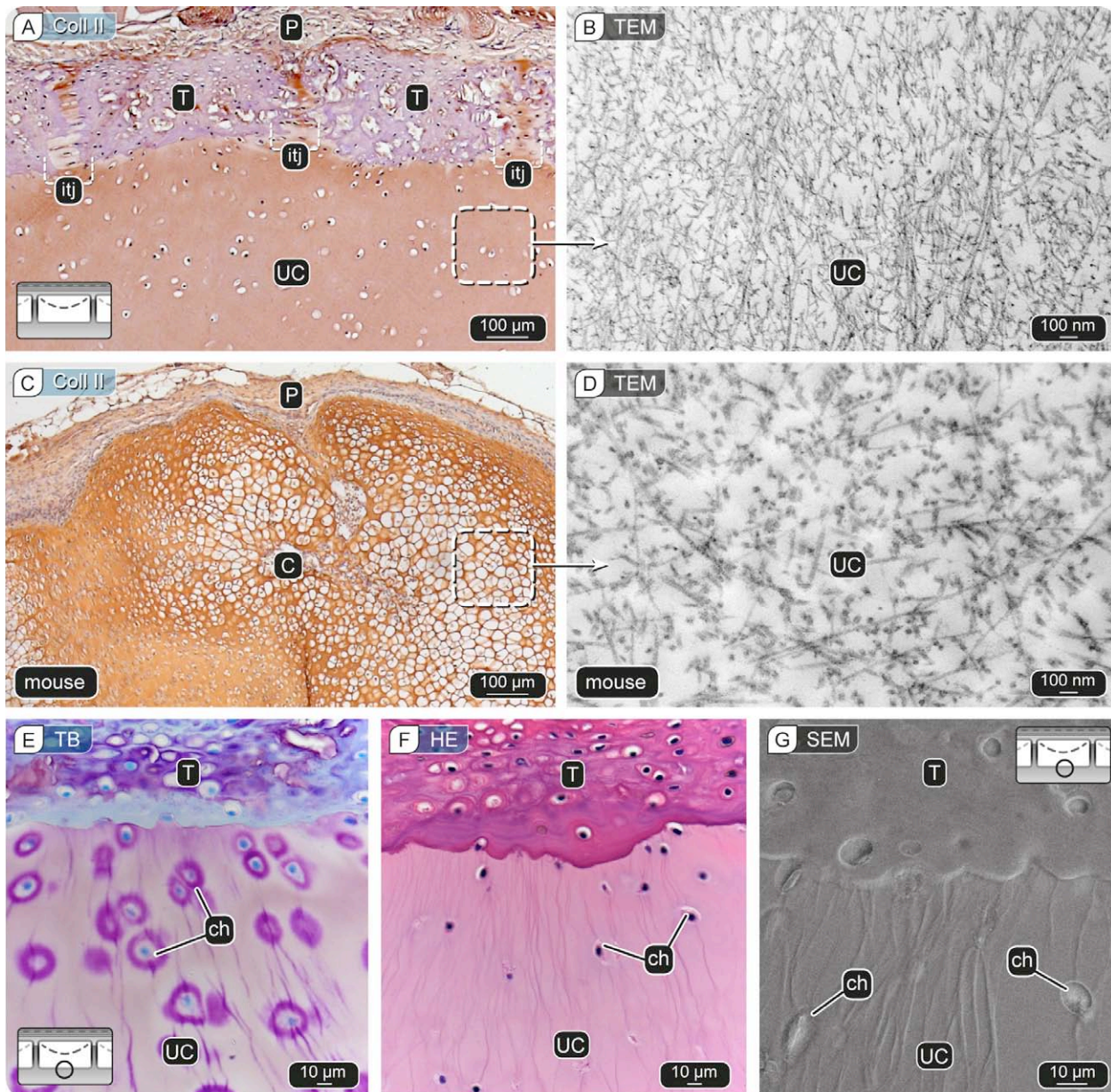
Fig. 7 IHC (Coll II), Electron microscopy (TEM and SEM), and Histological staining (TB and HE) of the unmineralized cartilage core. (A-B) The unmineralized cartilage core (UC) showed a positive immunostaining for Coll II, which was supported by B) TEM imaging showing a disorganized network of collagen type-II fibrils interspersing the otherwise electron-translucent extracellular matrix. (C-D) Control samples of mammalian (mouse) uncalcified cartilage (C), with TEM images showing a comparatively less dense Coll II network than in the ray samples. (E) TB histology image of the unmineralized cartilage near the chondral margin of tesserae showing chondrocytes of regular shape exhibiting a purple halo. (E-F) TB and H&E histology images of the unmineralized cartilage (UC) region near tesserae also revealed strand-like structures that were previously unrecognized in TEM images, appearing to form a network between chondrocytes (ch) near the tesserae layer (T) and deep in the cartilage core. (G) SEM imaging of a decalcified, iodine vapor-coated section showing the strand-like structures aren't artefacts of the histology staining. Abbr.: itj intertesseral joint, P perichondrium.
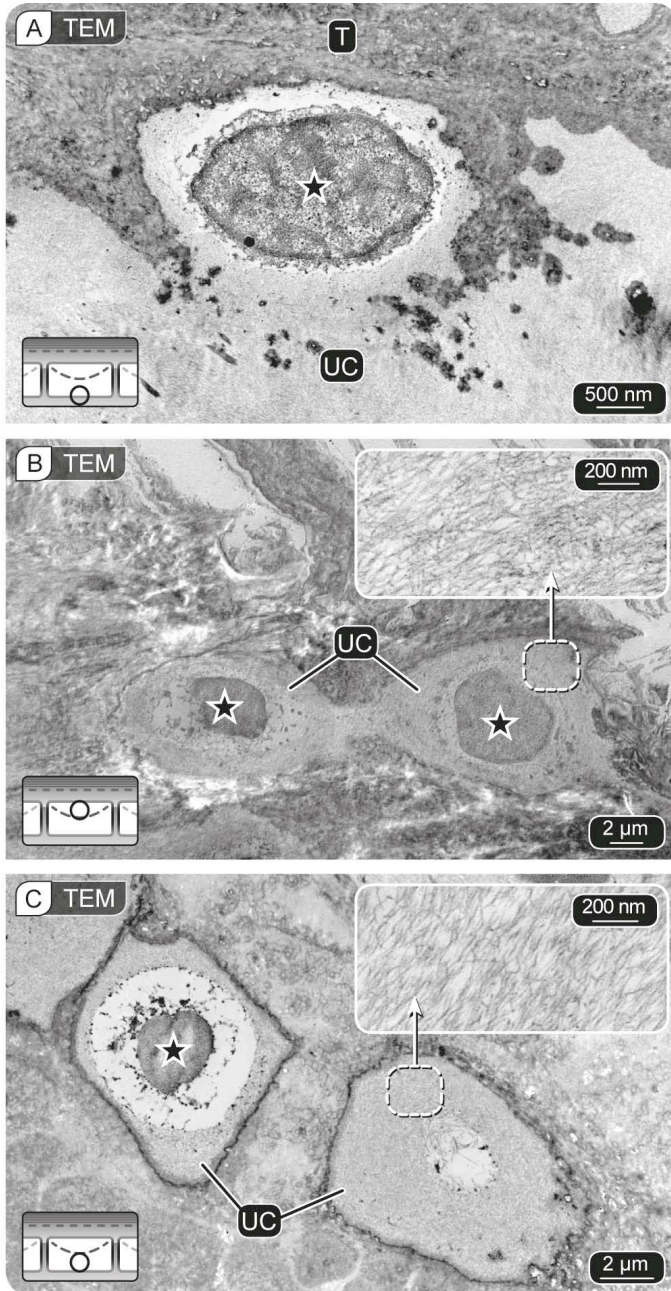
Fig. 8 TEM imaging of chondrocytes in tesserae's lacunar spaces and in the subtesseral uncalcified cartilage.

Decalcified sections of chondrocytes (stars) (A) in the electron-translucent subtesseral uncalcified cartilage (UC) where it is partly surrounded by electron dense tissue (from the tessera, T), (B) in the cap zone and (C) in the body zone of a tessera. Chondrocytes embedded in lacunar spaces in tesserae appear intact, maintaining a pericellular envelope of Coll II unmineralized cartilage (insets) around them and are connected via unmineralized passages between lacunae (image B).

subtesseral uncalcified cartilage, whereas in HE and Toluidine blue, these layers/regions stained differently. In HE, the supratesseral layer stained red, effectively an intermediate staining between those of the perichondrium and uncalcified cartilage. The supratesseral uncalcified cartilage also exhibited a particularly strong, deep purple TB staining (Fig. 9B) and was the only skeletal tissue we observed to stain strongly positively for Coll X (Fig. 9C; see additional comments on Coll X staining in cells in 'Intertesseral joints' below).
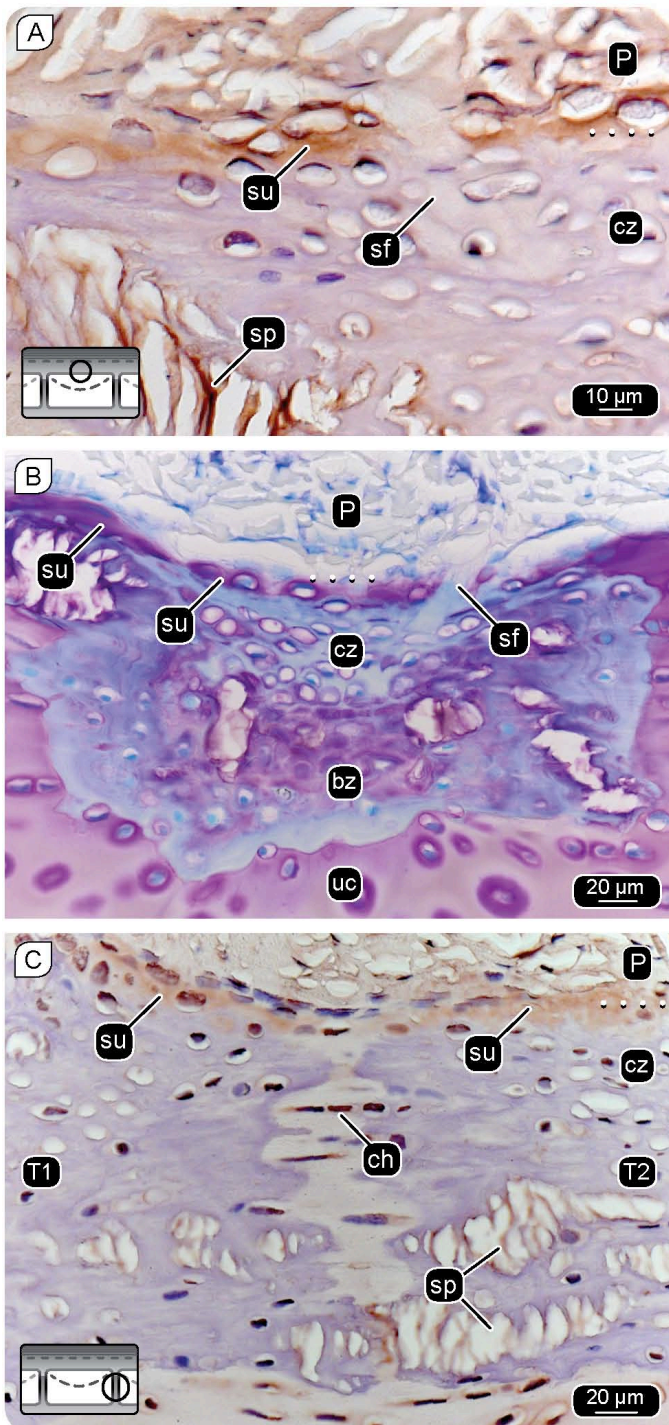
Fig. 9 IHC (Coll II and X) and TB stain of the supratesseral uncalcified cartilage layer.

(A) The supratesseral layer between tesserae and the perichondrium stained positive for Coll II, but also thick Coll I fibril bundles from the perichondrium (Sharpey's fibers, see above) passed through the supratesseral layer to insert into the cap zone of tesserae. (B) Section through a tessera and adjacent regions stained with TB, showing a Sharpey's fiber (sf) from the perichondrium (P) inserting in the tessera's (T) cap zone (cz) after passing through the supratesseral uncalcified cartilage (su) layer. The supratesseral uncalcified cartilage exhibits a particularly strong, deep purple TB staining in contrast to the pale purple staining of the subtesseral cartilage (UC) and the weak staining of the perichondrium and Sharpey's fiber. Abbr. bz body zone. (C) The supratesseral uncalcified cartilage (su) was the only skeletal tissue we observed to stain strongly positively for Coll X. In some Coll X immunostained samples, intertesseral joint cells (ch) and the thin vertical fibrous lamellae in spokes (sp) appeared to stain positively for Coll X; in some of these cells, the staining seemed to be localized to the cytoplasm.

5.3.4 Intertesseral Joints

In skeletal cross-sections (i.e. vertical section of the tesserae layer), individual tesserae were clearly visible, and separated from one another by intertesseral joints (Fig. 10; Seidel et al., 2016). Intertesseral joints are complex features, comprised of planar surfaces where tesserae are in contact (intertesseral contact zones, ICZ; Figs. 1 and 10A, D) and concave regions where fibrous material links the adjacent tesserae (intertesseral fibrous zones, IFZ; Fig. 1; Seidel et al., 2016). The convoluted three-

dimensional arrangements of ICZs and IFZs mean that the proportion of fibrous and mineralized material visible varies with 2D sectioning plane, with some joint sections dominated by mineralized tissue (i.e. ICZs), some being a mix of ICZ and IFZs, and others with unmineralized tissue (IFZs) extending between the supra- and subtesseral uncalcified cartilage layers without interruption by tesseral contact.

HE-stained sections of the intertesseral joints showed cells and fibrous material in intertesseral fibrous zones (Fig. 10B, C). In between the bundles of collagenous and "non-staining" fibrils adjoining adjacent tesserae in the lower, chondral portion of the joint, long end-to-end series of cells could be seen extending from one tessera into the other (Fig. 10B; Clement, 1992; Dean et al., 2009; Dean et al., 2010; Seidel et al., 2016). These intertesseral cells in between fibril bundles typically exhibited an exaggerated spindle morphology (compressed with their length axis parallel to the surrounding fibril bundles and the skeletal surface/tesserae layer), being up to four times longer but less than half the height of uncalcified cartilage core cells with a more typical ellipsoidal chondrocyte shape (Fig. 10C, G). In some Coll X immunostained samples, intertesseral joint cells appeared to stain positively for Coll X; in some of these cells, the staining seemed to be localized to the cytoplasm (Fig. 9C).

TEM imaging occasionally showed individual Coll I fibril bundles originating from the perichondrium, running through the upper portion of the joints into the cap zones (Fig. 10E, F); these bundles were not visible in Coll I stained sections, perhaps due to their sparseness (Fig. 10D). The upper ('perichondral') portions of joints, however, did stain positively for Coll II (Fig. 10G). TEM data revealed that, with the exception of the individual Coll I fibrils and fibril bundles occasionally entering the joint from the perichondrium and the supratesseral layer, the ultrastructural characteristics of the upper joint matrix were the same as those of the uncalcified cartilage core (Fig. 10G, J). This was supported by all histological stains showing a similar staining result for the upper, perichondral joint matrix and the uncalcified cartilage core (Table 2).

The lower ('chondral') portions of joints showed no immunostaining for Coll II, but contained arrays of thin (~10nm in diameter), parallel fibrils that spanned the entire joint, connecting adjacent tesseral body zones (Fig. 10G, I). In TEM, the fibrils were structurally distinct being approximately 20x narrower than Coll I fibrils and unbanded, and densely packed with very little intervening Coll II matrix (Fig. 10G, I). The lower joint fibrils did not stain with orcein, a dye for elastin fibers; in contrast, the internal and external elastin-containing membranes of blood vessels in the same sections stained positively, serving as positive controls (data not shown). In most histological stains the lower joint matrix stained similarly to the uncalcified cartilage core (Fig. 10); however, in some sections Masson's and AZAN staining were either paler or absent.
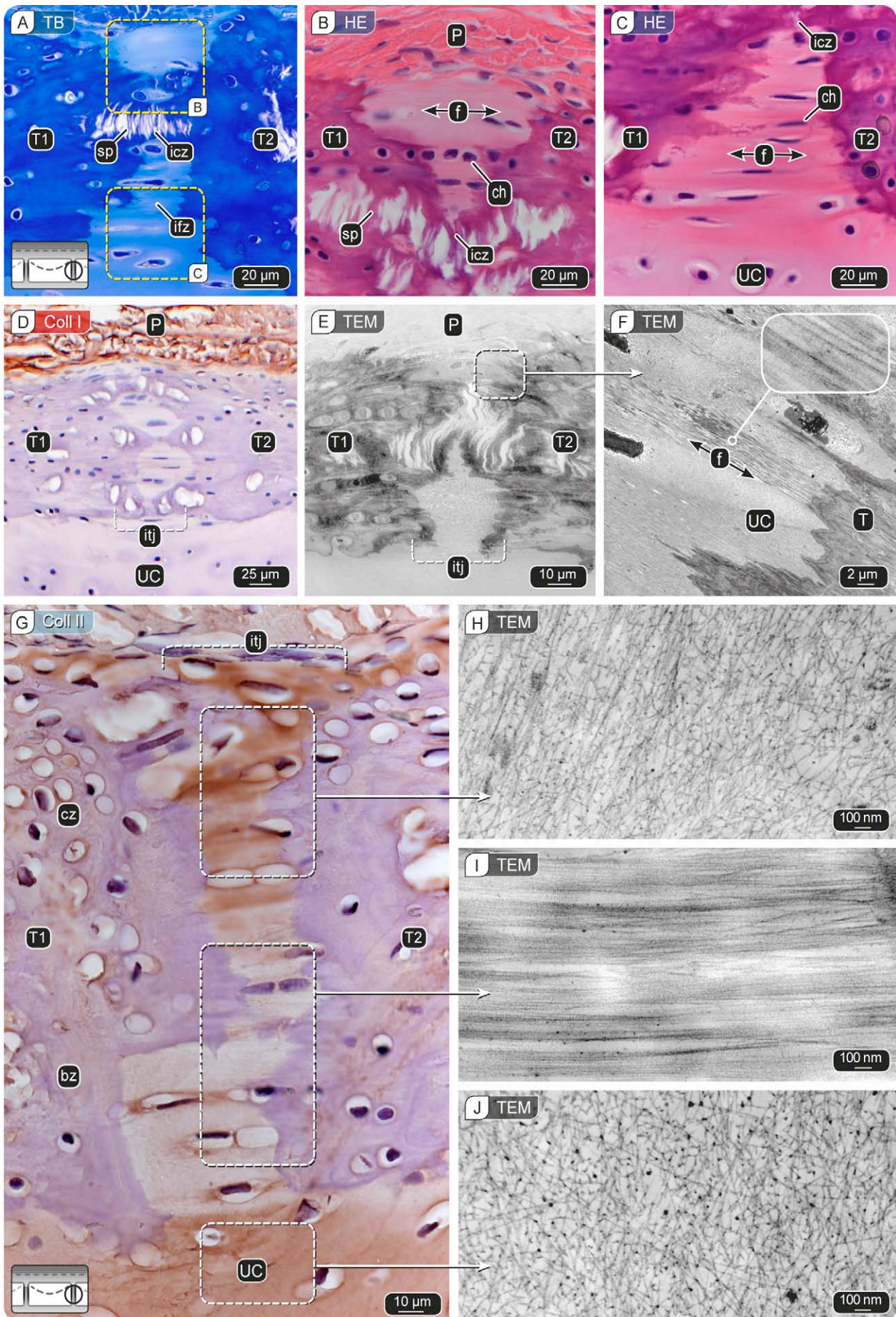
◀ **Fig. 10 Histological staining (TB and HE), IHC (Coll I and II), and TEM imaging of the intertesseral joint.**
(A–C) Section through adjacent tesserae (T1-2) and the intertesseral joint comprised of intertesseral contact zones (icz) with spokes (sp) and intertesseral fibrous zones (ifz) consisting of unmineralized cartilage matrix (UC), intertesseral joint cells (ch) that can exhibit sometimes long and slender morphologies if they are located in between aligned collagenous fibril bundles (f) that link adjacent tesserae. (D) The intertesseral joint and the tesserae stained negative in IHC Coll I stains, in contrast to the perichondrium. However, in the most upper part of the intertesseral joint (E-F) TEM imaging showed some type-I collagenous fibril bundles (f) (inset shows banding of Coll I fibrils) spanning the unmineralized cartilage (UC) 'gap' between tesserae (T) near the perichondrium (P) and insert in the mineralized matrix of tesserae. (G) Zoomed in view of the intertesseral joint (itj) showing the intertesseral fibrous zones (ifz) stained different for Coll II in the upper and lower portions of the joint, associated with the upper and lower portion of tesserae, cap (cz) and body zone (bz), respectively. (H-I) TEM imaging of the different regions in the ifz and comparison with the subtesseral unmineralized cartilage (UC) revealed networks of Coll II fibrils in the upper joint portion and in the UC, (H,J) similar in density and network organisation with random orientation of the fibrils. Coll I fibrils were in some sections observed intermingling the upper portion of the joints (here not shown). (I) TEM image of the lower portion of the joint showing aligned, densely packed fibrils that could not be identified, staining negative for Coll I, II, X and elastin.

5.4   DISCUSSION

Our results show that tesserae of *U. halleri* are bipartite, consisting of spatially-segregated regions of Coll I and Coll II forming the cap and body zones, respectively. This finding challenges previous conservative classifications of tesserae as simply 'calcified cartilage' (Applegate, 1967; Moss, 1977; Kemp and Westrin, 1979; Peignoux-Deville et al., 1982; Clement, 1992; Currey, 1999; Hall, 2005; Dean and Summers, 2006; Seidel et al., 2016). Tesserae grow by mineral apposition on all surfaces (perichondral, chondral and lateral; Kemp and Westrin, 1979; Seidel et al., 2016); the heterogeneity of matrix composition and structure in adult tesserae suggests that their multiple mineralization fronts employ different, locally-controlled mineral precipitation mechanisms and/or are influenced in different ways by their neighboring unmineralized tissues. Below, we differentiate the adult tessera of *U. halleri* into three distinct anatomical regions —perichondral, chondral and lateral— discussing what the tissues and morphologies observed suggest for the growth of elasmobranch tessellated cartilage.

5.4.1   Supratesseral cartilage side (perichondral 'cap' side)

Kemp and Westrin (1979) interpreted the cap zone of tesserae as a "thin veneer of bone", due to the presence of acidophilic Sharpey's fibers and fusiform cells in the tesseral caps of several shark species. We refute this designation, based on structural details of the cap and its association with the
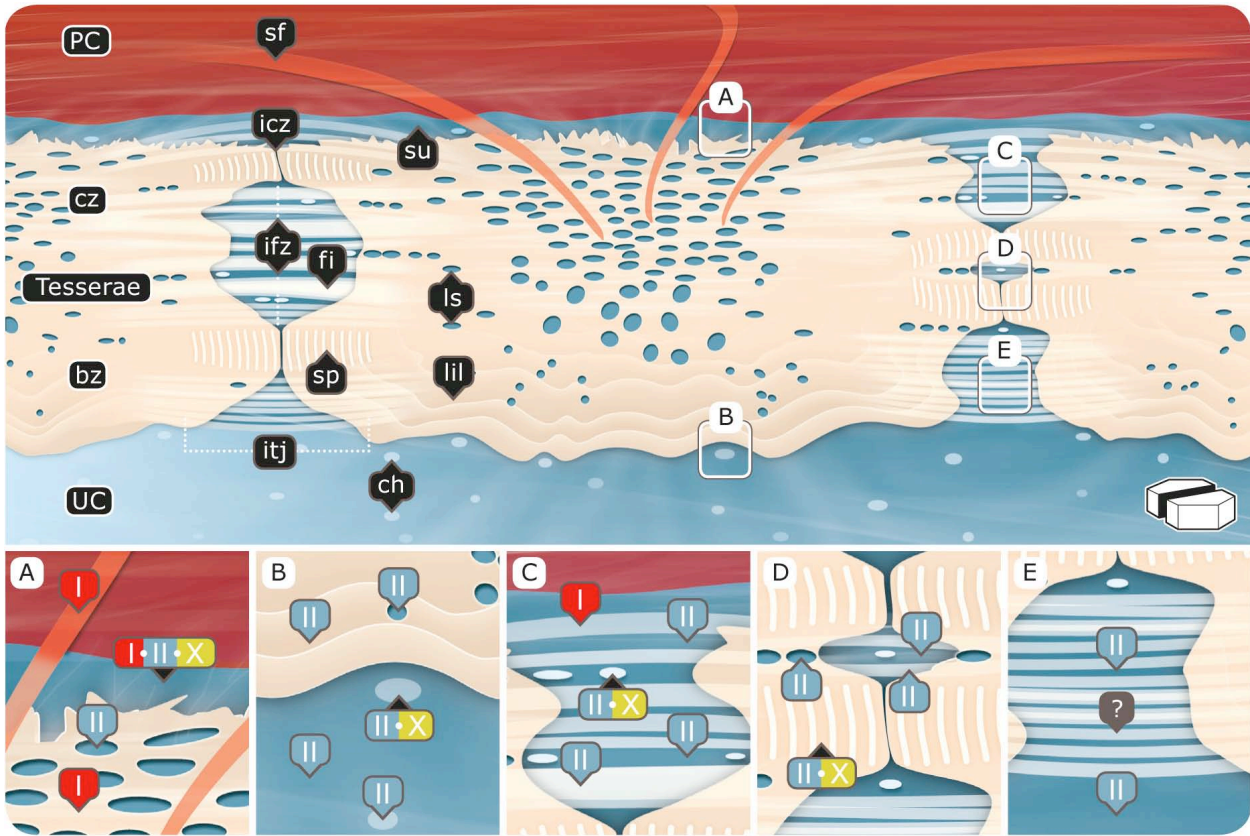
Fig. 11 Collagens in tessellated cartilage of elasmobranchs.
Schematic illustration of a vertical section through the tesseral layer showing the collagenous composition of tesserae and adjacent tissues based on this study (specimens: adult *U. halleri*). Images (A–E) in the lower panel represent magnified views of the regions squared in the upper image. (A) Supratesseral layer of uncalcified cartilage (su) and tesserae cap zone (cz) with lacunar spaces (ls). Sharpey's fibers (sf) coming from the perichondrium (PC) pass through the supratesseral layer to end in the tesseral cap zone. (B) Chondral edge of the tesseral body zone (bz) associated with the unmineralized cartilage core (UC) and chondrocytes (ch) near the tesserae edge. (C) Intertesseral fibrous zone (IFZ) in the upper joint portion showing the unmineralized ground matrix of the joints (UC), and chondrocytes (ch) between collagen fibrils (fi) linking adjacent tesserae. (D) Intertesseral contact zone (ICZ) of two abutting tesserae, with spoke laminae (sp) in the tesseral margins parallel to the ICZ. Lacunar spaces (ls, housing cells that appear intact and alive) in tesserae often form long strings together with chondrocytes (ch) in the unmineralized matrix (UC). (E) Intertesseral fibrous zone in the lower joint portion showing the ground matrix (UC) is the same as the cartilage core (UC), but exhibits intertesseral fibrils that did not stain for Coll I, II, X or elastin in *U. halleri*.

supratesseral cartilage layer, which we believe is of significance to the cap's origin. The supratesseral cartilage layer was noted by several authors in the skeleton of the S. canicula (Lorch, 1949; Bordat, 1988; Egerbacher et al., 2006; Enault et al., 2015), but not in other elasmobranch species (e.g. Ørvig, 1951; Kemp and Westrin, 1979; Dean et al., 2009; Seidel et al., 2016), likely having been overlooked due to the thinness of the layer in some species, and its similarity to perichondrium in SEM and some histological stains.

Although the supra- and subtesseral cartilage tissues appear relatively similar in histological

staining (e.g. with Masson's and AZAN staining; and HE in S. canicula, Enault et al., 2015), we show that they differ in their composition and structure, with the former distinguished by the presence of more fusiform cells (similar to perichondral fibroblasts), the coexistence of Coll I, II and X, and a high concentration of chondroitin sulphate (Fig. 9B; Romeis, 1968: TB stains acid mucopolysaccharides violet-red). The presence of Coll X is notable as this collagen is used as a marker for calcifying cartilage in vertebrates (Poole and Pidoux, 1989; Gannon et al., 1991), and is associated with cell hypertrophy and death (Farnum et al. 2002; Kraan & Berg 2011; Cooper et al. 2013) and vascularization (Maes et al., 2010). The fact that extracellular Coll X expression (in the absence of cell hypertrophy) was observed at the perichondral edge of *U. halleri* tesserae, but appeared to be absent at other tesseral edges, shows that 1) the mechanisms regulating the mineralization of the cap zone are different from those in any other tesseral region, 2) tesserae and cartilage mineralization can occur without Coll X expression (e.g. at the chondral edge), and 3) cell hypertrophy and vascularization are not linked compulsorily to Coll X expression and vertebrate cartilage mineralization (Kwan et al., 1991; van der Kraan & van den Berg, 2011).

Our data lend some support to Kemp and Westrin's (1979) assertion of bone-like tissue in tesserae, showing that the tesseral cap is largely a Coll I-based tissue (like bone). However, we show that it also contains Coll II, sequestered between embedded Sharpey's fibers. Furthermore, the fusiform cells in the cap zone, similar in shape to those in the supratesseral layer, lack the cell processes of osteocytes and appear to be capable of maintaining the unmineralized cartilage (Coll II) matrix that surrounds them and fills the tesseral lacuno-canalicular network. In this way, the cap is more comparable to the chondroid bone known in bony fishes and mammals: a non-transitional, intermediate tissue with bone-like extracellular matrix and cartilage-like cells (Beresford, 1981; Witten and Hall, 2002). This particular amalgamation of cellular and matrix components evokes recent proposals that some mammalian chondrocytes are capable of transdifferentiation into bone-forming (i.e. Coll I matrix-secreting) cells (reviewed in Hinton et al., 2017).

We hypothesize that the cap zone is formed via mineralization of supratesseral cartilage, rather than mineralization of the perichondral tissue, and that this may be a general growth phenomenon for elasmobranch tesserae. Although tesserae continuously accrete mineral and increase in size with age (Seidel et al., 2016), the fact that the supratesseral layer of unmineralized cartilage was found even in adult animals, implies that the supratesseral layer continuously produces matrix throughout life. The supratesseral layer as the source of cap zone tissue would explain the comingling of chondrocytes, Coll II-based matrix and thick Coll I bundles in the cap zone.

This hypothesis is supported by evidence that tesseral development begins in cartilage at some distance from the perichondrium: in pre-tessellate embryos of *S. canicula*, alkaline phosphatase, an enzyme vital to skeletal mineralization in vertebrates (Stephens et al., 1992; Omelon et al., 2014; Dean

et al., 2015), is expressed in the unmineralized cartilage near (not at) the skeletal surface and indicates the future location of tesserae (Lorch, 1949; Eames et al., 2007). A layer of supratesseral cartilage is maintained above the young tesserae in sub-adults of both *U. halleri* (Fig. 3 in Seidel et al., 2016) and *S. canicula* (Fig. 2 in Lorch, 1949; Fig. 1 in Enault et al., 2015). Those supratesseral cartilage Coll I fibrils that are incorporated into the tesseral cap —both sparse individual fibrils and larger bundled Sharpey's fibers— apparently originate in the perichondrium, suggesting that the Coll I content of the supratesseral cartilage is merely a function of perichondral fibrils 'passing through', linking the perichondrium to the tesseral layer. It is unknown, however, how these fibrous connections are established during development (i.e. how sub-surface tesserae become linked with the perichondrium through the supratesseral cartilage), but the presence of similar Sharpey's fibers in tessellated cartilage of other elasmobranchs species (e.g. Kemp and Westrin, 1979; Peignoux-Deville et al., 1982; Clement, 1992; Summers, 2000) and in mammalian bone and dental tissues (Boyde and Jones, 1968; Jones and Boyde, 1974) argues for their being a widespread and highly conserved solution for connecting soft, Coll I-based tissues to vertebrate skeletons.

The nature of the electron dense layer sheathing fibrils of the Sharpey's bundles in the *U. halleri* cap zone is unclear, but may explain the conflicting results of previous studies (e.g. Egerbacher et al., 2006; Enault et al., 2015 arguing for different collagen composition of *S. canicula* tesserae; Table 1). In our study, this layer appeared as an impermeable barrier, preventing Massons' staining and primary IHC antibody binding. The fact that the collagens of other vertebrate hard tissues (e.g. rat incisor cementum: Stern, 1964; our mouse bone controls) appear to lack this electron-dense layer and that our mouse bone controls stained as expected —brown in Coll I IHC, green in Massons' and blue in AZAN stains— suggests fundamental differences in mineral-collagen interactions in elasmobranchs and bony vertebrates. The reason for tesserae in our study and Clement's (1992) staining red with AZAN (which typically stains collagenous tissues blue and only nuclei and cytoplasm red) requires further investigation.

5.4.2 Subtesseral cartilage side (chondral 'body' side)

Our data support the hypothesis that the chondral edge of tesserae is an active mineralization front, adding to the thickness of the tesseral layer by accreting new mineralized, globular matrix onto the undersides of tesserae, and in the process engulfing chondrocytes from the cartilage core into the tesseral body zone (Fig. 8; Kemp and Westrin, 1979; Bordat, 1988; Dean et al., 2009; Dean et al., 2010; Seidel et al., 2016). In contrast to the cap, the body zone appears to be patterned entirely on a Coll II-rich ECM (Fig. 5) and, therefore, is effectively a "true" calcified cartilage. The body zone ECM in demineralized sections exhibited regions of periodic tissue density variation (Fig. 6) correlating with the locations of spokes and Liesegang lines, structural features defined by periodic mineral density

variation, recently characterized in elasmobranch tesserae using backscatter SEM (Fig. 4 in Seidel et al., 2016). Although the contours of Liesegang lines in demineralized sections mirrored those of the chondral margins of tesserae, supporting the hypothesis of Liesegang lines as growth lines (e.g. Ørvig, 1951, Kemp and Westrin, 1979; Seidel et al., 2016), we never observed a similar periodic pattern in the neighboring unmineralized cartilage, as others have reported (Kemp and Westrin, 1979). This argues that the banded tissue patterning (and the negative correlation between matrix collagen density and mineral density in the body zone of tesserae) occurs during the mineralization of the tissue.

The process of matrix mineralization at the chondral edge also appears to be associated with changes in the chondrocytes that become incorporated into the tesseral matrix. In contrast to those cells deeper in the cartilage core, chondrocytes at the chondral margins of tesserae demonstrated evidence of a largely intracellular Coll X expression, different from the extracellular matrix expression of Coll X in the supratesseral cartilage layer, echoing cytoplasmic Coll X expression of pre-hypertrophic chondrocytes in avian cartilage (Gibson et al., 1986). Coll X is typically treated as a marker for terminal differentiation (hypertrophy), for example, in mammalian and avian chondrocytes, and is therefore, considered to be closely associated with endochondral mineralization. The function of Coll X in mineralization is still unclear, but it has been theorized to play a role in stabilizing or organizing the extracellular matrix in the shift from cartilage to bone (Shen, 2005; Chen et al., 2015; van der Kraan & van den Berg, 2012; Reichenberger et al., 1991). However, while Coll X is indeed a product of hypertrophic chondrocytes, it can also be produced by mature, non-hypertrophic chondrocytes as well as by some osteoblasts (Chung et al., 1995; Eames et al., 2012), and can even be found within the ECM of the permanent zone of articular calcified cartilage (ZCC; Gannon et al., 1991).

We support previous work (e.g. Clement, 1992; Dean et al., 2009; Seidel et al., 2016; Seidel et al., 2017) in finding no evidence of hypertrophic chondrocytes associated with tesserae. We have no information about the lifespan and age of elasmobranch chondrocytes, but if Coll X expression could be related to chondrocyte maturity —as in bony fishes (Eames et al., 2012), birds (Adams et al., 1991) and mammals (Gannon et al., 1991)— we would expect to find Coll X expression in at least some chondrocytes in other regions of the skeleton, particularly in some intratesseral cells, as these are likely to be among the oldest in the skeleton (Seidel et al., 2016). Instead, our data indicate that chondrocytes no longer express Coll X once incorporated into tesserae, supporting the argument that, in a broad phylogenetic sense, Coll X is more relevant as a marker for cartilage mineralization than for chondrocyte hypertrophy/maturity.

The localization of Coll X in our data suggests that it co-occurs with expression of the enzyme alkaline phosphatase (ALP) (Eames et al., 2007; Omelon et al., 2014), similar to the expression pattern observed in long bone growth plates in mammals (e.g. Gannon et al., 1991; Stephens et al., 1992). Omelon et al. (2014) provided evidence that, during tesseral mineralization, chondrocytes cease

expression of ALP following their incorporation into tesserae. This implies a concomitant down-regulation of Coll X and ALP following matrix mineralization, and could indicate a shift in chondrocyte activity, from promoting mineralization to inhibiting it (e.g. in order to maintain the patency of intratesseral lacunae and canaliculi and also the unmineralized fibrous zones at the joints; Dean et al., 2010, Seidel et al., 2016).

Our observation of strand-like structures connecting chondrocytes in the cartilage core offers another curious perspective on cartilage evolution, in that similar structures have been observed in a variety of vertebrates, from chimaeroid fishes (Fig. 6D in Liu et al., 2010) and sharks (Fig. 10b in Roth, 1911), to birds and mammals (see review in Lawton et al., 1995; also Figs. 2 and 6 in Blumer et al., 2004). These have borne a variety of names —*Saftbahnen* ('sap/juice channels'), 'interlacunar networks', or simply 'strand-like structures'— and have been variously proposed as nourishment canals, mechanical components of the matrix, or tissue preparation artifacts. Their consistent structural appearance and staining characteristics across taxa (e.g. staining positive with toluidine blue and linking chondrocytes in a web-like network), however, argue they are natural features. Previous work showed that these structures are, at least in rat and chicken, sheets rather than strands or tubes (Cole, 1982; Lawton et al., 1995), and that they can be localized to specific types of cartilage, for example, being found in higher densities in younger (faster-growing) rodent cartilage (Cole, 1982) or only in the resting zone of embryonic chicken cartilage (Blumer et al., 2004). The demonstration that they are also found in the continually growing cartilage of cartilaginous fishes (Roth, 1911; Liu et al., 2010; this study) supports their being an ancient and conserved feature of vertebrate cartilage.

5.4.3 Tesserae lateral side (intertesseral joint side)

The third anatomical region within tesserae is the lateral portion associated with intertesseral joints (ITJ; Figs. 1, 10, 11). Our data show that intertesseral fibrous zones (IFZ) within the joint space comprise a diversity of collagens, different from the matrices of both the cartilage core and perichondrium and therefore suggesting a previously unidentified fibrous network guides the growth of the tessellated pattern in elasmobranch skeletons.

In essence, the ground matrix for the entire IFZ is Coll II, as it is in the cartilage core, supporting the idea that tesserae are completely surrounded by cartilage. However, the composition of this fibrous network exhibits spatial variation within the intertesseral joint space, involving at least three types of collagens forming the fibrous connections between adjacent tesserae (Figs. 10 and 11; Seidel et al., 2016). In the top portions of the IFZ, Coll I intermingled with the Coll II matrix, whereas the lower portions exhibited an unidentified fibrous tissue interspersed with cartilage matrix. This fibrous tissue was glossy in its appearance, stained neither for Coll I, II, X nor elastin, and was only observed in this particular region of the skeleton. As upper and lower portions of the joint can be predicted to

behave differently under certain loading conditions (Fig. 13 in Fratzl et al., 2016), this suggests that this tissue has a specific mechanical function. Additional study is warranted to determine the identity, mechanical properties and spatial arrangement of this tissue.

5.5 CONCLUSIONS

We show that tesserae in adult *U. halleri* are patterned on a spatially complex mixture of at least three collagens (Coll I, II and X). Tesserae are characterized by regional variation, in mineral density distribution and mineralized tissue ultrastructure, cellular shape and distribution, fibrous tissue orientation and type (e.g. this study; Kemp and Westrin, 1979; Seidel et al., 2016). Our results suggest that this is a function of the different unmineralized tissues upon which the cap, body and joint mineralization fronts are based. The development of elasmobranch-specific collagen antibodies and probes for in situ hybridization is vital to verify our TEM and IHC findings. In situ hybridization, in particular, will allow visualization of collagen gene expression activity among the populations of cells surrounding and filling tesserae, which likely have different roles (e.g. in growth and mineralization), but all have the appearance of chondrocytes.

Our findings add to a growing body of literature indicating that vertebrate skeletal tissues are structurally diverse and break many of the established but mammal-centric "rules" regarding how vertebrate skeletons grow and mineralize (Eames et al., 2007; Currey et al., 2016; Witten et al., 2010; Atkins et al., 2014; Dean et al., 2015). The natural phylogenetic variation in these tissues in terms of composition, architecture, growth, and response to load provides a natural laboratory for understanding the underpinnings of skeletal mineralization and the interrelations of the factors involved. Our results suggest that elasmobranch skeletons, for example, could offer useful alternative perspectives on Sharpey's fibers, structural interfaces between Coll I- and Coll II-based tissues (e.g. as in the mammalian growth plate), differences between transient and permanent cartilages, and the role of cells and proteins (e.g. ALP, Coll X) in tissue mineralization.

5.6 ACKNOWLEDGEMENTS

5.7 REFERENCES

Please see the concatenated reference list at the end for all citations provided within this thesis.

> TRANSITION:

In this chapter we characterized the soft tissue underlying tessellated cartilage (incl. tesserae, intertesseral joints and associated tissues) in stingray *U. halleri*, showing that tesserae are in fact bipartite in their collagenous composition composed of a Coll I-based cap and a Coll II-based body zone. Cells from the unmineralized cartilage matrix are embedded in tesserae and appear intact and capable to maintain a surrounding layer of unmineralized cartilage. In this way they seem to be able to regulate, and once embedded in tesserae, inhibit the mineralization of the matrix.

In the following chapter I present data showing presumably what 'happens if mineralization goes bad'. We characterized an unusual, aberrant type of cartilage mineralization associated with the tesseral layer of several species, but in contrast to tesserae mineralization, cells in the unmineralized matrix die when they come in contact with it. <

6. Ultrastructural, material and crystallographic description of endophytic masses – a possible damage response in shark and ray tessellated calcified cartilage

Ronald Seidel [a,*], Michael Blumer [b], Paul Zaslansky [c,d], David Knötel [e], Daniel R. Huber [f], James C. Weaver [g], Peter Fratzl [a], Sidney Omelon [a,h], Luca Bertinetti [a], Mason N. Dean [a]

[a] Department Biomaterials, Max Planck Institute of Colloids & Interfaces, Potsdam, Germany
[b] Division of Clinical and Functional Anatomy, Medical University of Innsbruck, Innsbruck, Austria
[c] Julius Wolff Institute, Charité – Universitätsmedizin Berlin, Germany
[d] Department for Restorative and Preventive Dentistry, Charité – Universitätsmedizin Berlin, Germany
[e] Department Visualization and Data Analysis, Zuse Institute Berlin, Germany
[f] Department of Biology, The University of Tampa, 401 W. Kennedy Blvd, Tampa, FL, USA
[g] Wyss Institute for Biologically Inspired Engineering, Harvard University, Cambridge, MA, USA
[h] Department of Chemical and Biological Engineering, University of Ottawa, Canada

ABSTRACT

The cartilaginous endoskeletons of elasmobranchs (sharks and rays) are reinforced superficially by minute, mineralized tiles, called tesserae. Unlike the bony skeletons of other vertebrates, elasmobranch skeletons have limited healing capability and their tissues' mechanisms for avoiding damage or managing it when it does occur are largely unknown. Here we describe an aberrant type of mineralized elasmobranch skeletal tissue called endophytic masses (EPMs), which grow into the uncalcified cartilage of the skeleton, but exhibit a strikingly different morphology compared to tesserae and other elasmobranch calcified tissues. We use materials and biological tissue characterization techniques, including computed tomography, electron and light microscopy, X-ray and Raman spectroscopy and histology to characterize the morphology, ultrastructure and chemical composition of tesserae-associated EPMs in different elasmobranch species. EPMs appear to develop between and in intimate association with tesserae, but lack the lines of periodic growth and varying mineral density characteristic of tesserae. EPMs are mineral dominated (high mineral and low organic content), comprised of birefringent bundles of large calcium phosphate crystals (likely brushite) aligned end to end in long strings. Both tesserae and EPMs appear to develop in a type-2 collagen-based matrix, but in contrast to tesserae, all chondrocytes embedded or in contact with EPMs are dead and mineralized. The differences outlined between EPMs and tesserae demonstrate them to be distinct tissues. We discuss several possible reasons for EPM development, including tissue reinforcement, repair, and disruptions of mineralization processes, within the context of elasmobranch skeletal biology as well as damage responses of other vertebrate mineralized tissues.

Keywords: Elasmobranch cartilage, Tesserae, Skeleton, Skeletal damage, Mineralization, Callus

6.1 INTRODUCTION

The endoskeletons of sharks and rays (elasmobranch fishes) are typically described as being composed of unmineralized cartilage and two distinct types of calcified cartilage, which differ in their location and ultrastructure. Areolar calcified cartilage is a highly cellular, net-like mineralized tissue, with the cells occupying the holes in the net, that is only found in the centra of the vertebral column (Clement, 1992; Compagno 1988; Huber et al. 2013; Porter et al. 2006). In contrast, tessellated calcified cartilage comprises the remainder and vast majority of the endoskeleton (Fig. 1A–C) (Clement, 1992; Dean & Summers, 2006; Dean et al. 2009; Kemp & Westrin, 1979; Seidel et al. 2016). Tessellated cartilage is a composite tissue, comprised of an unmineralized, hyaline-like cartilage, covered in a thin rind of abutting calcified tiles, polygonal in shape and a few hundred microns in size, called tesserae. On top of this tessellated layer lies a fibrous tissue (perichondrium) wrapping the entire skeletal element (Fig. 1B, D). Tessellated cartilage has received the majority of research attention, and represents both
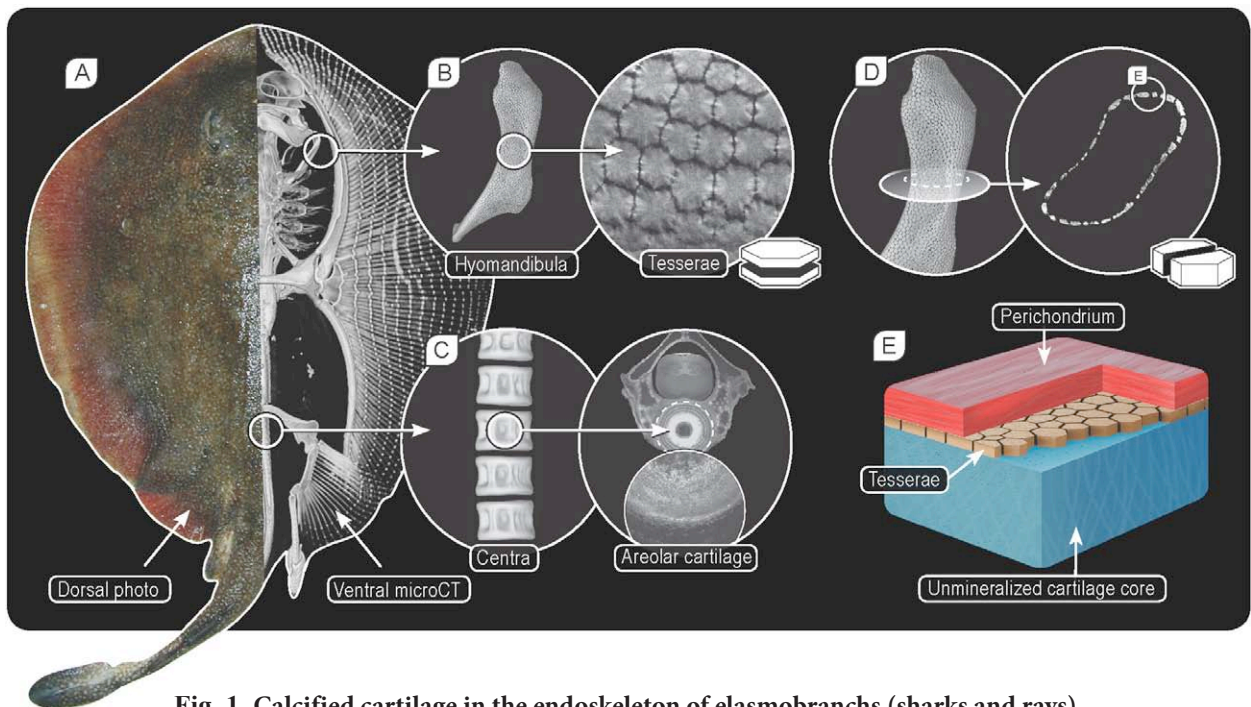

Fig. 1 Calcified cartilage in the endoskeleton of elasmobranchs (sharks and rays).
(A) Photograph of round stingray *Urobatis halleri* (left), and CT image (right) showing most of the skeleton is mineralized (and therefore visible using micro-computed tomography). Two major types of calcified cartilage are described in elasmobranchs: (B) tessellated calcified cartilage consisting of individual mineralized tiles called tesserae (shown here in planar view), covering each skeletal elements' surface and (C) areolar calcified cartilage located in the center of the vertebrae. (D) In cross sections of skeletal elements (here the hyomandibula), tesserae can be seen in vertical view. The section plane and orientation of the samples and images presented in this study are indicated by two icons; each a single schematic tessera sectioned either in planar or vertical view (inset B and D, respectively). (E) General organization of the tissues forming elasmobranchs' endoskeletons showing a mineralized, tessellated layer that is sandwiched between a hyaline cartilage core and an outer fibrous, connective tissue called perichondrium.

a unique skeletal feature among vertebrates and a defining feature of the elasmobranch group for more than 400 million years (Long et al. 2015; Maisey, 2013).

Several additional, but uncommon calcified tissues have been described to date for elasmo-branchs, all of which appear to be modifications of tessellated calcified cartilage, but far less universal in their distribution, being found only in specific parts of the body and/or phylogenetic groups (for summaries of these see Dean, 2011; Maisey, 2013). For example, the skeletons of the rostra of modern lamnid sharks and large extinct sclerorhynchid batoids are covered with exceptionally tall "columnar" tesserae which, in sclerorhynchids, can exhibit a mineralized overlay apparently formed from miner-alization of the perichondrium and obliteration of intertesseral spaces (Fig. 2A–C) (Compagno, 1988; Maisey, 2013; Mollen et al. 2012). The long and slender saws of sawfishes, the jaws of hard prey-eating myliobatiform stingrays and the jaws of a variety of large shark species all are characterized by supra-numerary tesseral layers, a thickening of the skeletal cortex via stacking of multiple tessellated layers (Fig. 2D–F) (Dean et al. 2006; Dingerkus et al. 1991; Summers, 2000).

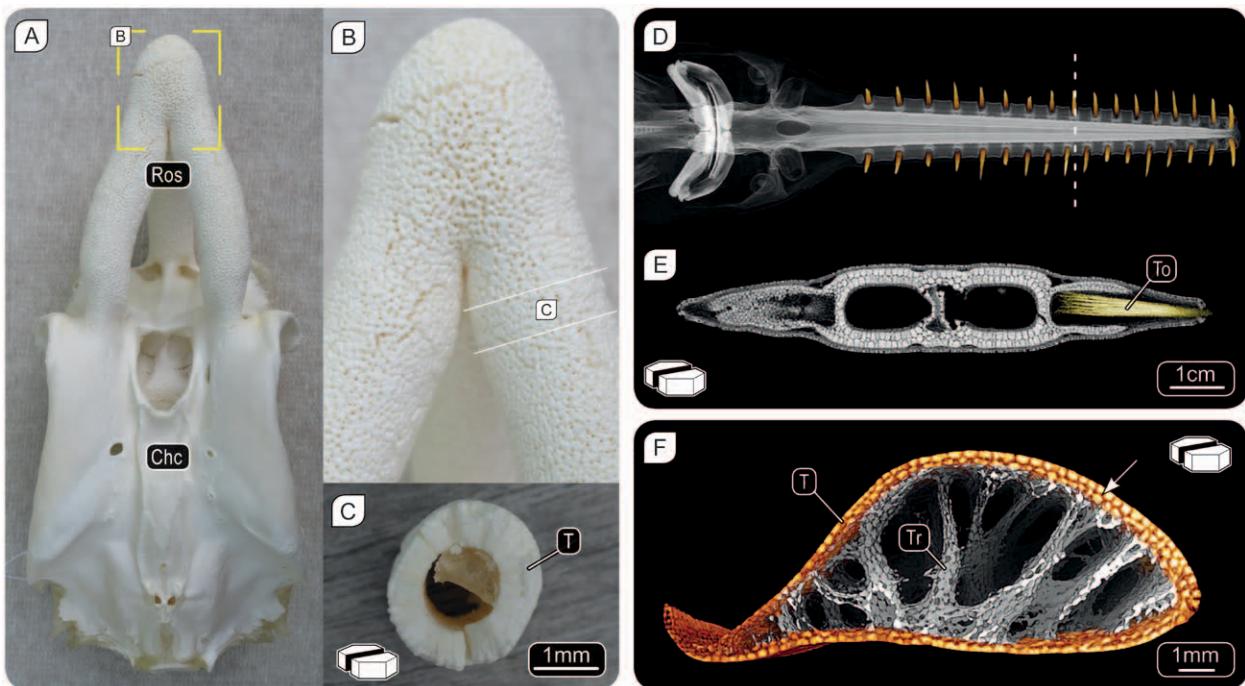In addition, in many elasmobranch taxa, but most pronounced in the jaws of myliobatiform

Fig. 2 Modifications of tessellated calcified cartilage for skeletal reinforcement.
(A–B) Chondrocranium (Cho) of a mackerel shark Lamna nasus, showing the thickened bars of the rostrum (Ros), characteristic of this genus. (C) Cross section of the rostrum as indicated in (B) showing multiple layers of large, "columnar" tesserae. (D) Computed tomography image of the chondrocranium and rostrum/saw of the sawfish Pristis microdon (E) showing 2–3 close-fitting/tight layers of tesserae and a tooth (To) in cross section of the saw. (F) Computed tomography image of a cross section of the lower jaw of a cownose stingray Rhinoptera bonasus, exhibiting supernumerary tesseral layers (T; arrow) and trabeculae (Tr).

stingrays, the skeleton can be further reinforced with trabecular cartilage, where tessellated struts pass through the uncalcified cartilage from one side of the jaw to the other (Fig. 2F) (Dean et al. 2006; Summers, 2000).

All of these mineralized tissues represent variations on the theme of tessellated calcified cartilage and suggest a role in reinforcing skeletal elements, even though they are not all found in areas likely to experience heavy loads. Here, we define a new form of calcified tissue in elasmobranchs, which is associated with tessellated calcified cartilage, but apparently not derived from it. The skeletal features we describe here—which we refer to as endophytic masses (EPMs)—are a drastic departure from the previously described forms, and therefore suggest a new and entirely different process of cartilage calcification. Using a variety of materials and biological tissue characterization techniques, including histology, polarized light microscopy, electron microscopy and diffraction studies, we show that EPMs exhibit an entirely different composition and ultrastructure compared to tesserae. Also, as we demonstrate that EPMs occur in a variety of disparate but related species, we argue that they are natural features of tessellated calcified cartilage, discussing also their origin and role in shark and ray skeletons.

6.2 MATERIALS & METHODS

6.2.1 Species examined & sample preparation

We discovered EPMs in samples which had been prepared for another study (Seidel et al. 2016), either frozen and fixed for examination in microCT or plastic-embedded and sectioned for light and electron microscopy. All characterization/visualization techniques in the current study (excluding microCT, which was performed on whole, ethanol-fixed samples) use the plastic embedded sections described below, with some techniques (histology, TEM) requiring further sample preparation to remove embedding material.

In addition, to verify that EPMs were not an artifactual result of sample preparation (e.g. ethanol dehydration and/or fixation), a variety of control samples were prepared. Fresh (non-fixed) hyomandibular or shoulder girdle (propterygium) samples from several shark and batoid species were examined either as manual cross sections in light microscopy or as intact skeletal pieces in microCT. Furthermore, propterygium samples from *Urobatis halleri* and *Leucoraja naevus* were incubated for 5 months in either water, dehydrating agent (EtOH series) or other fixative media (paraformaldehyde, PFA) and observed regularly for EPM growth.

Jaw, hyomandibular, or propterygium cartilages were excised from frozen adult elasmobranch specimens (skates/rays: *Amblyraja radiata*, *L. naevus*, *Raja montagui*, *U. halleri*; sharks: *Negaprion*

brevirostris, *Scyliorhinus retifer*); excepting *U. halleri* with three specimens, we examined one specimen per species. Specimens were acquired from bycatch from research cruises at other institutions, except for S. retifer, which were lab-raised. Samples were embedded in plastic resin (polymethyl methacrylate, PMMA), cut in slices (300 ± 100 μm thick; Buehler IsoMet low speed saw) and mounted on a PMMA object slide using double-sided adhesive tape. Sections were wet polished with silicon carbide papers with descending grain sizes (Logitech PM5 Precision Lapping and Polishing Machine), then polished using a soft polishing plate and diamond spray (0.25 μm grain size). For more detailed discussion of sample preparation, see Seidel et al. (2016).

6.2.2 Microcomputed tomography (microCT)

Hyomandibulae from an age series of *U. halleri* (7.0, 11.0, 14.4 and 19.0 cm disc width: DW, the maximum lateral dimension of the animal) were dissected and transferred through an ascending alcohol series, then stored for several weeks until scanning in 75% EtOH. For scanning, samples were gripped in hand-cut polystyrene cradles and sealed in PVA vials partially filled with 75% EtOH (to create a humidified scanning environment, but not touching the samples) and scanned with a Skyscan 1172 desktop microCT scanner (Bruker microCT, Kontich, Belgium). Scans for all samples were performed with voxel sizes of 4.89 μm, at 59 kV source voltage and 167 mA source current, over 360° of sample rotation.

6.2.3 Backscatter scanning electron microscopy (BSE) and energy dispersive X-ray spectroscopy (EDS)

BSE microscopy allows the imaging of either changes in tissue elemental density or composition as grayscale variation. Images were acquired of polished PMMA-embedded samples from *N. brevirostris*, *U. halleri*, *L. naevus*, and *R. montagui* jaw, hyomandibular, and propterygium cartilages in backscatter mode using a Field Emission-Environmental Scanning Electron Microscope (FE-ESEM, FEI Quanta 600F) in environmental mode (i.e. at low vacuum without sputtering) with acceleration voltage of 10–12.5 kV.

To determine the nature of the grayscale variation observed in BSE, we examined samples from *L. naevus* propterygium cartilages under EDS using a JEOL JSM 7500F scanning electron microscope equipped with two Oxford X-Max 150 Silicon drift detectors. Using EDS, we compared the elemental composition of tesserae and EPMs in the skate *L. naevus* with regards to elements relevant to mineral formation (calcium, magnesium, sodium, phosphorus and sulfur). All EDS spectra and elemental maps were acquired at 20 kV acceleration voltage and paired with images of the same regions of interest taken under the same conditions in backscatter mode or with a secondary electron detector. To perform a semiquantitative analysis on the mineral phases, a hydroxyapatite standard of known composition

was measured to standardize the EDS quantification routines for Ca, O and P. As few data exist for elasmobranch skeletal tissue mineral composition or crystallography, a human bone sample of known elemental composition was also examined to validate the standardization. The bone sample, from an adult woman's femur, was provided by the Department of Forensic Medicine of the Medical University of Vienna, in accordance with the ethics commission board of this institution (EK#: 1757/2013); the sample had been stained with Rhodamine6G for another study, but this has no effect on our elemental analysis. All samples were coated with a conductive layer of carbon, and so this element was excluded from the semi-quantitative analyses; the composition data we report therefore sum to 100% without C.

6.2.4 Transmission electron microscopy (TEM)

For TEM, PMMA-embedded hyomandibulae samples from a skate (*R. montagui*) were used. PMMA was removed with acetone overnight and subsequently the samples were embedded in EPON resin. Serial ultrathin sections (150 nm) were cut on a Reichert Ultracut S microtome (Leica Microsystem, Wetzlar, Germany) with an ultra-diamond knife, and mounted on dioxan-formvar coated slot-grids (#G2500C, Christine Gröpl, Elektronenmikroskopie, Tulln, Austria). Although these sections had high native contrast due to their slice thickness and did not require staining with uranyl acetate (pH = 3.5) and lead citrate (pH = 8.0), we stained every third section (Leica Ultrostainer, Leica Microsystem, Wetzlar, Germany) to highlight delicate structures such as collagen fibers. The sections were examined with a Philips CM 120 transmission electron microscope at 80 kV (FEI, Eindhoven, Netherlands) equipped with a MORADA digital camera (Olympus SIS, Münster, Germany). To compare crystallographic characteristics of tesserae and EPMs, we performed selected area electron diffraction (SAED) using a ZEISS EM 912X transmission electron microscope working at 120 keV. The TEM images were used to measure EPM crystal dimensions, and assuming that, in the various images acquired, the crystals are axially randomly oriented we estimated the 3D size of the crystals taking the maximum and minimum sizes perpendicular to the particles' long axes.

6.2.5 Raman spectroscopy

Raman spectra of three EPMs, tesserae and uncalcified cartilage within embedded samples were acquired from an *L. naevus* jaw vertical section using a confocal Raman microscope (CRM200, WITec GmbH, Ulm, Germany) equipped with a P-500 piezoscanner (Physik Instrumente, Karlsruhe, Germany) and a CCDsensor (Princeton Instruments Inc., Trenton, NJ). A 785 nm laser (Toptica Photonics AG, Graefelfing, Germany) was used to generate Raman scattering while minimizing autofluorescence and the resulting spectra were investigated using WITec Project software (v. 2.10, WITec GmbH, Ulm, Germany). Brushite and calcium pyrophosphate dihydrate (CPPD) were synthesized for comparison with EPM spectra, as both of these phases were previously identified in calcified cartilage (McCarty

et al. 1966). Synthetic brushite was precipitated with K2HPO4 (Sigma), Na2HPO4 (ChemCruz), and CaCl2•2H2O (Roth), as described in Temizel et al. (2011). Synthetic CPPD triclinic was synthesized according to Brown et al. (1963).

6.2.6. Polarized light microscopy (PLM)

PLM was performed on polished samples (sections of ~150–300 μm thickness) of *N. brevirostris*, *U. halleri*, *L. naevus*, and *R. montagui* jaw, hyomandibular, and propterygium cartilages, showing tesserae in vertical section (cross sections with perichondrium on one side of the tessera and uncalcified cartilage on the other; Fig. 1), using a Leica microscope DMRXA2, camera DFC480, and the imaging software LAS X. The orientation of collagen fibers could be discerned since birefringence varied with fiber angle, with a maximum birefringence signal seen at ±45º relative to the position of the microscope's polarizer and analyzer. We used a lambda filter to render positive and negative orientations with color contrast to allow finer scale distinction of EPM collagen fiber orientation.

6.2.7 Histology

Von Kossa (VK) staining was performed on the PMMAembedded cross-sections (300–380 μm) of hyomandibula of *L. naevus*. VK is typically used as a stain for mineralized tissues: VK stains phosphate ions that are common to calcium phosphate deposits (e.g. in mineralized tissues), via the precipitation of phosphate with silver ions, forming yellow/brown silver phosphate. The VK stain therefore indicates the presence of phosphates in calcium phosphate-based mineralized tissues (Kóssa, 1901; Puchtler and Meloan, 1978), not calcium, as claimed by some authors (e.g. Ashhurst, 2004; Dettmeyer, 2011; Romeis, 1968). The silver stain is further reduced to black under strong light, via the reduction of silver into silver phosphate by surrounding organic material (Puchtler and Meloan, 1985). To allow stain penetration, PMMA was removed with acetone for 2 h, then sections were hydrated in a descending series of ethanol (100%, 90% and 70%) and rinsed in distilled water. Floating sections were incubated in 5% silver nitrate placed under light (60Wlight bulb) for 1 h at room temperature (Allerstorfer et al. 2010; Álvarez et al. 2005; Blumbach et al. 2008; Blumer et al. 2012). Subsequently, they were rinsed in distilled water, and unreacted silver was removed with 5% sodium thiosulfate incubation for 5 min. Sections were rinsed again, mounted on glass slides and either embedded in entellan (after dehydration in ethanol) or distilled water without counterstaining. The sections were examined with a Zeiss Axioplan 2 (Zeiss, Oberkochen, Germany) and photographed as color images, using a Zeiss AxioCam HR and AxioVision 4.1. software. To increase the contrast of the sections, the aperture of the light microscope was closed slightly.
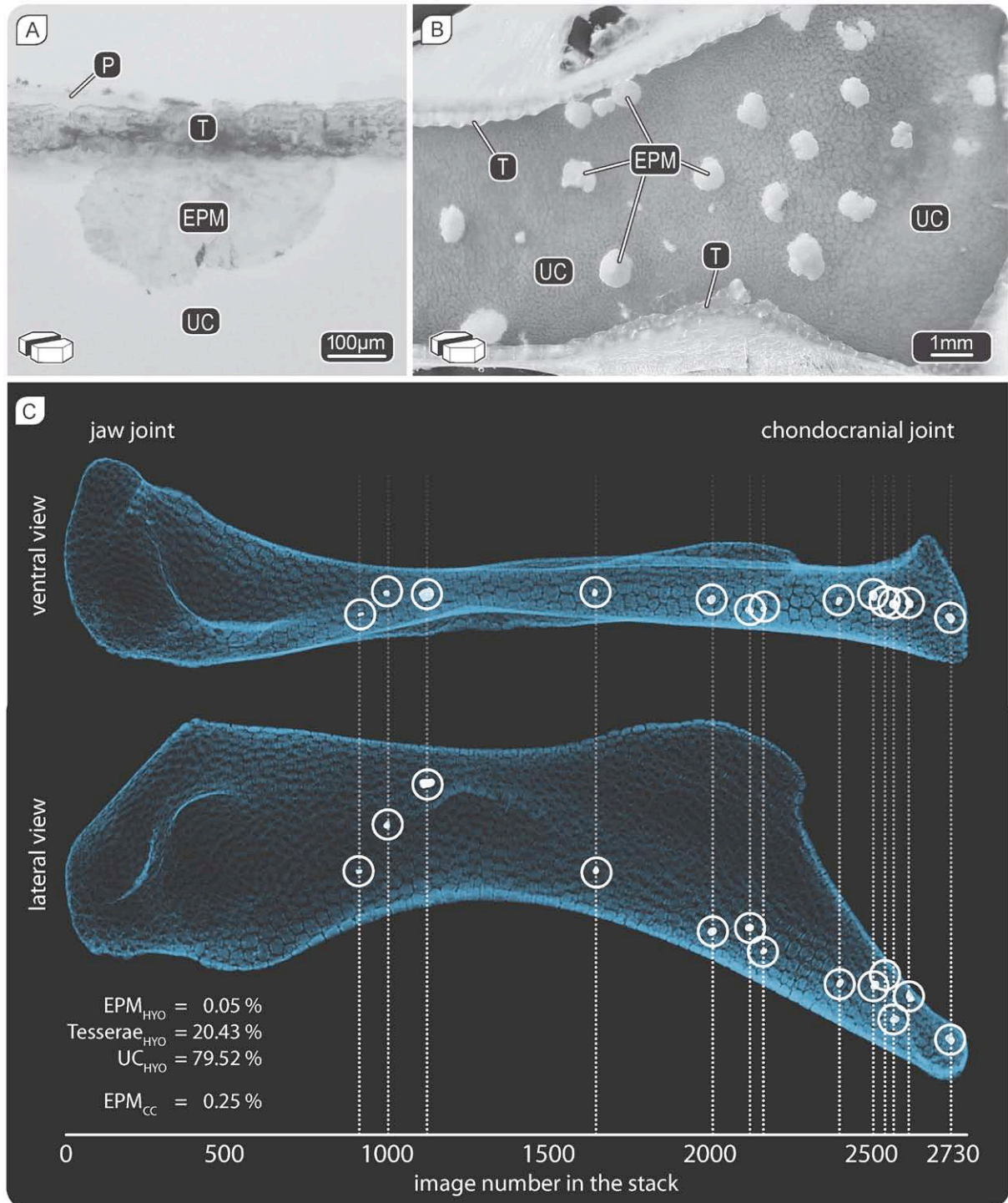
Fig. 3 Distribution of endophytic masses (EPMs) in skeletal elements of elasmobranchs.
(A) Transmittance light microscopy and (B) reflectance light microscopy (LM) images of cross-sections of unstained skeletal elements (propterygia) from *N. brevirostris* and *L. naevus*, respectively, showing the tessellated cartilage layer in vertical view. In transmittance LM of thin sections (<250 μm), EPMs and uncalcified cartilage (UC) appear almost transparent. Note in (B) that some EPMs are associated with tesserae (T), while others are located deeper in the tissue (slice thickness: ~350 μm). (C) Micro-computed tomography imaging showing the occurrence of EPMs in the hyomandibula of *U. halleri*. EPMs constitute a very small volumetric percent of the overall skeletal element; volume fractions for each component of the skeletal tissue are listed on the lower left (hyo = percentage of the total hyomandibula volume; cc = percentage of the total calcified cartilage volume, tesserae and EPM).

6.3   RESULTS

Endophytic masses (EPMs) were almost transparent in thin skeletal sections (<250 μm) using transmittance light microscopy (Fig. 3A). However, in thicker sections (~350 μm), using reflectance light microscopy, EPMs stood out as opaque, white masses against the nearly transparent uncalcified cartilage core of skeletal elements and the surrounding outer layer of mineralized cartilage (tesserae) (Fig. 3B). EPMs were found in a variety of the cranial and shoulder girdle skeletal elements observed, and in multiple species: a shark (*N. brevirostris*), one stingray (*U. halleri*) and two skates (*L. naevus*, *R. montagui*). EPMs did not form in any of the control samples prepared from *U. halleri* or *L. naevus* propterygia or hyomandibulae, incubated for up to 5 months in either water, EtOH series or PFA.

EPMs were typically associated with the inner, chondral edge of the mineralized tesseral layer, appearing semi-circular in cross section with a diameter of ~300–500 μm (Fig. 3A and B). Sometimes, EPMs were found deeper inside the cartilaginous skeletal element, a short distance from the tessellated layer, but with no apparent association, being typically slightly larger than tesserae associated EPMs (~200–600 μm in diameter) and exhibiting a more circular shape (Fig. 3B). We will focus primarily on the description of tesserae-associated EPMs for the remainder of the results, referring to them simply as EPMs.
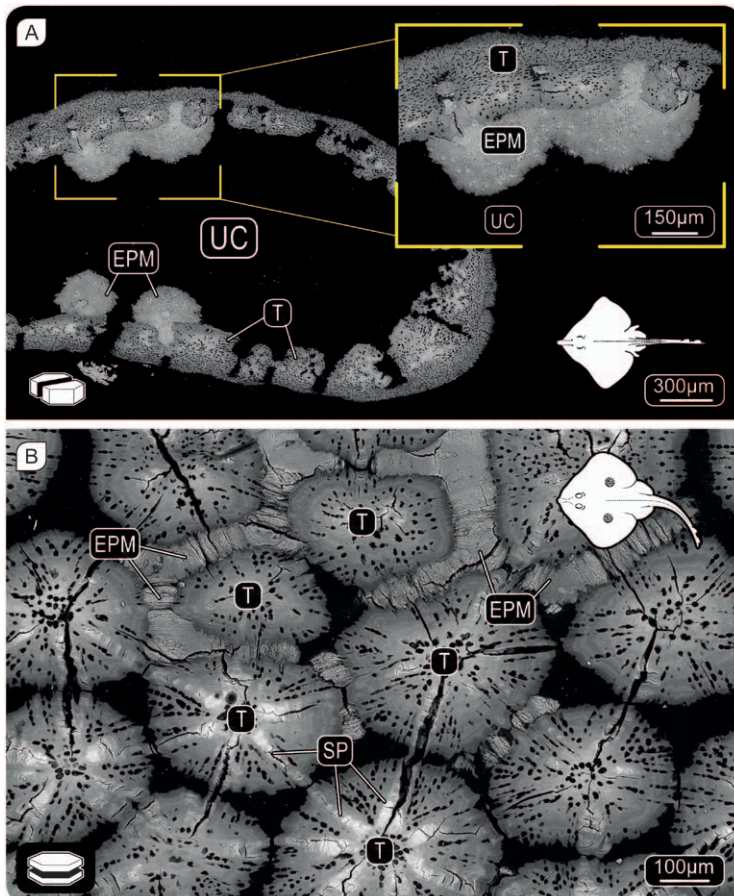

Fig. 4 Mineralized, tesserae-associated endophytic masses.
(A) EPMs at intertesseral joints in vertical view (*R. montagui*) and (B) at intersections of several tesserae in planar view (*L. naevus*). Mineralized EPMs appeared to cluster forming larger masses along the chondral edges of tesserae, covering larger areas and multiple intertesseral joints. In these backscatter SEM images, variation in grayscale represents mineral density variation, with the spokes (SP) within tesserae (T) showing the highest mineral density and the uncalcified cartilage (UC) the least. EPMs exhibit some variation in mineral density between specimens, but typically have mineral densities comparable to the non-spoke regions of tesserae.
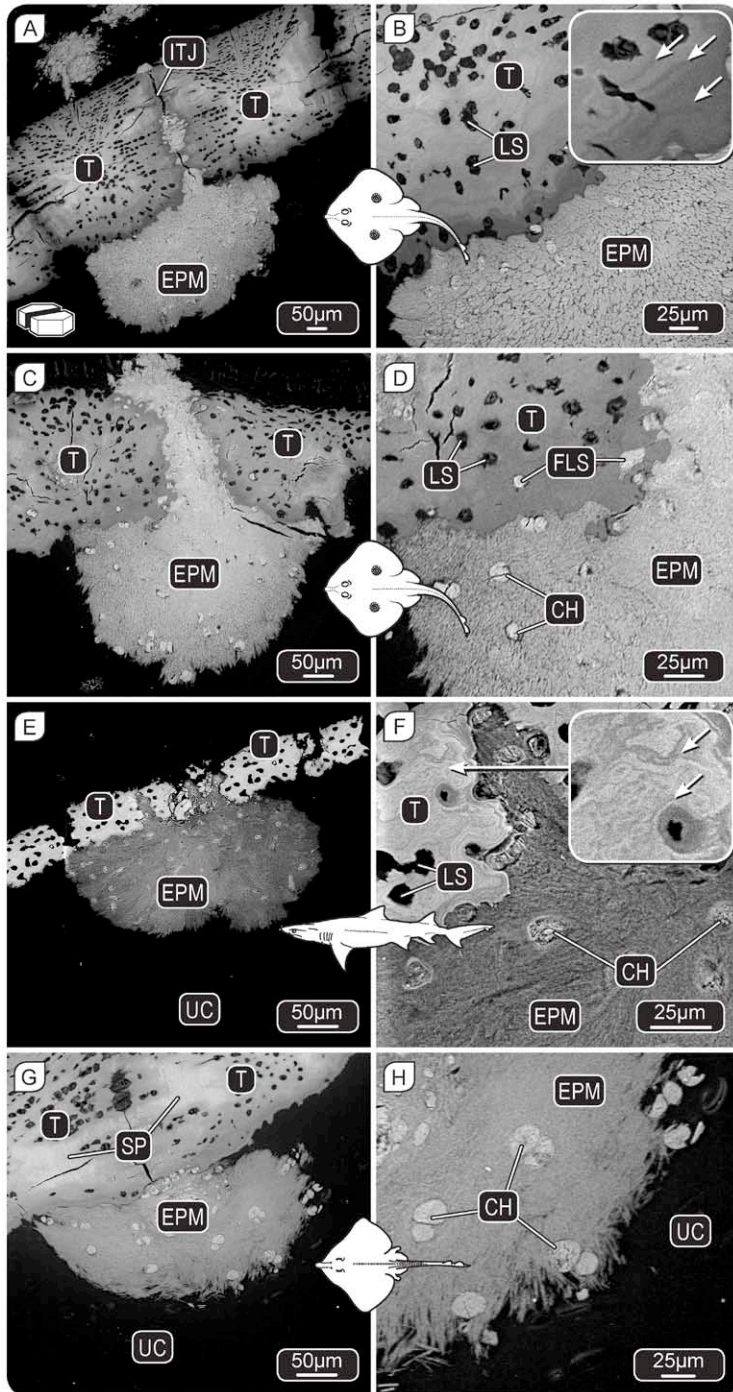
Fig. 5 Ultrastructure of mineralized, tesserae-associated endophytic masses (EPMs).

Characteristic mushroom shape of individual mineralized EPMs associated with tesserae, in backscatter SEM images of vertical views from tessellated calcified cartilage of several elasmobranch species; (A–D) *L. naevus*; (E–F) *N. brevirostris*; (G–H) *R. montagui*. EPMs occurred predominantly at intertesseral joints (ITJ), squeezing between two tesserae, growing into the unmineralized cartilage (UC). In some sections, EPMs appeared to continue into the perichondrium on the "outer" side of the tesseral layer (image A, C). The tissue around EPMs appeared to be intact in almost all EPM sections and no obvious damage of the unmineralized cartilage was observed; the broken tesserae visible in image E are a result of sample preparation. The chondrocytes (CH) at the EPM mineralization fronts and within EPMs were dead and heavily mineralized. Also, the lacunar spaces (LS) in tesserae, which house living chondrocytes (Dean et al. 2010), were sometimes filled with mineral (FLS) where they bordered EPMs (image D). Filled lacunar spaces exhibited a similar mineral density as the spokes (SP), the most pronounced features of adult tesserae (image G). Insets (image B, F) are magnifications showing Liesegang lines, another feature of mineral density in tesserae, which was not observed in EPMs.

EPMs were irregularly distributed within skeletal elements, with some sections lacking EPMs entirely while others contained multiple (e.g. 16 in ~85 mm2 of uncalcified cartilage in Fig. 3B). The distribution was also inconsistent when comparing different hyomandibulae: of the several paired hyomandibulae (14 skeletal elements) we microCT scanned from several ages of *U. halleri*, EPMs were observed in only three hyomandibulae, from two different sub-adult animals (11 & 12 cm disc width, male & female, respectively; Fig. 3C). In total, 24 EPMs were found among these three CT scanned hyomandibulae, with the largest number of EPMs (13) found in the right hyomandibula of the 11 cm
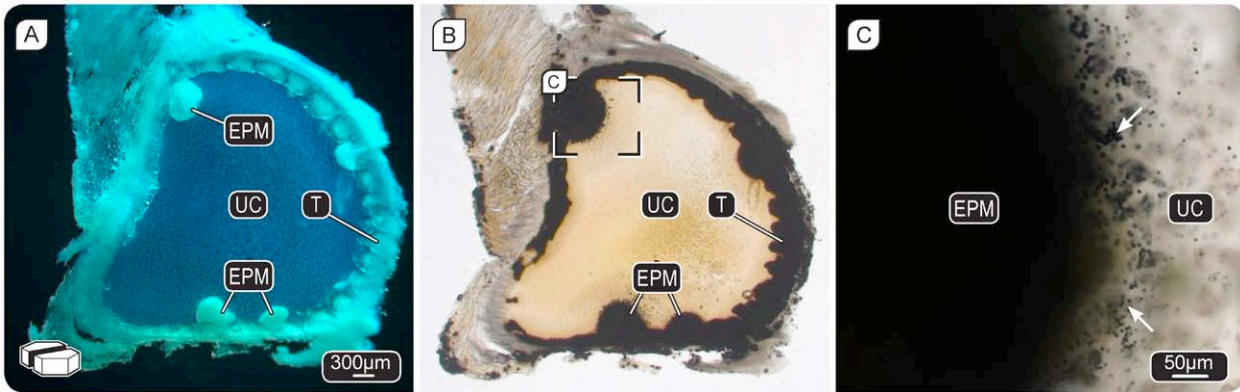
Fig. 6 von Kossa staining of tesserae and EPMs.

(A) Reflectance light microscopy images of opaque EPMs in the almost transparent uncalcified cartilage (UC) of unstained skeletal elements (propterygia) from *L. naevus* (slice thickness: ~350 µm). (B) The same section from (A) stained with VK to illustrate that both tesserae and EPMs are phosphate-containing tissues; coupled with backscatter SEM data (e.g. Figs. 4 and 5), this verifies that both are calcified tissues. (C) Small cell-associated granules in the unmineralized cartilage near the EPM mineralization front were visible (white arrows), in long-incubated VK-stained samples, but never short-incubated samples, nor in BSE, nor TEM imaging. The cells containing these granules (nearly invisible here due to lack of staining) are likely precursors to mineralized cells in EPMs and otherwise look similar to chondrocytes further away from the EPM.
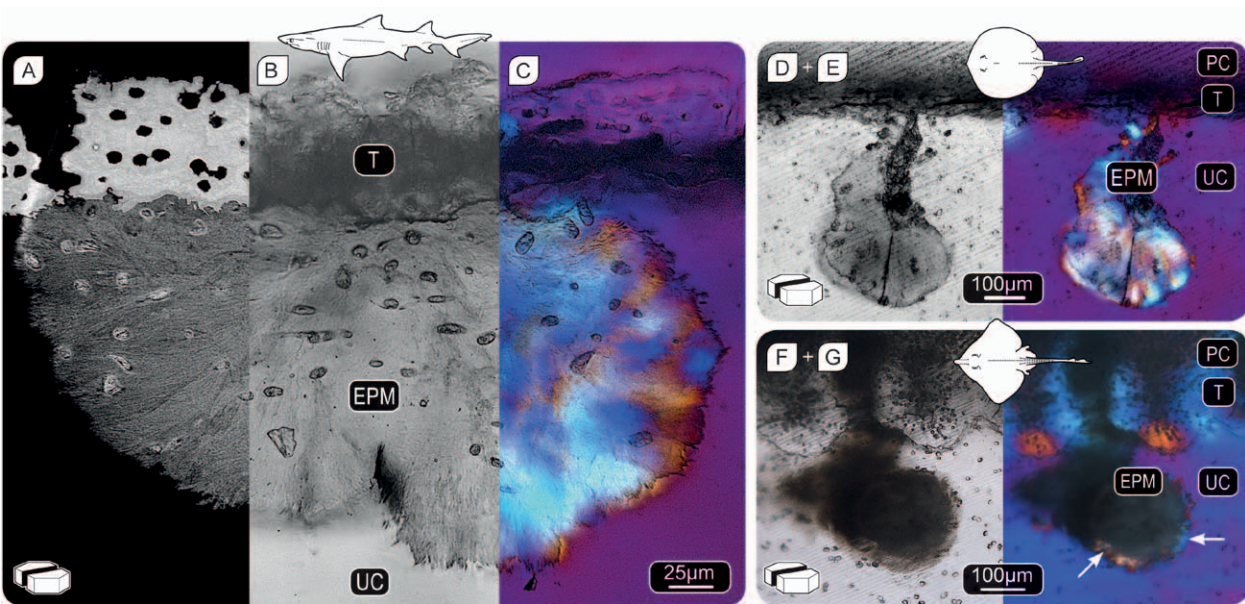
Fig. 7 Birefringence and ultrastructure of EPMs.

(A–C) Vertical section of a tessera-associated EPM in *N. brevirostris* in (A) backscatter SEM imaging, (B) transmitted light microscopy and (C) polarized light microscopy with lambda filter showing EPMs' birefringent fibrous texture and frayed margins. (D–G) Transmitted light and polarized light microscopy of tesserae-associated EPMs in vertical view of two different species, highlighting the variation in the degree of EPMs' birefringence which was not related to the slice thickness. (D–E) EPMs in round stingray *U. halleri* were highly birefringent, whereas (F–G) EPMs in *R. montagui* exhibited only little birefringence mostly at the margins (arrows), suggesting that the variation in birefringence can be either linked to developmental stages or ultrastructural differences.

Fig. 8 TEM micrographs and SAED patterns of elasmobranch skeletal cartilage.
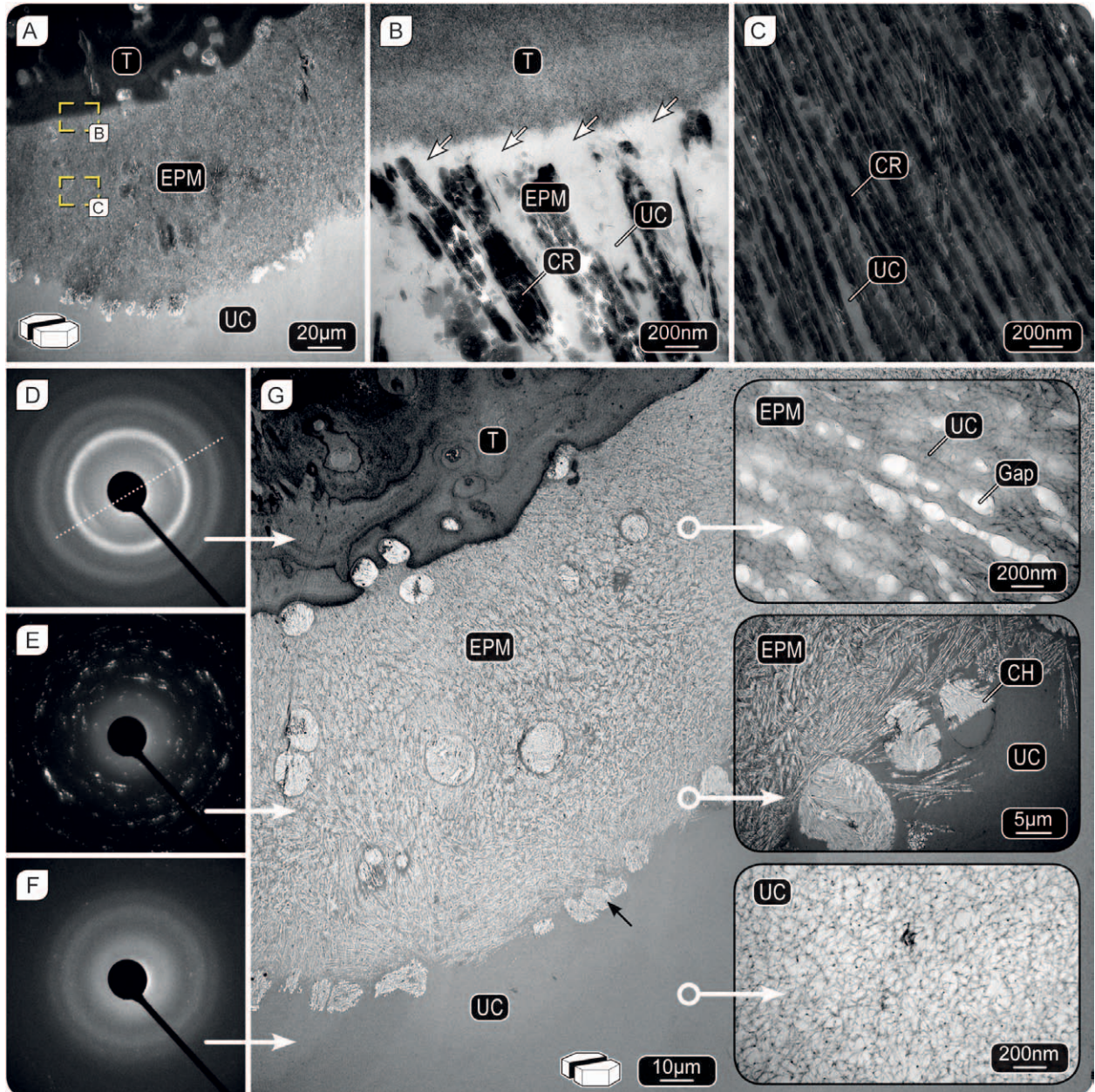(A–C) Unstained thin-sections of tessera-associated EPMs of *R. montagui* showing the profound differences in crystal size and density between tesserae (T) and EPMs, with the latter exhibiting large, aligned crystals (Cr) forming long strings of crystals, embedded in unmineralized cartilage (UC). Tesserae and EPMs were commonly separated from one another by small gaps of unmineralized cartilage (white arrows in B). (D– F) SAED patterns of (D) a tessera, (E) an EPM and (F) unmineralized cartilage. Comparison of D) and E) illustrates the extreme difference in crystal size between tesserae and EPMs, while also showing that (D) crystallites in the chondral margin of tesserae are aligned roughly parallel to the tesseral edge. (G) Stained thin-section of a tessera-associated EPM showing type-2 collagen based uncalcified cartilage (UC) interspersed between EPM crystals. Gaps in the UC matrix represent former positions of crystals, which were removed in the staining process due to the acidic properties of uranyl acetate (see Material and Methods). Mineralized chondrocytes in the EPM and at the EPM edge (black arrow, and middle inset) show high crystal densities, suggesting a lower portion of organics in the cells compared to the extracellular matrix (UC).

disc width male. Despite the large number of EPMs in this sample, they only occupied a small portion of the hyomandibula (0.05% by volume).

EPMs occurred in particular at intertesseral joints or at intersections of several tesserae (Fig. 4). In many sections, individual EPMs exhibited narrow "stems" tethering them to the tesseral layer, squeezed between tesserae, so that EPMs appeared to protrude into the uncalcified cartilage like mushrooms (Figs. 4A, 5). The EPMs' mushroom-like bodies extended into the unmineralized cartilage on average a few hundred microns; however, their size varied considerably within skeletal elements. In some sections, the EPMs' stems could be seen to extend through the tesseral mat up into the fibrous perichondrium layer, where the EPM matrix spread into the connective tissue in a relatively formless mass (Fig. 5A, C). The tissue surrounding EPMs (e.g. unmineralized cartilage, tesserae and perichondrium) appeared intact, without gaps or cracks (except in cases where tesserae were fractured due to sample preparation).

EPMs can be distinguished from surrounding tissues by several aspects of their structure and appearance. Both tesserae and EPMs are mineralized, evident from BSE images (Figs. 4 and 5) and VK staining (Fig. 6), in contrast to the surrounding, non-mineralized musculature, connective tissue (i.e. perichondrium) and the uncalcified cartilaginous core of the skeleton (Figs. 4–6). The mineral density of the EPM matrix is relatively uniform across the tissue mass, but variable relative to tesserae, being at times higher, lower or the
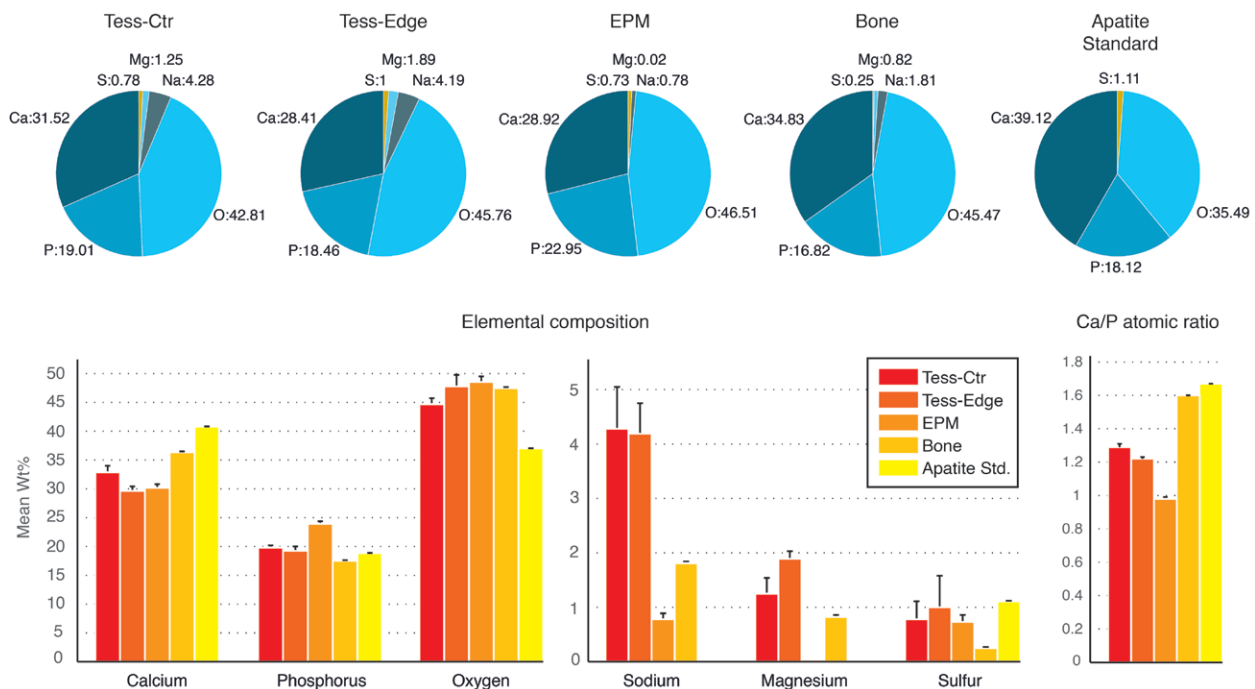
Fig. 9 Chemical analysis of tesserae and EPMs in skate *L. naevus*.
Energy Dispersive Spectroscopy (EDS) data for two regions of tesserae (center and edge), EPM, and bone and apatite standards. All values are in mean wt%. Calcium to phosphorous atomic (often referred to as molar) ratios are provided in the lower right corner. Note, in particular, the differences between tesserae and bone/apatite samples and between EPM and tesserae. Abbreviation: Tess-Ctr = Tessera center, Tess-Edge = Tessera edge.

Fig. 10 Elemental composition and Raman vibrational spectra of tessellated calcified cartilage and EPMs in skate *L. naevus*.
(A) Backscatter SEM imaging and elemental maps of calcium (Ca), magnesium (Mg), sodium (Na), oxygen (O), phosphorus (P) and sulfur (S) concentrations in different elasmobranch tissues; perichondrium (PC), tesserae (T), unmineralized cartilage (UC) and a tesserae-associated EPM. (B) Raman spectra of two different EPMs, tesserae, and uncalcified cartilage, as well as brushite and PMMA (embedding material) for comparison. (C) Ma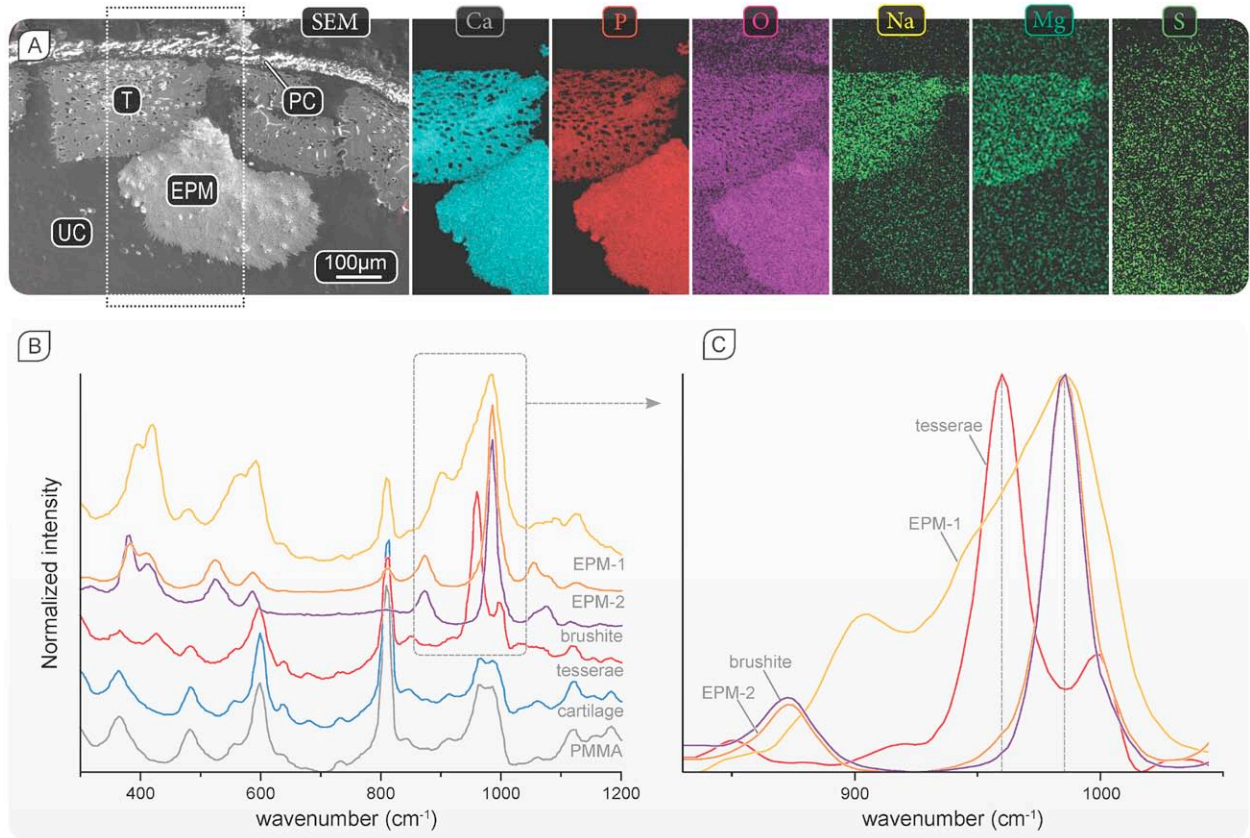gnification of the m1 spectral region of phosphates shown in the dashed gray box in (B); note the different position of the m1 phosphate peak for EPM regions relative to tesserae and the similarity between the brushite spectrum and that of EPM-2.

same grayscale value (i.e. mineral density) as tesserae in the same BSE image (Fig. 5). The mineral density of the EPM matrix never appeared to exceed the highest mineral density features in tesserae, the hypermineralized "spokes" reinforcing intertesseral joints, visible in BSE (Fig. 4B and 5G) (Seidel et al. 2016).

EPMs contain cells of similar size (~10–15 μm long) and density to the living chondrocytes in the surrounding unmineralized cartilage and to the lacunar spaces (housing cells) in tesserae (i.e. Fig. 5) (Dean et al. 2010). EPM cells, however, are uniformly dead and mineralized: note that, in contrast to the cells in the uncalcified cartilage and tesserae, EPM cells are visible in the BSE images in Fig. 5, due to their mineralization. The high mineral density of EPM cells is comparable to that of tesseral spokes (Seidel et al. 2016) and always exceeded that of the EPM body (e.g. Fig. 5). The cells within the lacunae of tesserae directly bordering the "stems" of the EPMs (i.e. flanking the intertesseral joints through

which EPMs passed) were also often hypermineralized (Fig. 5C).

The texture of the mineralized matrix in tesserae and EPMs is strikingly different. Whereas tesserae are characterized by a compact mineralized tissue with visible lines of accretive growth (Liese-gang lines; Fig. 5B, F; e.g. Kemp & Westrin, 1979 and Seidel et al. 2016), EPMs exhibit a brushstroke-like pattern of birefringent mineralized tissue, arranged in bundles that appear to be randomly oriented (Figs. 5 and 7). The mineralized margins of the EPMs splay into the surrounding UC matrix, resulting in the EPM-UC interface often having a "frayed" appearance, in contrast with the defined, smooth chondral margins of tesserae (Figs. 4 and 5).

Only in VK-stained samples, we observed arrays of black, ovoid granules (1–10 µm; Fig. 6A, B), haloing the "frayed" margin of EPMs. Granules were closely associated with UC chondrocytes, but it was unclear whether they were localized within or outside of cells (Fig. 6C). Granules were clustered into large masses directly along the EPM edges, with larger granules often appearing as conglom-erations of at least two smaller granules, and with granules becoming smaller and more sparse with increasing distance from EPMs (Fig. 6C). Granules were not observed when a VK protocol with shorter incubation time (illuminated for less than 5 min) was used.

The mineral phase of the EPM exhibits pronounced differences relative to that of tesserae, visible particularly in TEM micrographs (Fig. 8). In unstained sections of EPMs (Fig. 8A–C), we observed large single, elongated platelets (estimated to be ~500 x 250 x 100 nm in size from TEM images), aligning end to end in long strings. These crystal strings are embedded in an organic matrix, which is similar in appearance and with a similar SAED pattern to the uncalcified cartilage (Fig. 8F, G). This is reflected in the corresponding SAED patterns, which are characterized by scattered, isolated and very sharp spots, indicating that this phase is composed of micron-scale single crystals (Fig. 8E). The radi-ally integrated diffraction patterns cannot be unequivocally assigned to a specific calcium phosphate phase, but the large number of detected reflections and their small separation is compatible with low-symmetry CaP phases: brushite ($CaHPO_4 \cdot 2H_2O$) or monetite ($CaHPO_4$) or CPPD ($Ca_2P_2O_7 \cdot 2H_2O$) (Bjelle 1972; McCarty et al. 1966). Also, this phase appears to contain a higher amount of P and O than the tesseral mineral phase, and is depleted in Na and Mg, suggesting less elemental substitution (Figs. 9 and 10A). This observation is consistent with the single crystalline nature of the EPM mineral phase. Interestingly, the semi-quantitative compositional analysis of this phase reveals that it is characterized by a Ca/P ratio close to 1. This is compatible with brushite, monetite or CPPD, but the mineral phase of the EPM cannot be identified unambiguously by EDS alone.

Raman microspectroscopic data acquired on EPMs supported EDS and SAED findings (see below) that EPMs are comprised of a Ca and P-rich crystalline phases (Fig. 10B, C). A survey of Raman spectra collected from different EPMs showed two m1 phosphate peak shapes, either a broad peak (930–1020 cm-1; EPM-1 in Fig. 19B-C) or a narrow peak (~960–1010 cm-1; EPM-2 in Fig. 10B, C),

both with peak position at ~985 cm-1. The narrow peak closely resembled the m1 phosphate peak of brushite (Fig. 10B, C) (Casciani and Condrate, 1979; Penel et al. 1999). The shoulder of the broad m1 phosphate peak of EPM-1 could result from a convolution with a mineral phase similar to tesseral apatite (959 cm-1). The primary peak of synthetic CPPD (1037 cm-1) was not evident in EPM spectra. Monetite shares a similar strong Raman peak at ~983 cm-1 (Casciani and Condrate, 1980), however its full spectrum is not similar to the EPM spectra. The presence of this anhydrous calcium phosphate phase in EPMs is unlikely, as its in vitro crystallization occurs at 90º C (Casciani and Condrate, 1979).

In contrast to those obtained for EPMs, selected area electron diffraction (SAED) patterns obtained on tesserae showed several broad rings (see Fig. 8D), as typically observed for nanosized particles, and exhibited preferential orientation roughly parallel to the tessera's chondral edge. The position of the reflections in radially integrated patterns (not shown) is fully consistent with apatite, supporting findings from previous diffraction work on elasmobranch tesserae and vertebrae (Applegate 1967; Omelon et al. 2014; Urist, 1961, 1962). Furthermore, from the analysis of the angular dependence of the (002) apatite reflections, it can be inferred that the c crystallographic axis of the nanoparticles lies parallel to the collagen fibers, as found in other vertebrate hard tissues like bone (Ascenzi et al. 1979; Fratzl et al. 2004 and references within; Jaschouz et al. 2003) and mineralized turkey tendon (Bigi et al. 1988). The Ca/P atomic (often referred to as molar) ratios measured by EDS for the tesseral apatite (Fig. 9) range between 1.2 and 1.3, much smaller than the theoretical value for apatites (1.67) and lower than those reported for elasmobranch vertebrae (1.52; Urist, 1961) and bone apatites, the values of which have been reported to range from 1.5 to 1.85, depending on the sample preparation and analysis techniques used (e.g. Bigi et al. 1997; Grynpas et al. 1991; Landis and Glimcher, 1978; Legros et al. 1987; Mahamid et al. 2011; Obrant and Odselius 1985; Ravaglioli et al. 1996) However, the high content of sodium (Na) and magnesium (Mg), which can substitute for calcium (Ca) in the apatite lattice, can explain this difference. It is worth noting from Na and Mg distributions that the degree of substitution varies spatially within tessera, and, in particular, increases from the center to the margin (Fig. 9).

6.4 DISCUSSION

Endophytic masses —a form of ectopic cartilage calcification we describe for the first time in elasmobranch fishes— were observed in a variety of skeletal elements and species, from both sharks and batoids (rays and relatives). Intra- and inter-species EPM comparisons revealed general anatomical commonalities in EPM shape, size, ultrastructure, association with intertesseral joints, and incorporation of high-mineral-density chondrocytes. Even though endophytic masses are closely associated with tesserae —the primary and ubiquitous mineralized component of the skeleton— bordering their

chondral and lateral surfaces, their ultrastructure and crystallography differ significantly (Clement 1992; Kemp & Westrin, 1979; Peignoux-Deville et al. 1982; Seidel et al. 2016). Tesserae bear record of an accretive and periodic growth process, in the form of agglomerations of mineralized sphericles ("calcospherites") at their chondral and lateral margins, and internal banding of varying mineral density (Liesegang lines; Figs. 5B and 8G; see also Ørvig, 1951; Dean et al. 2015; Seidel et al. 2016 and references within). In contrast, EPMs are comprised of long strings of platelike crystals interspersed with scant volumes of a type-2 collagen-based matrix (Fig. 8G), similar to the surrounding uncalcified cartilage (Blumer et al. 2015; Enault et al. 2015). The organization of the crystals appears not to be linked to the collagen orientation in the cartilage. Although tesserae and EPMs are apparently both type-2 collagen-based tissues (Blumer et al. 2015; Enault et al. 2015), the differences in crystallite size and chemistry, and in the apparent mechanisms of tissue organization and mineral precipitation between them may explain why tesserae and EPMs were separated by unmineralized gaps and not fused (Fig. 8B). The striking mineralization pattern of EPMs and their non-ubiquity also argue that different mechanisms of skeletal cartilage mineralization underlie tesserae and EPM development.

6.4.1 EPM etiology

EPMs appear to be uncommon: we observed them in just three of the 14 hyomandibulae examined with microCT from several ages of round stingray *U. halleri*. The lack of mention of EPMs in previous literature is also conspicuous (but see Fig. 2 in Maisey, 2013, for what could be a non-tesserae-associated EPM in the jaw cartilage of the shark Mustelus). While the overall rarity of the EPMs raises the possibility that these features may be somehow produced by our sample preparation methods, as was recently reported with zinc oxide mineral precipitating in spider fang channels during dehydration (Politi et al. 2016), our experimental results suggest otherwise. Our control samples—incubated in either water, EtOH series or PFA—indicate that EPMs are not simply features resulting from dehydration or fixation. The presence of EPMs in intact, microCT-scanned hyomandibulae also argues that EPMs are not caused by cutting or trimming samples (e.g. by allowing materials from one tissue compartment anomalous access to another). That EPMs are naturally occurring features in living animals and not artifacts is further supported by their apparent integration into (rather than displacement and rupture of) surrounding tissues, as well as the consistency of EPM size, shape and appearance in a variety of species.

That we did not observe EPMs in any fresh dissected samples implies that they may have a different appearance in non-fixed tissue (e.g. may be transparent) and that they may simply be uncommon. Our microCT-investigated age series of hyomandibulae suggests that EPMs would be found in 21.4% (=3/14) of samples from the same portion of the skeleton and in varying frequency when present. This is, however, even more prevalent than CPPD crystal deposition in human knee

cartilage, which was observed in only 13% of elderly subjects in a large study of 608 cadaveric knees (Ryu et al. 2014). In that study, age, gender and degree of joint degeneration were strong predictors of CPPD deposition; additional work is necessary to determine whether EPM presence is correlated with similar factors.

The distinct texture of EPMs and their occurrence in regions that typically do not mineralize suggests that they could represent a failure of the processes that normally determine where mineralization occurs and where it is inhibited. Elasmobranch cartilage proteoglycans can inhibit mineral precipitation in vitro (Gelsleichter et al. 1995), and are broken down at skeletal mineralization fronts in vivo (via degradation and/or desulfonation of glycosaminoglycan chains; Takagi et al. 1984). Furthermore, matrix Gla protein (MGP), a binder of mineralization ions and inhibitor of soft tissue calcification (Luo et al. 1997), has been found adjacent to vertebral and tesseral mineralization fronts in blue sharks, Prionace glauca (Ortiz-Delgado et al. 2005). There is also growing indication that chondrocytes play a role in elasmobranch cartilage calcification by controlling their local environment via expression of mineralization inhibitors and promoters. Cells near tesserae appear to express the highest concentrations of MGP (inhibitor; Ortiz-Delgado et al. 2005), while also occupying regions of high concentration of polymers of phosphate (polyPs) and the enzyme alkaline phosphatase (ALP), which cleaves polyPs to increase local inorganic phosphorous ion concentration for mineralization (Omelon et al. 2014; Urist, 1962). Several authors have also described what are apparently cell-associated vesicles at the tesseral mineralization front (e.g. Bordat, 1988; Clement, 1992; Kemp & Westrin, 1979; Takagi et al. 1984), suggesting that cells may secrete a packaged, metastable mineral precursor into the extracellular matrix to be delivered to mineralizing areas and transformed into apatite.

These pieces of evidence imply that EPM formation could be favored under abnormal conditions that upset local tissue homeostasis. Ectopic mineralization could conceivably be triggered by a decrease in local proteoglycan content that allows mineralizing ions more access to collagen fibers (as proposed for some mammalian cartilage diseases; Gallagher et al. 2015; Kalya and Rosenthal, 2005; Kemp & Westrin, 1979), a change in chondrocyte health, or a decrease in pH below the neutral pH of elasmobranch body sera (see citations in Supplementary Table 4: Dean et al. 2015), since the calcium phosphate mineral suggested by our data (brushite) precipitates in acidic solutions (pH ~5; Galea et al. 2013; Shellis et al. 1997).

The argument that EPMs represent a disruption to local homeostasis is supported in particular by EPM-associated cells, which are "micropetrotic" (filled by hypermineralized material). Our data suggest that cells do not die from being encapsulated in mineralized EPM tissue (as with micropetrotic cells in bone; Carpentier et al. 2012; Frost, 1960; Remaggi et al. 1996). Rather it appears that cells need only come into contact or proximity with EPMs to become mineralized (Figs. 5H and 8G). EPM micropetrosis is also apparently not a function of animal age, in contrast to the micropetrosis described

recently for intratesseral chondrocytes in *U. halleri* (Seidel et al. 2016). Whereas mammalian cartilage and bone cells are known to die as a function of tissue damage (Cardoso et al. 2009; Martin et al. 2015; Verborgt et al. 2000), we saw no evidence of in vivo damage (e.g. clefts) in EPM- associated tesserae or unmineralized cartilage. Furthermore, the shape and size of partially-mineralized cells external but near to EPMs appeared otherwise similar to unaffected cells further away in the unmineralized carti-lage core.

EPM-adjacent cells, however —and not cells neighboring active tesseral mineralization fronts (i.e. chondral and intertesseral margins)— were the only ones associated with the von Kossa-positive granules that we observed during long (but not short) staining incubation times (Fig. 6). The gran-ules were not detectable in backscatter SEM (i.e. they were not mineralized) or in EDS, but were of similar sizes and shapes to the cell-associated vesicles previously hypothesized to be involved in elas-mobranch cartilage mineralization (Clement, 1992; Kemp & Westrin, 1979; Takagi et al. 1984). The delayed VK staining we observed could be due to sample preparation resulting in inorganic phosphates being freed from an unknown endogenous phospho-complex (e.g. via polyP degradation; Omelon et al. 2014). Even if granule staining is somehow artifactual (e.g. the result of the stain associating with organic material; see Puchtler and Meloan, 1978, 1985 and references within), their consistent place-ment within or in the vicinity of EPM-adjacent cells and their condensed morphologies indicate that elasmobranch chondrocytes and their pericellular environments undergo distinct changes in associa-tion with the development of EPMs.

6.4.2 EPMs in context

Although EPMs have not been previously documented, they resemble other ectopic tissues reported in elasmobranch fishes. Studies have noted mineralized fusions of tesserae (Applegate, 1967; Maisey, 2013), in some cases taking the form of massive "hypercalcified" masses on the perichondral side of the tesseral layer (Fig. 10 in Maisey, 2013), resulting in a stiff covering to the skeleton. It is not clear whether the "hypercalcified" masses also continued onto the chondral side of the tesseral layer. EPMs could represent an earlier stage in the formation of the massive hypercalcifications/ fusions described by Maisey (2013). Many authors have also observed pathologic, mineralized masses encasing portions of the vertebral column in sharks (Hoenig and Walsh, 1983; Huber et al. 2013; Officer et al. 1995; Porter et al. 2006), particularly in captive sandtiger sharks (Carcharias taurus) with spinal deformities (Fig. 11A), encasing sites of former vertebral fracture or dislocation (Fig. 11B–C) (Huber et al. 2013). This excessive mineralization occurs within the fracture gaps of damaged indi-vidual vertebrae (endophytic mineralization), but also outside the margin of the notochordal sheath (exophytic mineralization), with the latter being the source of mineral overgrowth that results in fusion of adjacent vertebrae.
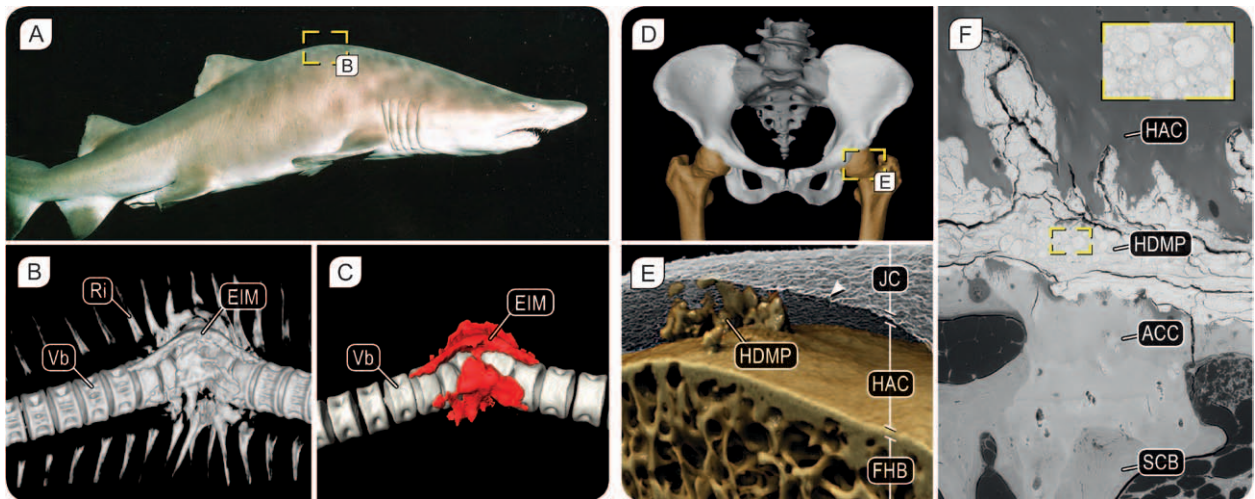
Fig. 11 Skeletal pathologies in vertebrates (cartilaginous fish and human).
(A) Photograph of a captive sandtiger shark (*Carcharias taurus*, Elasmobranchii) with spinal deformity (yellow frame). (B–C) Computed tomography imaging of spinal deformation from *C. taurus*, with exophytic idiopathic mineralization (EIM) associated with vertebrae (Vb) and ribs (Ri). (D) CT scan of a human pelvis with lumbar vertebrae and femora, indicating the location of joint shown in image E (yellow frame) (E) Micro-computed tomography image of hyperdense mineralized protrusions (HDMP) protruding into the hyaline articular cartilage HAC covering a femoral head (FHB) with advanced osteoarthritis. The HAC has been rendered transparent to visualise HDMPs, and the arrowhead indicates the surface of the HAC within the joint capsule (JC). (F) Backscatter SEM image showing the different mineral densities of subchondral bone (SCB), articular calcified cartilage (ACC) and HDMPs, and the globular ultrastructure of the latter.

Previous studies of elasmobranch "hypercalcified" masses and vertebral calluses did not characterize ultrastructure or mineral phase and so cannot be compared with our data. However, a commonality of EPMs, "hypercalcified" masses and vertebral calluses is that they all involve the fusion of mineralized portions of skeletal elements. The cause of "hypercalcified" masses is unclear. The descriptions of vertebral calluses, however, suggest that they are specific responses to vertebral column damage (e.g. subluxation), perhaps triggered by local injury to the notochordal sheath (Huber et al. 2013). Similarly, but on a smaller scale, EPMs could be a response to damage, either to tesserae, the surrounding soft tissues (i.e. the unmineralized cartilage and perichondrium) or to the cells occupying the narrow gaps between tesserae, forming a mineralized and heterogeneous matrix to span and stabilize fracture gaps to facilitate repair, as in bone calluses (Fratzl and Weinkamer, 2007; Hoerth et al. 2014). In this way, ectopic mineralization could actually serve an adaptive function, stabilizing lesions and containing the spread of damage or infection, as has been suggested for inflammation-associated, pathological calcification in mouse and human vasculature (Abdelbaky et al. 2013; Abedin et al. 2004; Aikawa et al. 2007). To date, however, evidence suggests that elasmobranch skeletons cannot resorb or remodel tesserae in response to damage (e.g. in vivo experimental fracture of skeletal elements; Ashhurst, 2004; Clement,

1986), and that those calluses that do form in damaged tessellated tissue are fibrous, not mineralized (Ashhurst, 2004).

From an anatomical perspective, EPMs are perhaps more similar to mammalian joint destructive pathologies, such as chondrocalcinosis (e.g. pseudogout) and high density mineralized protrusions (HDMPs). Chondrocalcinosis describes the deposition of calcium salts —brushite, calcium pyrophosphate (CPP), and/or basic calcium phosphate (BCP)— within joint articular cartilage or fibrocartilage and is often associated with the development and progression of osteoarthritis (Kalya and Rosenthal, 2005; McCarty et al. 1966). In chondrocalcinotic cartilage, as with elasmobranch EPMs, poorly formed, mineralized masses form within the extracellular matrix and are visible using radiographic techniques (Barskova et al. 2013; McCarty et al. 1966). Although we do observe evidence of brushite (and possibly other CaP minerals) in EPMs, we could not conclude that matrix proteoglycans or calcium-binding proteins have been altered in EPM production, as would be the case in chondrocalcinosis (Kalya and Rosenthal, 2005). Yet, the lack of chondrocyte hypertrophy and of visible damage to the matrix and fibers surrounding cells —hallmarks of chondrocalcinosis— illustrate the etiologies of EPMs and chondrocalcinotic cartilage differ at fundamental levels.

HDMPs, described recently in human and racehorse joint cartilage, are abnormal mineralized protrusions of the calcified cartilage layer surmounting the bone, jutting into the superficial unmineralized hyaline cartilage (Fig. 11C, D) (Boyde et al. 2011, 2014). It appears that HDMPs form in the cracks in the subchondral plate that follow abnormal cartilage matrix stiffening, which can be caused by age- or disease-related modifications of the proteoglycans that typically protect collagens and inhibit mineralization of cartilage (Gallagher et al. 2015). Like EPMs, HDMPs exhibit comparatively high mineral density and grow endophytically into uncalcified cartilage. However, their presence in clearly damaged areas and their structure —lacking cells and comprised of dense globular mineral accretions rather than large, individual crystals— argue that their similarity with EPMs ends there.

6.5 CONCLUSIONS

EPMs are a distinct and comparatively rare mineralized tissue in elasmobranch skeletons, that differ considerably from tesserae in their ultrastructure and chemistry. Although the presence of EPMs in multiple species argues for their being a natural part of elasmobranch skeletal biology, their apparent inconsistency of location (i.e. not only in high-load areas) and the lack of coexisting tissue damage suggests they are a result of conditions that are not universal.

We conclude that a local breakdown of CaP mineralization inhibition processes is a likely cause for EPM formation. The micropetrotic cells within and bordering EPMs and the observation of von Kossa-positive granules haloing EPM-adjacent chondrocytes suggest that changes in local tissue

homeostasis may precede EPM formation, as has been shown for some joint destruction diseases in mammals. Although there was no visible damage or degradation of the unmineralized cartilage surrounding EPMs, EPM ultrastructure and crystallography suggest multiple similarities with mineral deposition disorders in elasmobranch but also mammalian cartilage (e.g. chondrocalcinosis associated with osteoarthritis and HDMPs). Elasmobranch cartilage could therefore prove a useful and novel comparative model for joint destructive diseases and osteoarthritic micropetrosis.

Characterization of EPM development and surrounding matrix properties will be vital to developing elasmobranch cartilage as a model, perhaps in skates (Rajidae), where EPMs appear to be quite common and particularly prominent when present (e.g. Fig. 3). Further studies could focus in particular on biochemical changes that characterize the transition from unmineralized to mineralized cartilage in elasmobranchs, during apatite formation in tesserae, as well as during growth of EPMs. Parameters to investigate include changes in proteoglycan and polyP content, pH, and ALP activity at both EPM and tesserae mineralization fronts.

6.6 ACKNOWLEDGEMENTS

6.7 REFERENCES

Please see the concatenated reference list at the end for all citations provided within this thesis.

7. SUMMARY

This thesis is dedicated to the development and ultrastructure of skeletal tissues from sharks, rays and relatives (elasmobranchs), whose endoskeletons are unique in their anatomy and composition among vertebrates. Elasmobranchs' skeletal tessellated cartilage exhibits a complex arrangement of soft and hard tissues that interact with one another under permanent, repetitive loads while the whole system is growing. It is a natural tessellation combining many fascinating aspects of growth, form and mechanics that can be of interest to scientists related to the fields of skeletal biology, cartilage, tissue biomineralization and also engineering.

The primary goal of this study was to characterize tesserae from round stingray *Urobatis halleri* and use them as a model system for distilling features of tesserae growth and anatomy to provide a window into tessellated cartilage in elasmobranchs in general. We used high-resolution materials characterization and biological techniques, including synchrotron and laboratory µCT, BSE, SAED, EDX, TEM, Raman spectroscopy, IHC, Histology and PLM to investigate both mineralized sections of tesserae and the underlying and associated soft tissues in demineralized sections. Based on ontogenetic series of tessellated cartilage obtained from the same skeletal elements we defined growth phases in *U. halleri* and important developmental time points, for example when tesserae start to mineralize, come in contact, and when distinct intratesseral features form. One strength of this thesis lies in the presentation of constant perspectives and section planes of tesserae, providing the first 3-dimensional understanding of tesserae composition and ultrastructure, and allowing for cross-study correlations of images gathered with different techniques. These insights provide a holistic view of elasmobranch tessellated cartilage from *U. halleri*, but also bring to light ultrastructural commonalities while outlining the variation of tesserae anatomy across shark and ray species.

Tesserae start to form as individual, mineralized platelets in the cartilage core and grow in all directions by accretion of new mineral to their existing surfaces. They grow, eventually come in contact, but don't fuse and show no obvious overlapping or interdigitation. There is no evidence for remodeling in tesserae of *U. halleri* as patterns of intersecting lines similar to those of secondary osteons in bone are absent, supporting the theory of tesserae as a deposition-only model. Intratesseral features, such as spokes and Liesegang lines, visible as lines of varying mineral density in BSE, reflect the successive deposition of mineral and growth of tesserae. Spokes, described here for the first time, are comprised of stacked laminae of oscillating mineral density parallel to the edges of contact zones of abutting tesserae. If cracks occurred during preparation of our samples (e.g. due to sample block dehydration), they were found predominantly in spoked regions and exhibited characteristic zig-zag morphologies (pers. observation). It is unclear whether such cracks form in life, but this observation suggests that

spoke laminae could be important for dissipating the energy at the tips of cracks, and therefore that spokes represent a successful strategy to link both growth and mechanical integrity.

Although tesserae start to develop surrounded by cartilage, they are not just blocks of calcified cartilage patterned on type-II collagen (Coll II), the major collagen forming cartilage. In fact, tesserae are patterned on at least 3 different types of collagen, Coll I, II and X. Tesserae exhibit a largely bipartite anatomy comprised of an upper cap, patterned on type-I collagen, and a lower body zone associated with the cartilage core, both patterned on type-II collagen. Type-X collagen, typically a marker for hypertrophic chondrocytes in mineralizing growth plate calcified cartilage in vertebrate long bones (Gannon et al. 1991; Shen, 2005), was expressed heavily at the cap mineralization front, in a supratesseral layer of unmineralized cartilage (Coll II) interspersed with Coll I fibers. The lack of cell hypertrophy in the skeleton of *U. halleri*, however, suggests that Coll X expression may be evolutionarily linked to vertebrate tissue calcification rather than cell hypertrophy. Cells were embedded in tesserae in a network of lacunar spaces, and appeared to be intact chondrocytes. Our findings argue that elasmobranch chondrocytes are capable of secreting both cartilage- and a bone-like matrix, in line with recent theories for mammalian systems that chondrocytes can transform directly into bone (i.e. Coll I) matrix-secreting cells in developing long bone growth plates and fracture calluses (reviewed in Hinton et al. 2017).

Our description of endophytic masses (EPMs) outlines a possible response to damage and shift away from homeostatic equilibrium in tessellated cartilage. This aberrant type of cartilage calcification is closely associated with tesserae, but exhibited different anatomical and material characteristics compared to tesserae, demonstrating them to be distinct tissues, likely governed by different growth mechanisms. Although both tesserae and EPMs are built on a type-II collagen-based matrix, EPMs exhibit much larger crystals, aligned in strings, and cells that were in contact with EPMs or embedded in EPM tissue are dead. The latter fact in combination with the lack of periodic growth lines (Liesegang lines, characteristic for tesserae) in EPMs hints at two distinct pathways of cartilage calcification. It is therefore plausible thatelasmobranchs' tessellated cartilage could prove a useful and novel comparable model for joint destructive diseases, such as osteoarthritic micropetrosis. Further studies could focus on the transition from unmineralized to mineralized cartilage in elasmobranchs, in particular on the changes of proteoglycan and polyP content, pH, and ALP activity at cartilage mineralization fronts.

7.1 Open questions & Outlook

My dissertation opens several lines of further enquiry relating to vertebrate mineralized tissue structure-functional relationships, the developmental origin of the tessellated pattern and local control of mineralization of shark and ray cartilage. In the following I discuss, what became in my eyes during this study the two most intriguing questions, and also what the major implications of the findings mean to cartilage biology in vertebrates in general:

1. Why does the mineralization only occur on the surface of the skeleton?

Tissue mineralization is typically a controlled process of organic fiber and biomineral deposition and interaction, where an organic framework dictates the organization of the mineralized tissue. In the first study of this thesis, we have shown that a network of dense, aligned fibers links and probably guides the lateral growth of tesserae in adult elasmobranchs. However, in pre-tessellate *U. halleri* specimens (i.e. where tesserae had not begun to form yet) such a fibrous network is absent (or at least not apparent). This suggests that it develops later, maybe coincidentally with tesserae, and therefore, cannot be the driving factor for the initiation of the mineralization. If structural differences between the core and the skeletal periphery (where tesserae form) aren't causing the initial mineral precipitation, what then?

In elasmobranchs, the mineralization of the cartilage matrix appears to be linked to the presence of ALP, a known enzymatic marker for biomineralization (Omelon et al. 2014; Dean et al. 2016). Lorch (1949) and Eames et al. (2007) showed that ALP expression occurs only on the surface of the skeletal elements, in the same regions where tesserae form, prior to cartilage calcification. Therefore, understanding why the expression of ALP is restricted to the cartilage surface could give us clues to why there is only a layer of mineralized cartilage instead of a fully calcified skeleton. Based on my work and data available from the literature I discuss possible explanations for when mineralization starts and its restriction to the surface of the skeleton.

First, our μCT data suggests that stress distributions in the skeleton could dictate where and when mineral forms. In whole skeletal elements from young animals the mineralization doesn't start simultaneously on the surface of the skeletal elements. Tesserae appear first at convex surfaces of the hyomandibulae in histotroph animals, around the time of hatching from the egg case, which is the start of free swimming and increased movement. Given the orientation of the hyomandibula in the head of the animal and its role in the feeding apparatus, the convex regions are likely loaded earlier and to a higher degree, in both compression and tension, compared to the more planar regions. This observation may hint at some form of mechanically induced ALP expression and subsequent mineralization.

Secondly, the appearance of mineralization only in the periphery of the skeleton could be a response to signals from the overlying perichondrium or from cells in the outer region of the skel-

eton, perhaps the spindle-shaped cells in the supratesseral layer of unmineralized cartilage bordering the perichondrium. This is supported by the following: 1) ALP expression occurs in the same region as Coll X, the latter was only observed in the narrow supratesseral layer between tesserae and the perichondrium, and both proteins often occur in co-existence in vertebrate cartilage mineralization. Neither Coll X nor ALP was expressed deeper in the cartilage matrix, which forms the unmineralized cartilage core and 'never' mineralizes. This suggests an important role of the spindle shaped cells in the supra-tesseral layer for tesserae formation, and the coupling of ALP and Coll X in vertebrate skeletal tissue mineralization when Coll I fibers (in the supratesseral cartilage layer) are present.

2) There appears to be a successive spatio-temporal expression pattern of ALP during the development of elasmobranch skeletal tissues. In pre-tessellate animals from a shark species, ALP expression was first observed outside the cartilaginous skeleton in the perichondrium, then in the supratesseral cartilage layer, and later in the region of the future tesseral layer (Lorch, 1949). This could be hinting at a signaling cascade, initializing ALP expression and subsequent skeletal mineralization, which is advancing from the outside of the skeleton towards the skeletal core. Understanding the factors that control these signaling cascades and the restriction of the mineralization to the surface and not the core of the skeleton and the perichondrium, will require in vivo investigations, particularly in the ontogenetic stages associated with the initial formation of tesserae, as outlined in this dissertation.

2. What is the reason for the tiling of this mineralized layer?

Although our ultrastructural characterization of tessellated cartilage from young and adult animals of *U. halleri* offers many insights into the sequence of developmental processes, our understanding of the role of cells in cartilage matrix mineralization and turnover is still very narrow. There is some evidence that, similar to the development of a mineralized surface layer, the presence of ALP is linked to the organization of the tiling pattern as well. Eames et al. (2007) showed that, in pre-tessellate animals, distinct groups of chondrocytes express ALP at the skeletal surface leading to a patchy distribution of ALP predicting the location of tesserae. We did not observe morphological differences between the cells in the periphery in pre-tessellate specimens of *U. halleri*, however, the fact that some cells express ALP whereas others don't is puzzling. These ALP-producing 'founder cells' could be the result of a developmental process, for example, where mesenchymal cells differentiate into two distinct cell populations at the skeletal surface, which do not differ in morphology, but are fundamentally different in the products they synthesize and perhaps their fates in the adult skeleton (see below). Alternatively, the chondrocytes in the skeleton do not differ fundamentally, as suggested by our morphological observations, but focal external stimuli (as discussed above, e.g. growth factors or matrix alterations such as changes in proteoglycan, water content or pH) result in a cell response,

ALP expression and subsequent calcification of elasmobranch skeletal cartilage.

Whether cells are different or not, they certainly appear to behave differently according to their local environment and single cells may change their role during the process of tissue mineralization. Cells at the mineralization fronts of tesserae secrete ALP into the surrounding matrix until they become incorporated into tesserae, at which point they apparently cease ALP (and Coll X) production (Omelon et al. 2014; this study). This change may actively suppress mineralization, resulting in a surrounding layer of unmineralized matrix between cells and the lacunar wall that encases them. The factors mediating this switch in function are unknown, but could indicate the ability of tessellated cartilage chondrocytes to sense external factors, mechanical (e.g. pressure) or chemical (e.g. GAGs, PGs), or both.

The ability for cells to sense and respond to local stimuli is also suggested by the persistence of unmineralized tissue in intertesseral joints. Intertesseral cells may regulate the growth of intertesseral fibers (e.g. via a combination of collagen synthesis and MMP expression) and also prevent tesserae fusion, by producing cartilage matrix in the joints, as well as matrix mineralization inhibitors. It is intriguing to consider that non-ALP producing cells from the pre-tessellate skeleton (i.e. 'non-founder cells') may be pre-destined to become intertesseral joint cells, always involved with non-mineralizing regions of the skeleton (e.g. 'gaps' between tesserae). Regardless of the origin of intertesseral joint cells, the spatial patterning of mineralizing and non-mineralizing zones (and subsequent formation of tesserae and joints) is surely a deciding factor in the large variation we observed in tesseral shapes across species and demands further study.

3. What does the elasmobranch skeleton teach us about the biology of cartilage in general?

These open questions illustrate our limited knowledge of the development, structure and variation in skeletal tissues in sharks, rays and relatives. This dissertation, however, also demonstrates the value of studies investigating non-traditional systems that are alternatives to current model systems or species. Broadening our perspectives in this way ensures that we don't become too biased in our assumptions of how endoskeletons grow, are structured and deal with damage. For example, our studies of elasmobranch collagens and tesserae ultrastructure demonstrate the dangers of assuming that cartilage mineralization can only occur according to the axioms of mammalian cartilage biology, requiring a cascade of chondrocyte differentiation events leading to hypertrophy, mineralization and cell death.

Our data suggest that chondrocytes control tesserae mineralization to remain alive and intact when embedded in tesserae. This is supported by the maintenance of a patent network connecting chondrocyte lacunae in tesserae, similar to the osteocyte lacuno-canalicular network in bone. The necessity of the lacuna-canalicular network in tesserae remains a mystery, but suggests cells may somehow communicate with one another and/or monitor their surrounding environment. As chondrocytes in mammalian skeletons are not known to build such networks, elasmobranch skeletons may prove useful

models for chondrocyte potential, beyond their known roles in mammalian cartilage. Development of such a model system is timely, given growing support for the idea that mammalian chondrocytes do not always die in mineralization, but can contribute directly to the pool of bone (Coll I) matrix-secreting cells (reviewed in Hinton et al., 2017), challenging to the dogma of chondrogenesis and osteogenesis as separate processes.

Multi-functionality of elasmobranch chondrocytes is further suggested by the apparent variation in their protein expression and the composition of their surrounding matrix. Elasmobranch chondrocytes can be found in matrices based on a single collagen type or on complex mixes of collagens (compare the cartilage core, supratesseral layer and intertesseral joint matrices) and can show either intracellular, extracellular or no Coll X expression. The differing roles but gross morphological similarity of elasmobranch chondrocyte populations sets a research stage for exciting novel investigation into the cell signals that drive variable protein expression and cell fate decisions. Also, the fact that only some elasmobranch chondrocytes expressed Coll X, but none exhibited hypertrophy, indicates that these cells could act as interesting cell culture models, providing unique insights into unrecognized chondrocyte-mediated mechanisms of tissue growth (without the massive volume enlargements of hypertrophic chondrocytes that determine growth rates of skeletal elements in mammals) and mineralization (without what is believed to be an obligate relationship between Coll X expression and cell hypertrophy).

In these ways, elasmobranch tessellated cartilage offers a unique perspective on cartilage development, longevity and mechanics and could prove a useful model system, providing fresh perspectives on vertebrate skeletal health and disease.

8. REFERENCES

Abdelbaky A, Corsini E, Figueroa AL, et al. (2013). Focal arterial inflammation precedes subsequent calcification in the same location: a longitudinal FDG-PET/CT study. Circ Cardiovasc Imaging 6, 747–754.

Abedin M, Tintut Y, Demer LL, (2004). Vascular calcification. Arterioscler Thromb Vasc Biol 24, 1161–1170.

Adams SL, Pallante KM, Niu Z, et al. (1991). Rapid induction of type X collagen gene expression in cultured chick vertebral chondrocytes. Exp Cell Res 193, 190–197.

Aikawa E, Nahrendorf M, Sosnovik D, et al. (2007). Multimodality molecular imaging identifies proteolytic and osteogenic activities in early aortic valve disease. Circulation 115, 377–386.

Allerstorfer D, Longato S, Schwarzer C, et al. (2010). VEGF and its role in the early development of the long bone epiphysis. J Anat 216, 611–624.

Álvarez J, Costales L, Serra R, et al. (2005). Expression patterns of matrix metalloproteinases and vascular endothelial growth factor during epiphyseal ossification. J Bone Miner Res 20, 1011–1021.

Applegate SP, (1967). A survey of shark hard parts. In: Sharks, Skates and Rays. (eds Gilbert PW, Mathewson RF, Rall DP), pp. 37–66. Maryland: Johns Hopkins Press.

Ascenzi A, Bonucci E, Generali P, et al. (1979). Orientation of apatite in single osteon samples as studied by pole figures. Calcif Tissue Int 29, 101–105.

Ashby MF, Gibson LJ, Wegst U, et al. (1995). The mechanical properties of natural materials. I. Material property charts. In: Proceedings of the Royal Society of London A: Mathematical, Physical and Engineering Sciences. The Royal Society, 123–140.

Ashhurst DE, (2004). The cartilaginous skeleton of an elasmobranch fish does not heal. Matrix Biol 23, 15–22.

Atkins A, Dean MN, Habegger ML, et al. (2014). Remodeling in bone without osteocytes: Billfish challenge bone structure– function paradigms. Proc Natl Acad Sci 111, 16 047–16 052.

Bargmann W, (1939). Zur Kenntnis der Knorpelstrukturen. Untersuchungen am Skeletsystem von Selachiern. Zeitschrift für Zellforschung und Mikroskopische Anatomie, Abteilung A 29, 405–424.

Barskova VG, Kudaeva FM, Bozhieva LA, et al. (2013). Comparison of three imaging techniques in diagnosis of chondrocalcinosis of the knees in calcium pyrophosphate deposition disease. Rheumatology (Oxford) 52, 1090–1094.

Benzer P, 1944. Morphology of calcification in *Squalus acanthias*. Copeia 1944, 217–224.

Beresford WA, (1981). Chondroid Bone, Secondary Cartilage and Metaplasia. The American Journal of Surgical Pathology 5, 405.

Bigi A, Ripamonti A, Koch M, et al. (1988). Calcified turkey leg tendon as structural model for bone

mineralization. Int J Biol Macromol 10, 282–286.

Bigi A, Cojazzi, G, Panzavolta, S, et al. (1997). Chemical and structural characterization of the mineral phase from cortical and trabecular bone. J Inorg Biochem 68, 45–51.

Bjelle AO, (1972). Morphological study of articular-cartilage in pyrophosphate arthropathy – (chondrocalcinosis articularis or calcium pyrophosphate dihydrate crystal deposition disease). Ann Rheum Dis 31, 449–456.

Blumbach K, Niehoff A, Paulsson M, et al. (2008). Ablation of collagen IX and COMP disrupts epiphyseal cartilage architecture. Matrix Biol 27, 306–318.

Blumer MJF, Hausott B, Schwarzer C, et al. (2012). Role of tartrate-resistant acid phosphatase (TRAP) in long bone development. Mech Dev 129, 162–176.

Blumer M, Seidel R, Pechriggl E-J, et al. (2015). Cartilage or bone? Collagens in "cartilaginous" fish skeletons answer an old question. FASEB J 29.

Bobacz K, Erlacher L, Smolen J, et al. (2004). Chondrocyte number and proteoglycan synthesis in the aging and osteoarthritic human articular cartilage. Ann Rheum Dis 63, 1618–1622.

Bonewald LF, (2011). The Amazing Osteocyte. J Bone Miner. Res. 26, 229–238. doi:10.1002/jbmr.320

Boot-Handford RP, Tuckwell DS, (2003). Fibrillar collagen: the key to vertebrate evolution? A tale of molecular incest. Bioessays 25, 142–151.

Bordat C, (1988). Les cartilages calcifiés de la petite roussette (*Scyliorhinus canicula* L., Chondrichthyens): Histologie et ultrastructure. Can J Zool 66, 1432–1445.

Bormuth, H., 1933. Die trajektoriellen Strukturen im Knorpel der Haifische auf Grund von Untersuchungen im polarisierten Lichte. Cell Tissue Res 17, 767–797.

Boyde A, Hobdell MH, (1968). Scanning electron microscopy of lamellar bone. Z Zellforsch 93, 213–231.

Boyde A, Jones SJ, (1968). Scanning electron microscopy of cementum and Sharpey fibre bone. Z Zellforsch 92, 536–548.

Boyde A, Mccorkell FA, Taylor GK, et al. (2014). Iodine vapor staining for atomic number contrast in backscattered electron and X-ray imaging. Microsc Res Tech 77, 1044–1051.

Boyde A, Davis GR, Mills D, et al. (2014). On fragmenting, densely mineralised acellular protrusions into articular cartilage and their possible role in osteoarthritis. J Anat. 225, 436–446.

Boyde A, Riggs CM, Bushby AJ, et al. (2011). Cartilage damage involving extrusion of mineralisable matrix from the articular calcified cartilage and subchondral bone. Eur. Cell Mater. 21, 470–478.

Brown EH, Lehr JR, Smith JP, et al. (1963). Preparation and characterization of some calcium pyrophosphates. J Agric Food Chem. 11, 214–222.

Busse B, Djonic D, Milovanovic P, et al. (2010). Decrease in the osteocyte lacunar density accompanied by hypermineralized lacunar occlusion reveals failure and delay of remodeling in aged human

bone. Aging Cell 9, 1065–1075.

Cardoso L, Herman BC, Verborgt O, et al. (2009). Osteocyte apoptosis controls activation of intracortical resorption in response to bone fatigue. J Bone Miner Res. 24, 597–605.

Carpentier VT, Wong J, Yeap Y, et al. (2012). Increased proportion of hypermineralized osteocyte lacunae in osteoporotic and osteoarthritic human trabecular bone: implications for bone remodeling. Bone 50, 688–694.

Casciani F, Condrate Sr. RA, (1979). The vibrational spectra of brushite, CaHPO4_2H2O. Spectrosc. Lett. 12, 699–713.

Casciani F, Condrate RA, (1980). The Raman spectrum of monetite, CaHPO4. J Solid State Chem. 34, 385–388.

Chen S, Fu P, Cong R, et al. (2015). Strategies to minimize hypertrophy in cartilage engineering and regeneration. Genes & Diseases 2, 76–95. doi:10.1016/j.gendis.2014.12.003

Chung KS, Park HH, Ting K, et al. (1995). Modulated expression of type X collagen in the Meckel's cartilage with different developmental fates. Developmental Biology 170, 387–396.

Clement JG, (1986). Development, structure and composition of chondrichthyan skeletal tissues. PhD Thesis. London: University of London, 1986.

Clement JG, (1992). Re-examination of the fine structure of endoskeletal mineralization in Chondrichthyans: Implications for growth, ageing and calcium Homeostasis. Mar. Freshw. Res. 43, 157–181.

Cole MBJ, (1982). Morphology of the interlacunar network in four sites of hyaline cartilage of neonatal, juvenile, and adult rats. Clinical Orthopaedics and Related Research 170, 277.

Cole AG, (2011). A Review of Diversity in the Evolution and Development of Cartilage: the Search for the Origin of the Chondrocyte. Eur Cell Mater 21, 122–129.

Compagno LJ, (1988). Sharks of the order Carcharhiniformes, Princeton University Press Princeton, New Jersey.

Conrad G, Kelly P, von der Mark K, et al. (1981). A comparative study of elasmobranch corneal and scleral collagens. Exp Eye Res 32, 659–672.

Cooper KL, Oh S, Sung Y, et al. (2013). Multiple phases of chondrocyte enlargement underlie differences in skeletal proportions. Nature 495, 375–378.

Currey JD, (1999). The design of mineralised hard tissues for their mechanical functions. Journal of Experimental Biology 202, 3285–3294.

Currey JD, (2002). Bones: Structure and Mechanics. Princeton: Princeton University Press.

Currey JD, (2008). Collagen and the Mechanical Properties of Bone and Calcified Cartilage, in: Springer US, Boston, MA, pp. 397–420.

Currey JD, Dean MN, Shahar R, (2016). Revisiting the links between bone remodelling and osteocytes: insights from across phyla. Biol Rev Camb Philos Soc 225, 62.

Daniel JF, (1922). The elasmobranch fishes. University of California Press.

Dean MN, Huber DR, Nance HA, (2006). Functional morphology of jaw trabeculation in the lesser electric ray *Narcine brasiliensis*, with comments on the evolution of structural support in the Batoidea. J Morphol 267, 1137–1146.

Dean MN, Summers AP, (2006). Mineralized cartilage in the skeleton of chondrichthyan fishes. Zoology 109, 164–168.

Dean MN, Gorb SN, Summers AP, et al. (2008). A cryoSEM method for preservation and visualization of calcified shark cartilage (and other stubborn heterogeneous skeletal tissues). Micros Today 16, 48–50.

Dean MN, Mull CG, Gorb SN, et al. (2009). Ontogeny of the tessellated skeleton: insight from the skeletal growth of the round stingray *Urobatis halleri*. J Anat 215, 227–239.

Dean MN, Socha JJ, Hall BK, et al. (2010). Canaliculi in the tessellated skeleton of cartilaginous fishes. J Appl Ichthyol 26, 263– 267.

Dean MN, (2011). Cartilaginous fish skeletal tissues. In: Farrell AP (Ed.), Encyclopedia of Fish Physiology. Academic Press, San Diego, pp. 428–433.

Dean MN, Ekstrom L, Monsonego-Ornan E, et al. (2015). Mineral homeostasis and regulation of mineralization processes in the skeletons of sharks, rays and relatives (Elasmobranchii). Semin Cell Dev Biol 46, 51–67.

Denhardt, D.T., Guo, X., 1993. Osteopontin: a protein with diverse functions. FASEB J 7, 1475–1482.

Dettmeyer R, (2011). Forensic histopathology: fundamentals and perspectives, Springer Science & Business Media.

Dingerkus G, Séret B, Guilbert E, (1991). Multiple prismatic calcium phosphate layers in the jaws of present-day sharks (Chondrichthyes; Selachii). Experientia 47, 38–40.

Dirckx N, Hul M, Maes C, (2013). Osteoblast recruitment to sites of bone formation in skeletal development, homeostasis, and regeneration. Birth Defects Research Part C: Embryo Today: Reviews 99, 170–191.

Donoghue PCJ, Sansom IJ, Downs JP, (2006). Early evolution of vertebrate skeletal tissues and cellular interactions, and the canalization of skeletal development. Journal of Experimental Zoology Part B: Molecular and Developmental Evolution 306, 278–294.

Duro-Royo J, Zolotovsky K, Mogas-Soldevila L, Varshney S, Oxman N, Boyce MC, Ortiz C, (2015). MetaMesh: A hierarchical computational model for design and fabrication of biomimetic armored surfaces. Computer-Aided Design 60, 14–27. doi:10.1016/j.cad.2014.05.005

Eames BF, Allen N, Young J, et al. (2007). Skeletogenesis in the swell shark *Cephaloscyllium ventriosum*. J Anat 210, 542–554.

Eames BF, Amores A, Yan Y-L, et al. (2012). Evolution of the osteoblast: skeletogenesis in gar and zebrafish. BMC Evol Biol 12.

Egerbacher M, Helmreich M, Mayrhofer E, et al. (2006). Mineralisation of the hyaline cartilage in the small-spotted dogfish *Scyliorhinus canicula* L. Scripta Medica (BRNO) 79, 199– 212.

Enault S, Muñoz DN, Silva WTAF, et al. (2015). Molecular footprinting of skeletal tissues in the catshark *Scyliorhinus canicula* and the clawed frog *Xenopus tropicalis* identifies conserved and derived features of vertebrate calcification. Front Genet 6, 283.

Farnum CE, Lee R, O'Hara K, et al. (2002). Volume increase in growth plate chondrocytes during hypertrophy: the contribution of organic osmolytes. Bone 30, 574–581.

Ferguson VL, Bushby AJ, Boyde A, (2003). Nanomechanical properties and mineral concentration in articular calcified cartilage and subchondral bone. Journal of anatomy 203, 191–202.

Fratzl P, 2003. Cellulose and collagen: from fibres to tissues. Current Opinion in Colloid & Interface Science 8, 32–39.

Fratzl P, Gupta HS, Paschalis EP, et al. (2004). Structure and mechanical quality of the collagen–mineral nano-composite in bone. J Mater Chem 14, 2115–2123.

Fratzl P, Weinkamer R, (2007). Hierarchical structure and repair of bone: deformation, remodelling, healing. In: Self Healing Materials. Springer Series in Materials Science, Springer, Netherlands, Dordrecht, pp. 323–335.

Fratzl P, (2008). Collagen. Springer Science & Business Media.

Fratzl P, Kolednik O, Fischer,FD, et al. (2016). The mechanics of tessellations – bioinspired strategies for fracture resistance. Chem Soc Rev 45, 252–267.

Frost HM, (1960). Micropetrosis, J Bone Joint Surg Am 42-A, 144–150.

Galea L, Bohner M, Thuering J, et al. (2013). Control of the size, shape and composition of highly uniform, non-agglomerated, sub-micrometer beta-tricalcium phosphate and dicalcium phosphate platelets. Biomaterials 34, 6388–6401.

Gallagher JA, Ranganath LR, Boyde A, (2015). Lessons from rare diseases of cartilage and bone. Curr Opin Pharmacol 22, 107–114.

Gannon JM, Walker G, Fischer M, et al. (1991). Localization of type-x collagen in canine growth plate and adult canine articular-cartilage. J Orthop Res 9, 485–494.

Gelsleichter JJ, Musick JA, van Veld P, et al. (1995). Proteoglycans from the vertebral cartilage of the clearnose skate, *Raja eglanteria*: inhibition of hydroxyapatite formation. Fish Physiol Biochem 14, 247–251.

Geyer G, Linss W, (1978). Toluidine blue staining of cartilage proteoglycan subunits. Acta histochemica 61, 127–134.

Gibson GJ, Bearman CH, Flint MH, (1986). The immunoperoxidase localization of type X collagen in chick cartilage and lung. Collagen and Related Research 6, 163–184.

Grynpas MD, Alpert B, Katz I, et al. (1991). Subchondral Bone in Osteoarthritis. Calcif Tissue Int 49, 20–26.

Gupta HS, Schratter S, Tesch W, et al. (2005). Two different correlations between nanoindentation modulus and mineral content in the bone–cartilage interface. Journal of structural biology 149, 138–148.

Hale LF, Lowe CG, (2008). Age and growth of the round stingray *Urobatis halleri* at Seal Beach, California. J Fish Biol 73, 510– 523.

Hall BK, (1975). Evolutionary consequences of skeletal differentiation. Integrative and Comparative Biology 15, 329–350.

Hall BK (2005). Bones and Cartilage: Developmental and Evolutionary Skeletal Biology. San Diego: Academic Press.

Hall BK, Witten PE, (2007). Plasticity of and transitions between skeletal tissues in vertebrate evolution and development, in: Anderson JS, Sues H-D (Eds.), Major Transitions in Vertebrate Evolution. Indiana University Press Bloomington, pp. 13–56.

Halstead LB (1974). Vertebrate Hard Tissues. London: Wykeham Publications.

Hasse KE, (1879). Das natürliche System der Elasmobranchier auf Grundlage des Baues und der Entwicklung ihrer Wirbelsäule: eine morphologische und paläontologische Studie. Vol. 2, Gustav Fischer, Jena.

Heinegård D, Oldberg A, (1989). Structure and biology of cartilage and bone matrix noncollagenous macromolecules. FASEB J 3, 2042–2051.

Henisch HK, (2005). Crystals in Gels and Liesegang Rings. Cambridge: Cambridge University Press.

Hinton RJ, Jing Y, Jing J, et al. (2017). Roles of chondrocytes in endochondral bone formation and fracture repair. Journal of Dental Research 96, 23–30.

Hoenig JM, Walsh AH, (1983). Skeletal lesions and deformities in large sharks. J Wildl. Dis. 19, 27–33.

Hoerth RM, Seidt BM, Shah M, et al. (2014). Mechanical and structural properties of bone in non-critical and critical healing in rat. Acta Biomater. 10, 4009–4019.

Holmbeck K, Bianco P, Caterina J, et al. (1999). MT1-MMP-deficient mice develop dwarfism, osteopenia, arthritis, and connective tissue disease due to inadequate collagen turnover. Cell 99, 81–92.

Huber D, Neveu DE, Stinson CM, et al. (2013). Mechanical properties of sand tiger shark *Carcharias taurus* vertebrae in relation to spinal deformity. J Exp Biol 216, 4256–4263.

Humason GL, (1962). Animal tissue techniques. Animal tissue techniques.

Hunziker EB, Quinn TM, Häuselmann HJ, 2002. Quantitative structural organization of normal adult human articular cartilage. Osteoarthritis and Cartilage 10, 564–572.

Janvier P, Arsenault M, Desbiens S, 2010. Calcified cartilage in the paired fins of the osteostracan Escuminaspis laticeps (Traquair 1880), from the Late Devonian of Miguasha (Québec, Canada), with a consideration of the early evolution of the pectoral fin endoskeleton in vertebrates. Journal of Vertebrate Paleontology 24, 773–779.

Jaschouz D, Paris O, Roschger P, et al. (2003). Pole figure analysis of mineral nanoparticle orientation in individual trabecula of human vertebral bone. J Appl. Crystallogr. 36, 494–498.

Johanson Z, Kearsley A, den Blaauwen J, et al. (2010). No bones about it: an enigmatic Devonian fossil reveals a new skeletal framework – a potential role of loss of gene regulation. Semin Cell Dev Biol 21, 414–423.

Jones SJ, Boyde A, (1974). The organization and gross mineralization patterns of the collagen fibres in sharpey fibre bone. Cell Tissue Res 148, 83–96.

Kalya S, Rosenthal AK, (2005). Extracellular matrix changes regulate calcium crystal formation in articular cartilage. Curr. Opin. Rheumatol. 17, 325–329.

Kemp NES, Westrin SK, (1979). Ultrastructure of calcified cartilage in the endoskeletal tesserae of sharks. J Morphol 160, 75–101.

Kirsch T, Wang W, Pfander D (2003). Functional differences between growth plate apoptotic bodies and matrix vesicles. J Bone Miner Res 18, 1872–1881.

Kóssa G, (1901). Ueber die im Organismus künstlich erzeugbaren Verkalkungen. Beiträge zur pathologischen Anatomie und zur allgemeinen Pathologie; 1901. Zweites Heft.

Kölliker A, (1864). Weitere Beobachtungen über die Wirbel der Selachier. Abh. Senckenberg. Naturf. Ges.

Kuz'min VI, Gadzaov AF, Tytik DL, et al. (2013). Kinetics of the formation of Liesegang rings. J Struct Chem, 54.2, 363–378.

Kwan AP, Cummings CE, Chapman JA, et al. (1991). Macromolecular organization of chicken type X collagen in vitro. J Cell Biol 114, 597–604.

Landis WJ, Glimcher MJ, (1978). Electron diffraction and electron probe microanalysis of the mineral phase of bone tissue prepared by anhydrous techniques. J Ultrastruct Res 63, 188–223.

Landis WJ, Hodgens KJ, Song MJ, et al. (1996). Mineralization of collagen may occur on fibril surfaces: Evidence from conventional and high-voltage electron microscopy and three-dimensional imaging. J Struct Biol 117, 24–35.

Lawton DM, Oswald WB, McClure J, (1995). The biological reality of the interlacunar network in the embryonic, cartilaginous, skeleton: A thiazine dye/absolute ethanol/LR White resin protocol for

visualizing the network with minimal tissue shrinkage. Journal of Microscopy 178, 66–85.

Lee AK, van Beuzekom M, Glowacki J, et al. (1984). Inhibitors, enzymes and growth factors from shark cartilage. Comp Biochem Physiol 78B, 609–616.

Legros R, Balmain N, Bonel G, (1987). Age-related-changes in mineral of rat and bovine cortical bone. Calcif Tissue Int 41, 137–144.

Leydig F, (1852). Beiträge zur Mikroskopischen Anatomie und Entwicklungsgeschichte der Rochen und Haie. Leipzig: Wilhelm Engelmann.

Liesegang RE, (1907). Über die Schichtungen bei Diffusionen: Eine Voruntersuchung. Düsseldorf: Ohligschläger.

Liu X, Dean MN, Summers AP, et al. (2010). Composite model of the shark's skeleton in bending: a novel architecture for biomimetic design of functional compression bias. Mater Sci Eng: C 30, 1077.

Liu, Y, Ibrahim, AS, Tay, B-H, Richardson, et al. (2010). Parathyroid hormone gene family in a cartilaginous fish, the elephant shark (*Callorhinchus milii*). Journal of Bone and Mineral Research 25, 2613–2623.

Liu X, Dean MN, Youssefpour H, et al. (2014). Stress relaxation behavior of tessellated cartilage from the jaws of blue sharks. J Mech Behav Biomed Mater 29, 68–80.

Long JA, Burrow CJ, Ginter M, et al. (2015). First shark from the late Devonian (Frasnian) Gogo Formation, Western australia sheds new light on the development of tessellated calcified cartilage. PLoS One 10, e0126066.

Lyons K, Lavado R, Schlenk D, et al. (2014). Bioaccumulation of organochlorine contaminants and ethoxyresorufin-o-deethylase activity in southern California round stingrays (*Urobatis halleri*) exposed to planar aromatic compounds. Environ Toxicol Chem 33, 1380–1390.

Lorch IJ, (1949). The distribution of alkaline phosphatase in relation to calcification in *Scyliorhinus canicula*. Development of the Endoskeleton. J Cell Sci 3, 381–390.

Lowenstam, HA, Weiner S, (1989). On biomineralization. Oxford University Press on Demand, 1989.

Luo G, Ducy P, McKee MD, et al. (1997). Spontaneous calcification of arteries and cartilage in mice lacking matrix GLA protein. Nature 386, 78–81.

Maes C, Kobayashi T, Selig MK, et al. (2010). Osteoblast precursors, but not mature osteoblasts, move into developing and fractured bones along with invading blood vessels. Dev Cell 19, 329–344.

Mahamid J, Sharir A, Gur D, et al. (2011). Bone mineralization proceeds through intracellular calcium phosphate loaded vesicles: a cryo-electron microscopy study. J Struct Biol 174, 527–535.

Maisey JG, (2013). The diversity of tessellated calcification in modern and extinct chondrichthyans. Rev Paleobiol 32, 335–371.

Martin RB, Burr DB, Sharkey NA, et al. (2015). Skeletal Tissue Mechanics. Springer, New York, NY.

McCarty DJ, Hogan JM, Gatter RA, et al. (1966). Studies on pathological calcifications in human cartilage. I. Prevalence and types of crystal deposits in the menisci of two hundred fifteen cadavera. J Bone Joint Surg Am 48, 309– 325.

Melrose J, Smith S, Whitelock J, (2004). Perlecan immunolocalizes to perichondrial vessels and canals in human fetal cartilaginous primordia in early vascular and matrix remodeling events associated with diarthrodial joint development. J Histochem Cytochem 52, 1405–1413.

Mizuta S, Hwang J, Yoshinaka R, (2003). Molecular species of collagen in pectoral fin cartilage of skate (*Raja kenojei*). Food Chem 80, 1–7.

Mollen FH, Wintner SP, Iglesias SP, (2012). Comparative morphology of rostral cartilages in extant mackerel sharks (Chondrichthyes, Lamniformes, Lamnidae) using CT scanning. Zootaxa 3340, 29–43.

Moss ML, (1968). The origin of vertebrate calcified tissues. In: Current Problems of Lower Vertebrate Phylogeny. (ed. Ørvig T), pp. 359–371. New York: Wiley (Interscience).

Moss ML, (1977). Skeletal tissues in sharks. Am. Zool. 17, 335–342.

Mulisch M, Welsch U, (2015). Romeis – mikroskopische technik. doi:10.1007/978-3-642-55190-1

Müller J, 1836. Ueber die Structur und die chemischen Eigenschaften der thierischen Bestandtheile der Knorpel und Knochen. Annalen der Physik 114, 295–353.

Obrant KJ, Odselius R, (1985). Electron microprobe investigation of calcium and phosphorus concentration in human bone trabeculae—Both normal and in posttraumatic osteopenia. Calcif Tissue Int 37, 117–120.

Officer RA, Clement JG, Rowler DK, (1995). Vertebral deformities in a school shark, Galeorhinus galeus: circumstantial evidence for endoskeletal resorption? J Fish Biol 46, 85–98.

Omelon S, Georgiou J, Variola F, et al. (2014). Colocation and role of polyphosphates and alkaline phosphatase in apatite biomineralization of elasmobranch tesserae. Acta Biomater. 10, 3899–3910.

Ortiz-Delgado JB, Simes DC, Viegas CSB, et al. (2005). Cloning of matrix Gla protein in a marine cartilaginous fish, *Prionace glauca*: preferential protein accumulation in skeletal and vascular systems. Histochem. Cell Biol 126, 89–101.

Ørvig T, (1951). Histologic Studies of Placoderms and fossil Elasmobranchs. I: The endoskeleton, with remarks on the hard tissues of lower vertebrates in general. Arkiv Zool 2, 321–454.

Peignoux-Deville J, Lallier F, Vidal B, (1982). Evidence for the presence of osseous tissue in dogfish vertebrae. Cell Tissue Res 222, 605–614.

Penel G, Leroy N, Van Landuyt P, et al. (1999). Raman microspectrometry studies of brushite cement: in vivo evolution in a sheep model. Bone 25, 81S–84S.

Politi Y, Pippel E, Licuco-Massouh AC, et al. (2016). Nano-channels in the spider fang for the transport of Zn ions to cross-link His-rich proteins pre-deposited in the cuticle matrix. Arthropod Struct Dev 46, 30–38.

Poole AR, Pidoux I, (1989). Immunoelectron microscopic studies of type X collagen in endochondral ossification. J Cell Biol 109, 2547–2554.

Poole AR, (1991). The growth plate: cellular physiology, cartilage assembly and mineralization. Cartilage: molecular aspects 179–211.

Poole CA, (1997). Articular cartilage chondrons: Form, function and failure. Journal of anatomy 191, 1–13.

Porter ME, Beltran JL, Koob TJ, et al. (2006). Material properties and biochemical composition of mineralized vertebral cartilage in seven elasmobranch species (Chondrichthyes). J Exp Biol 209, 2920–2928.

Puchtler H, Meloan SN, (1978). Demonstration of phosphates in calcium deposits – modification of Von Kossa reaction. Histochemistry 56, 177–185.

Puchtler H, Meloan SN, (1985). On the chemistry of formaldehyde fixation and its effects on immunohistochemical reactions. Histochemistry 82, 201–204.

Rama S, Chandrakasan G, (1984). Distribution of different molecular species of collagen in the vertebral cartilage of shark (*Carcharius acutus*). Connective tissue research 12, 111–118.

Ravaglioli A, Krajewski A, Celotti GC, et al. (1996). Mineral evolution of bone. Biomaterials 17, 617–622.

Reichenberger E, Aigner T, von der Mark K, et al. (1991). In situ hybridization studies on the expression of type X collagen in fetal human cartilage. Dev Biol 148, 562–572.

Reinholt FP, Hultenby K, Oldberg A, et al. (1990). Osteopontin – a possible anchor of osteoclasts to bone. PNAS 87, 4473–4475.

Remaggi F, Ferretti M, Cane V, et al. (1996). Histomorphological and chemico-physical analyses of the mineral matrix of micropetrotic human bone. Ann Anat 178, 223–227.

Ridewood W, (1921). On the calcification of the vertebral centra in sharks and rays. Philos T R Soc Lon B 210, 311–407.

Romeis B, (1968). Mikroskopische Technik. Oldenbourg Verlag, München and Wien.

Roschger P, Fratzl P, Eschberger J, et al. (1998). Validation of quantitative backscattered electron imaging for the measurement of mineral density distribution in human bone biopsies. Bone 23, 319–326.

Roth W, (1911). Beiträge zur Kenntnis der Strukturverhältnisse des Selachier-Knorpels. Morphologisches Jahrbuch 42, 485–555.

Ryu K, Iriuchishima T, Oshida M, et al. (2014). The prevalence of and factors related to calcium pyrophosphate dihydrate crystal deposition in the knee joint. Osteoarthr. Cartilage 22 (7), 975–979.

Schaeffer B, (1981). The xenacanth shark neurocranium, with comments on elasmobranch monophyly. Bulletin of the AMNH; v. 169, article 1.

Schmidt WJ, (1952). Über die Verkalkung des Knorpelgewebes der Haie. Cell Tissue Res 37, 377–388.

Seidel R, Lyons K, Blumer M, et al. (2016). Ultrastructural and developmental features of the tessellated endoskeleton of elasmobranchs (sharks and rays). J Anat 229, 681–702.

Seidel R, Blumer M, Zaslansky P, Knötel D, Huber DR, Weaver JC, Fratzl P, Omelon S, Bertinetti L, Dean MN, (2017). Ultrastructural, material and crystallographic description of endophytic masses - A possible damage response in shark and ray tessellated calcified cartilage. Journal of structural biology. doi:10.1016/j.jsb.2017.03.004

Seto J, Gupta HS, Zaslansky P, et al. (2008). Tough lessons from bone: extreme mechanical anisotropy at the mesoscale. Advanced Functional Materials 18, 1905–1911.

Sharpey W, (1848). Bone or osseous tissue. Elements of Anatomy.

Shellis RP, Heywood BR, Wahab FK, (1997). Formation of brushite, monetite and whitlockite during equilibration of human enamel with acid solutions at 37 degrees C. Caries Res 31, 71–77.

Shen G, (2005). The role of type X collagen in facilitating and regulating endochondral ossification of articular cartilage. Orthodontics and Craniofacial Research 8, 11–17. doi:10.1111/j.1601-6343.2004.00308.x

Sivakumar P, Chandrakasan G, (1998). Occurrence of a novel collagen with three distinct chains in the cranial cartilage of the squid *Sepia officinalis*: comparison with shark cartilage collagen. Biochim Biophys Acta 1381, 161–169.

Stern KH, (1967). Bibliography of Liesegang Rings. Washington: US National Bureau of Standards.

Stockwell RA, (1967). The cell density of human articular and costal cartilage. J Anat 101, 753–763.

Takagi M, Parmley RT, Denys FR, et al. (1984). Ultrastructural cytochemistry of proteoglycans associated with calcification of shark cartilage. Anat Rec 208, 149–158.

Temizel N, Girisken G, Tas AC, (2011). Accelerated transformation of brushite to octacalcium phosphate in new biomineralization media between 36 C and 80 C. Mater Sci Eng, C 31, 1136–1143.

Termine JD, Kleinman HK, Whitson SW, et al. (1981). Osteonectin, a bone-specific protein linking mineral to collagen. Cell 26, 99–105.

Thompson DW, (1942). On Growth and Form. Cambridge: Cambridge University Press.

Tretjakoff D, (1926). Die Funktionelle Struktur der Chordascheiden und der Wirbel bei Zyklostomen und Fischen. Cell Tissue Res 4, 266–312.

Trivett MK, Walker TI, Macmillan DL, et al. (2002). Parathyroid hormone-related protein (PTHrP) production sites in elasmobranchs. J Anat 201, 41–52.

Turner CH, (1998). Three rules for bone adaptation to mechanical stimuli. Bone 23, 399–407.

Urist MR (1961). Calcium and phosphorus in the blood and skeleton of the Elasmobranchii. Endocrinology 69, 778–801.

Urist MR (1962). Calcium and other ions in blood and skeleton of Nicaraguan fresh-water shark. Science 137, 984–986.

Urist MR (1967). Avian parathyroid physiology: including a special comment on calcitonin. Am Zool 7, 883–895.

Venkatesh B, Lee AP, Ravi V, et al. (2014). Elephant shark genome provides unique insights into gnathostome evolution. Nature 505, 174–179.

Verborgt O, Gibson GJ, Schaffler MB, (2000). Loss of osteocyte integrity in association with microdamage and bone remodeling after fatigue in vivo. J Bone Miner Res 15, 60–67.

Vortkamp A, Lee K, Lanske B, et al. (1996). Regulation of rate of cartilage differentiation by Indian hedgehog and PTH-related protein. Science 273, 613–622.

Weidenreich F, (1930). Das Knochengewebe. In v. Möllendorffs Handbuch der mikroskopischen Anatomie des Menschen. Die Gewebe, 11/2, 391.Berlin: Springer.

Wilga CA, Diniz SE, Steele PR, et al. (2016). Ontogeny of feeding mechanics in smoothhound sharks: morphology and cartilage stiffness. Integrative and comparative biology, 56(3), 442-448.

Witten PE, Hall BK, (2002). Differentiation and growth of kype skeletal tissues in anadromous male Atlantic salmon (*Salmo salar*). Int J Dev Biol 46, 719–730.

Witten PE, Huysseune A, Hall BK, (2010). A practical approach for the identification of the many cartilaginous tissues in teleost fish. Journal of Applied Ichthyology 26, 257–262.

Woodward AS, (1892). On the Lower Devonian Fish-Fauna of Campbellton, New Brunswick. Geol Mag 9, 1–6.

Wopenka B, Pasteris JD, (2005). A mineralogical perspective on the apatite in bone. Materials Science & Engineering C-Biomimetic and Supramolecular Systems 25, 131–143. doi:10.1016/j.msec.2005.01.008

Wurmbach H, (1932). Das Wachstum des Selachierwirbels und seiner Gewebe. Zool Jahrb 55, 1–136.

Zizak I, Roschger P, Paris O, et al. (2003). Characteristics of mineral particles in the human bone/cartilage interface. J Struct Biol 141, 208–217.

9. EIDESSTATTLICHE ERKLÄRUNG

Hiermit erkläre ich, die Dissertation selbstständig und nur unter Verwendung der angegebenen Hilfen und Hilfsmittel angefertigt zu haben. Ich habe mich anderwärts nicht um einen Doktorgrad beworben und besitze keinen entsprechenden Doktorgrad. Ich erkläre, dass ich die Dissertation oder Teile davon nicht bereits bei einer anderen wissenschaftlichen Einrichtung eingereicht habe und dass sie dort weder angenommen noch abgelehnt wurde. Ich erkläre die Kenntnisnahme der dem Verfahren zugrunde liegenden Promotionsordnung der Lebenswissenschaftlichen Fakultät der Humboldt-Universität zu Berlin vom 5. März 2015. Weiterhin erkläre ich, dass keine Zusammenarbeit mit gewerblichen Promotionsberaterinnen/Promotionsberatern stattgefunden hat und dass die Grundsätze der Humboldt-Universität zu Berlin zur Sicherung guter wissenschaftlicher Praxis eingehalten wurden.

Ronald Seidel   Potsdam-Golm, September 2017

10. ACKNOWLEDGEMENTS

The work that is presented within this thesis is a result of wonderful collaborations with many scientists who are experts in their disciplines. I want to thank all my co-authors for their great work, for introducing me to new techniques and allowing me to learn from their expertise, for valuable discussions helping me to understand and put the findings into a wider context.

I am deeply grateful to my supervisor Mason N. Dean for his confidence in me, giving me the chance to do my PhD at the MPIKG working in this fantastic multi-institutional and interdisciplinary project. Mason is an amazing supervisor, mentor and *Doktorvater*. I owe you a lot! I always felt supported, and free to 'run my own course', and I learned so much from you about scientific writing, presenting and communicating. Beyond that about the American humor and culture! In particular, I want to thank you for your understanding of my work-life-interface, which I think is the foundation for the success of our work and our friendship.

During my PhD at the Max Planck Institute of Colloids and Interfaces I clearly benefited from the great atmosphere in the institute and the high density of great scientists, of those who established their careers already and those who will (hopefully) have a bright career. It has been a wonderful time with fantastic colleagues working hard pushing the boundaries of science, with inspiring discussions on projects and goals, in both the academic career and life, and with many, many cakes. I also want to thank the technicians of the MPIKG for their support and their great work, for their time in planning sample preparation and running experiments. In particular, I want to thank and express my highest respect to Prof. Dr. Peter Fratzl for creating such a wonderful atmosphere in the department –every single day– and for your support from the very first minute on. Peter, you're making this a special place!

I also want to thank my beloved family, Maria and my beautiful sons. Maria, thank you for your support, your patience, your great company, your faith and your love!

Thanks boys, for making me laugh and enjoy the 'small things' in life. Thank you also for keeping me up at night giving me more time to think about my studies and results, for waking me up early in the morning, sometimes very early, just to make sure I get the last direct train to Golm – You are the best, I'm proud of you, I love you!

I'm dedicating this thesis to my mom.